Light Element Production in the Big Bang and the Synthesis of Heavy Elements in 3D MHD Jets from Core-Collapse Supernovae

Inauguraldissertation

zur

Erlangung der Würde eines Doktors der Philosophie
vorgelegt der
Philosophisch-Naturwissenschaftlichen Fakultät
der Universität Basel

von

Christian Winteler

aus Glarus Nord, GL

Basel, 2013

Originaldokument gespeichert auf dem Dokumentenserver der Universität Basel
edoc.unibas.ch

Dieses Werk ist unter dem Vertrag „Creative Commons Namensnennung-Keine kommerzielle Nutzung-Keine Bearbeitung 2.5 Schweiz“ lizenziert. Die vollständige Lizenz kann unter
creativecommons.org/licences/by-nc-nd/2.5/ch
eingesehen werden.

Genehmigt von der Philosophisch-Naturwissenschaftlichen Fakultät
auf Antrag von

Prof. Dr. F.-K. Thielemann
PD Dr. T. Rauscher
Prof. Dr. Karl-Ludwig Kratz

Basel, den 15. November 2011

Prof. Dr. Martin Spiess

Namensnennung-Keine kommerzielle Nutzung-Keine Bearbeitung 2.5 Schweiz

Sie dürfen:

das Werk vervielfältigen, verbreiten und öffentlich zugänglich machen

Zu den folgenden Bedingungen:

Namensnennung. Sie müssen den Namen des Autors/Rechteinhabers in der von ihm festgelegten Weise nennen (wodurch aber nicht der Eindruck entstehen darf, Sie oder die Nutzung des Werkes durch Sie würden entlohnt).

Keine kommerzielle Nutzung. Dieses Werk darf nicht für kommerzielle Zwecke verwendet werden.

Keine Bearbeitung. Dieses Werk darf nicht bearbeitet oder in anderer Weise verändert werden.

- Im Falle einer Verbreitung müssen Sie anderen die Lizenzbedingungen, unter welche dieses Werk fällt, mitteilen. Am Einfachsten ist es, einen Link auf diese Seite einzubinden.

- Jede der vorgenannten Bedingungen kann aufgehoben werden, sofern Sie die Einwilligung des Rechteinhabers dazu erhalten.
- Diese Lizenz lässt die Urheberpersönlichkeitsrechte unberührt.

Die gesetzlichen Schranken des Urheberrechts bleiben hiervon unberührt.

Die Commons Deed ist eine Zusammenfassung des Lizenzvertrags in allgemeinverständlicher Sprache: http://creativecommons.org/licenses/by-nc-nd/2.5/ch/legalcode.de

Haftungsausschluss:
Die Commons Deed ist kein Lizenzvertrag. Sie ist lediglich ein Referenztext, der den zugrundeliegenden Lizenzvertrag übersichtlich und in allgemeinverständlicher Sprache wiedergibt. Die Deed selbst entfaltet keine juristische Wirkung und erscheint im eigentlichen Lizenzvertrag nicht. Creative Commons ist keine Rechtsanwaltsgesellschaft und leistet keine Rechtsberatung. Die Weitergabe und Verlinkung des Commons Deeds führt zu keinem Mandatsverhältnis.

Quelle: http://creativecommons.org/licenses/by-nc-nd/2.5/ch/ Datum: 3.4.2009

Abstract

In this dissertation we present the main features of a new nuclear reaction network evolution code. This new code allows nucleosynthesis calculations for large numbers of nuclides. The main results in this dissertation are all obtained using this new code.

The strength of standard big bang nucleosynthesis is, that all primordial abundances are determined by only one free parameter, the baryon-to-photon ratio η. We perform self consistent nucleosynthesis calculations for the latest WMAP value $\eta = (6.16 \pm 0.15) \times 10^{-10}$. We predict primordial light element abundances: D/H $= (2.84 \pm 0.23) \times 10^{-5}$, ^{3}He/H $= (1.07 \pm 0.09) \times 10^{-5}$, $\mathrm{Y_p} = 0.2490 \pm 0.0005$ and ^{7}Li/H $= (4.57 \pm 0.55) \times 10^{-10}$, in agreement with current observations and other predictions. We investigate the influence of the main production rate on the ^{6}Li abundance, but find no significant increase of the predicted value, which is known to be orders of magnitude lower than the observed.

The r-process is responsible for the formation of about half of the elements heavier than iron in our solar system. This neutron capture process requires explosive environments with large neutron densities. The exact astrophysical site where the r-process occurs has not yet been identified. We explore jets from magnetorotational core collapse supernovae (MHD jets) as possible r-process site. In a parametric study, assuming adiabatic expansion, we find good agreement with solar system abundances for a superposition of components with different electron fraction (Y_e), ranging from $Y_e = 0.1$ to $Y_e = 0.3$. Fission is found to be important only for $Y_e \leq 0.17$.

The first postprocessing calculations with data from 3D MHD core collapse supernova simulations are performed for two different simulations. Calculations are based on two different methods to extract data from the simulation: tracer particles and a two dimensional, mass weighted histogram. Both results yield almost identical results. We find that both simulations can reproduce the global solar r-process abundance pattern. The ejected mass is found to be in agreement with galactic chemical evolution for a rare event rate of one MHD jet every hundredth to thousandth supernova.

Contents

Abstract **vi**

1 Introduction **1**

2 Nuclear Reaction Network Calculations **3**

- 2.1 General Formalism . . . 3
  - 2.1.1 Photodisintegrations . . . 5
  - 2.1.2 Electron and Positron Captures . . . 6
  - 2.1.3 Decays . . . 7
- 2.2 Nuclear Reaction Networks . . . 7
- 2.3 Numerical Integration . . . 9
  - 2.3.1 Euler's Method . . . 9
  - 2.3.2 Stiff Equations . . . 10
  - 2.3.3 Newton-Raphson Iteration . . . 11
  - 2.3.4 Solving the Reaction Network Equations . . . 12
- 2.4 Taking Advantage of Matrix Sparseness . . . 14
  - 2.4.1 Sparse Matrix Solver . . . 15
  - 2.4.2 Compressed Sparse Column Format . . . 16
- 2.5 Nuclear Statistical Equilibrium . . . 17
- 2.6 Implementation of Reaction Rates . . . 20
  - 2.6.1 Reaclib . . . 20
  - 2.6.2 Electron and Positron Captures . . . 21
  - 2.6.3 β-delayed Neutron Emission . . . 22
  - 2.6.4 Fission . . . 22

3 The Big Bang **27**

- 3.1 Physics of the Expansion . . . 28
- 3.2 Building the Elements . . . 31
- 3.3 Nucleosynthesis . . . 34
  - 3.3.1 SBBN Predictions . . . 36
  - 3.3.2 Testing the Consistency of SBBN . . . 37
    - 3.3.2.1 Deuterium . . . 38
    - 3.3.2.2 ^{3}He . . . 40
    - 3.3.2.3 ^{4}He . . . 41
  - 3.3.3 The Lithium Problem . . . 43
    - 3.3.3.1 The Missing ^{7}Li . . . 43

3.3.3.2 The Mysterious ^{6}Li 46
3.3.4 Nonstandard Big Bang 46
3.3.4.1 The Model 47
3.3.4.2 Results 48

4 Formation of Heavy Elements **51**
4.1 The Life and Death of Massive Stars 51
4.2 The s- and r-Process 53
4.2.1 Clues from Abundance Observations 56
4.2.2 Conditions for the r-Process 58
4.2.3 Possible Candidates 59
4.3 MHD-Jets from CCSN 61

5 Results **63**
5.1 Results from Standard Calculations 64
5.2 The Influence of Fission 69
5.3 3D MHD CCSN Simulations 71
5.3.1 Simulation Setup 72
5.3.2 Postprocessing of Tracer Data 73
5.3.3 Extraction of 3D Data 76
5.3.4 Postprocessing of 3D Data 80
5.3.5 Discussion 82
5.3.6 Implications for Galactic Chemical Evolution 85

6 Summary and Outlook **87**

A Self-Consistent Big Bang Evolution **89**

B Reaction Rate Fit Coefficients **95**
B.1 $n \leftrightarrow p$ 95
B.2 $^2\mathrm{H}\,(\alpha,\gamma)\,^6\mathrm{Li}$ 96
B.3 $^6\mathrm{Li}\,(\gamma,\alpha)\,^2\mathrm{H}$ 96

Bibliography **97**

Curriculum Vitae **107**

Acknowledgements **109**

Chapter 1

Introduction

One of the fundamental questions of mankind, is the question, where we come from. I am aware that this question can neither be answered by physics alone, nor within the scope of this thesis. Nevertheless, it is the driving force behind science, to search for our own origin by studying the state and the formation of our surroundings.

Whenever someone asked me what my thesis is about, I answered, that I am trying to explain the origin of elements in our solar system and their distribution. The solar photosphere and meteorites reflect the chemical signature of the gas cloud, from which our sun formed (see Figure 1.1). The abundance distribution contains the footprints of astrophysical processes, that occurred long before our sun was born.

The lightest elements (the yellow area in Figure 1.1) are produced in the big bang. The primordial gas consists (in mass) of $\sim 75\%$ ^{1}H, $\sim 25\%$ ^{4}He and traces of deuterium (^{2}H), ^{3}He, and lithium. From these basic building blocks, the elements up to iron (the green area in Figure 1.1) are mostly synthesized by fusion reactions of charged nuclei in hydrostatic burning phases of massive stars. The production of elements beyond the iron peak is hindered by the increasing Coulomb barrier (with increasing proton number). Reactions with neutrons are the main mechanism for the formation of most elements heavier than iron.

Two processes have been identified by the double peak structure in solar abundances, each of which contributes to about half of the synthesis of heavy elements (red and blue areas in Figure 1.1). Depending on whether neutron captures are slow or rapid, compared to the β-decay timescale, the process is called slow process or rapid process (hereafter s-process and r-process)[20, 22]. While the s-process and its astrophysical sites are quite well understood, the r-process still poses some problems. Although the astrophysical site of the r-process has not yet been unambiguously identified, there are indications that point to core collapse supernovae (CCSN) as the best candidate.

Numerical models are necessary to simulate these spectacular events in order to determine which elements are produced and in what quantities. Current multi-dimensional simulations of CCSN can only be carried out on powerful supercomputers. Detailed nucleosynthesis calculations, that determine the composition of ejected matter, are performed in a postprocessing manner. Here, we finally arrive at the general topic of my Ph.D. thesis: Nucleosynthesis in explosive scenarios.

Nucleosynthesis calculations are an interesting combination of nuclear physics and computer science, embedded in an astrophysical scenario. To keep up with the fast developments in information technology, I decided to rewrite the nuclear reaction

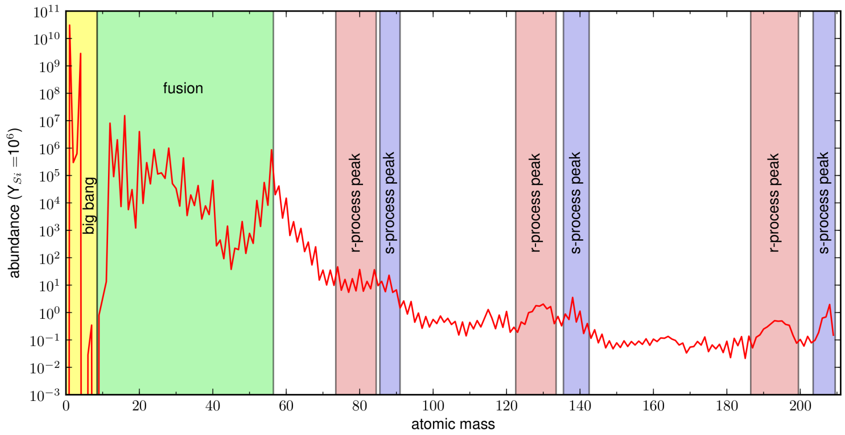

Figure 1.1: Solar system abundances of [13], with silicon normalized to 10^6

network code, that has been used for many years in our research group, from scratch. The main goal I pursued was to create a fast and versatile modern version of the old program.

Chapter 2 is dedicated to the theory of nuclear reaction network calculations. In a first part, thermonuclear reaction rates are derived and the nuclear reaction network equations are described. In a second part, the numerical methods to solve these equations are discussed in detail, and the main new features of the network code are introduced and their benefits discussed. In the final part of this chapter, the implementation of different kinds of reaction rates in the new code is presented.

In Chapter 3 the physics of the big bang and primordial nucleosynthesis are explained. The nucleosynthesis code is then used to perform self-consistent calculations of big-bang nucleosynthesis. Results are compared against observations and different nucleosynthesis predictions. The huge discrepancy between predicted and observed primordial lithium abundances is also discussed. The influence of different $^2\mathrm{H}(\alpha,\gamma)^6\mathrm{Li}$ reaction rates on the primordial ^{6}Li abundance is explored and the chapter ends with a short presentation of nucleosynthesis in inhomogeneous big-bang scenarios.

In Chapter 4 the main processes responsible for the formation of heavy elements are explained, together with a discussion of observational informations and astrophysical parameters for the r-process. Possible astrophysical sites for the r-process are also studied.

In Chapter 5 the focus will be set on MHD Jets from core collapse supernovae as possible r-process site. The influence of initial conditions on the final abundance distribution is qualitatively explored in a short parameter study. For the first time, data from 3D simulations of jets from core collapse supernovae is used as input for nucleosynthesis calculations. Two different methods to extract data from the simulation are investigated and qualitatively compared with results from lower dimensional simulations. A preliminary exploration of the consistency with galactic chemical evolution closes the chapter.

The thesis concludes with a summary of the results and an outlook on future projects and improvements in Chapter 6.

Chapter 2

Nuclear Reaction Network Calculations

In this section we introduce the formalism and techniques used in nuclear reaction network calculations. The purpose of a nuclear reaction network is to follow the evolution of nuclear abundances in astrophysical events. Such a network basically consists of a system of coupled first-order differential equations, one for each nuclide under investigation. The differential equations contain terms for individual nuclear reactions. Nuclear reactions are governed by three of the four fundamental forces: the electromagnetic force (emission and absorption of photons), the strong force (emission and absorption of nucleons and nuclei) and the weak force (emission and absorption of leptons such as electrons, positrons, neutrinos and antineutrinos). In Section 2.1 we will derive reaction rate expressions for the different interactions at work, following the (still) unpublished book by Cowan, Truran & Thielemann [29], starting from the most basic information about a reaction, the nuclear cross section. With this information, the basic concepts of reaction networks are introduced in Section 2.2. To evolve the system of differential equations over time, we have to rely on numerical methods. In Section 2.3 a detailed description of the numerical methods is given. Depending on the astrophysical scenario under investigation, the number of differential equations that have to be solved simultaneously can range from a few to several thousands. Solving large systems of coupled differential equations is usually pretty involved. In Section 2.4 we discuss some details of the computer program we developed in the course of this thesis, that take advantage of the characteristics of nuclear reaction networks. Under certain conditions, nuclear abundances do not depend on individual reaction rates anymore, but only on the given thermodynamic conditions. In Section 2.5 we present the common method to determine individual abundances under such conditions. Finally, in Section 2.6 the detailed implementation of certain reactions in the computer code is discussed.

2.1 General Formalism

The most basic piece of information about a nuclear reaction is the nuclear cross section. In the simple case of two colliding particles i and j, with number densities n_i, n_j and relative velocity $v = |\boldsymbol{v}_i - \boldsymbol{v}_j|$, the interaction cross section σ is defined by

$$\sigma = \frac{\text{number of reactions target}^{-1}\text{sec}^{-1}}{\text{flux of incoming projectiles}} = \frac{r/n_i}{n_j v}. \tag{2.1}$$

The second equality only holds when the relative velocity between targets and projectiles is constant, and has the value v. Then, r, the number of reactions per cm^3 and sec, can be expressed as $r = \sigma v n_i n_j$.

More generally, the targets and projectiles have specific distributions of velocities, in which case r is given by

$$r_{i;j} = \int \sigma\left(|\boldsymbol{v}_i - \boldsymbol{v}_j|\right) \cdot |\boldsymbol{v}_i - \boldsymbol{v}_j|\, dn_i dn_j. \tag{2.2}$$

The evaluation of this integral depends on the type of particles that are involved, and the distributions they obey. In the general case, where both i and j are nuclei in an astrophysical plasma, target and projectiles both obey a Maxwell-Boltzmann distribution, and with

$$dn_j = n_j \left(\frac{m_j}{2\pi k_B T}\right)^{3/2} exp\left(-\frac{m_j v_j^2}{2k_B T}\right) d^3 v_j = n_j \phi\left(\boldsymbol{v}_j\right) d^3 v_j \tag{2.3}$$

we find

$$r_{i;j} = n_i n_j \int \sigma\left(|\boldsymbol{v}_i - \boldsymbol{v}_j|\right) |\boldsymbol{v}_i - \boldsymbol{v}_j|\, \phi\left(\boldsymbol{v}_i\right) \phi\left(\boldsymbol{v}_j\right) d^3 v_i d^3 v_j \tag{2.4}$$

$$= n_i n_j \left\langle \sigma v \right\rangle_{i;j}. \tag{2.5}$$

The velocity distributions ϕ are those of a Boltzmann gas for a given number density and temperature

$$\phi\left(\boldsymbol{v_i}\right) = \left(\frac{m_i}{2\pi k_B T}\right)^{3/2} \exp\left(-\frac{m_i v_i}{2k_B T}\right) \tag{2.6}$$

The velocity integrated cross section $\left\langle \sigma v \right\rangle_{i;j}$ is often also referred to as reactivity. Using center of mass and relative coordinates rather than individual ones, the reactivity can be expressed as a function of relative velocity v and reduced mass $\mu = m_i m_j / \left(m_i + m_j\right)$ (see e.g. [23] for a more detailed derivation)

$$\left\langle \sigma v \right\rangle_{i;j} = \left(\frac{\mu}{2\pi k_B T}\right)^{3/2} \int \sigma\left(v\right) v \exp\left(-\frac{\mu v^2}{2k_B T}\right) d^3 v. \tag{2.7}$$

With $d^3 v = 4\pi v^2 dv$ and $E = \frac{1}{2}\mu v^2$ we can finally express Eq.(2.7) as an energy integral

$$\left\langle \sigma v \right\rangle_{i;j} = \left(\frac{8}{\mu\pi}\right)^{1/2} \left(k_B T\right)^{-3/2} \int_0^\infty E \sigma\left(E\right) \exp\left(-\frac{E}{k_B T}\right) dE. \tag{2.8}$$

It is obvious that the reactivity only depends on the temperature and, knowing $\sigma\left(E\right)$ of a nuclear reaction, can easily be calculated, provided that the participating nuclei obey Maxwell-Boltzmann statistics.

Using Eq.(2.5) we can define a mean lifetime of nuclide i against destruction through projectile j:

$$\tau_j\left(i\right) = \frac{1}{\left\langle \sigma v\right\rangle_{i;j} n_j}. \tag{2.9}$$

The cross sections needed to calculate the reaction rates are provided by experimental measurements (where feasible) and theoretical predictions. However, not all cross sections have to be determined explicitly. There exists a relation between the cross section of a reaction $i\left(j,o\right)m$ and its inverse reaction $m\left(o,j\right)i$. Using the Hauser-Feshbach formalism [51] one can derive an expression for the ratio of the two cross sections [19]

$$\frac{\sigma_i\left(j,o\right)_J}{\sigma_m\left(o,j\right)_J} = \frac{1+\delta_{ij}}{1+\delta_{om}}\frac{g_o g_m}{g_i g_j}\frac{k_o^2}{k_j^2}, \tag{2.10}$$

where the k are wave numbers with $k_o = p_o/\hbar = \sqrt{2\mu_{om}E_{om}}/\hbar$ (k_j is defined analogously), the g are the degeneracy factors of the ground state, $g_i = \left(2J_i^0+1\right)$, and the δ are Kronecker deltas. The subscript J indicates a single populated state in the compound nucleus with spin J. The relation in Eq.(2.10) is also known and referred to as *detailed balance*. This relation holds for all individual transitions summed over compound states J. Thus we obtain a similar relation for the total cross section

$$\frac{\sigma_i\left(j,o;E_{ij}\right)}{\sigma_m\left(o,j;E_{om}\right)} = \frac{1+\delta_{ij}}{1+\delta_{om}}\frac{g_o g_m}{g_i g_j}\frac{k_o^2}{k_j^2}, \tag{2.11}$$

at corresponding energies $E_{ij} = E_{om} + Q_{o,j}$, where $Q_{o,j}$ is the Q-value of the reaction $m\left(o,j\right)i$. For reactions in an astrophysical plasma the excited states of nuclei i and m are thermally populated, i.e. g_i and g_m have to be replaced by G_i and G_m, with $G_x = \sum_n\left(2J_n+1\right)\exp\left(-E_n/k_BT\right)$. Using Eq.(2.8) for the reactivity $\langle\sigma v\rangle$ and the above relation for the cross sections, we obtain

$$\left\langle \sigma v\right\rangle_{i;j,o} = \frac{1+\delta_{ij}}{1+\delta_{om}}\frac{G_m g_o}{G_i g_j}\left(\frac{\mu_{om}}{\mu_{ij}}\right)^{3/2}\exp\left(-Q_{o,j}/k_BT\right)\left\langle \sigma v\right\rangle_{m;o,j}. \tag{2.12}$$

Here μ again denotes the reduced mass (see above).

We note that the above relation is not only convenient but in fact very important for the application of reaction rates in reaction networks. Using detailed balance one avoids numerical inconsistencies in network calculations, which may arise when forward and reverse rates are calculated separately, or even worse, from different sources. The proper balance between the two directions can only be achieved in employing detailed balance [108].

In the following subsections we will derive similar expressions for reactions, where particles other than nuclei participate, and thus different statistics apply.

2.1.1 Photodisintegrations

The treatment of reactions with photons, leptons or simple decays is very similar. Nevertheless, we will discuss each quickly in detail. Again, we follow the general definition of $r_{i;j}$ given in Eq.(2.2). For a reaction with a photon, projectile j is replaced by the photon, resulting in a reaction of the type $i(\gamma,o)m$. The relative velocity is the speed of light, c, and the distribution dn_j is the Planck distribution of photons

$$dn_\gamma = \frac{8\pi}{c^3}\frac{\nu d\nu}{exp(h\nu/k_BT)-1} = \frac{1}{\pi^2\,(c\hbar)^3}\frac{E_\gamma^2 dE_\gamma}{exp(E_\gamma/k_BT)-1}. \tag{2.13}$$

The target i is a nucleus and thus the distribution dn_i is a Boltzmann distribution with $\int dn_i = n_i$. Since the relative velocity between the nucleus and the photon is constant, and the photodisintegration cross section is only dependent on the photon energy E_γ, the integration over dn_i can easily be performed, resulting in

$$r_{i;\gamma} = n_i \lambda_{i;\gamma,o}(T) \tag{2.14}$$

with

$$\lambda_{i;\gamma,o}(T) = \frac{1}{\pi^2 c^2 \hbar^3}\int_0^\infty \frac{\sigma_i(\gamma,o;E_\gamma)E_\gamma^2}{exp(E_\gamma/k_BT)-1}dE_\gamma. \tag{2.15}$$

Contrary to reactions where both reaction partners are following a Boltzmann distribution, resulting in Eq.(2.5), Eq.(2.14) only has a linear dependence on the number density of the nucleon. Thus the integral acts like an effective (temperature dependent) "decay constant" of nucleus i.

In practice, the photodisintegration cross section does not have to be measured, because it is related to the capture cross section of the reverse reaction $m\,(o,\gamma)\,i$ by detailed balance. Using the detailed balance relation in Eq.(2.10), we can rewrite Eq.(2.15) as

$$\lambda_{i;\gamma,o}(T) = \frac{g_o G_m}{(1+\delta_{om})\,G_i}\left(\frac{\mu_{om}k_BT}{2\pi\hbar^2}\right)^{3/2}\exp\left(-Q_{o,\gamma}/k_BT\right)\langle\sigma v\rangle_{m;o,\gamma}\,, \tag{2.16}$$

using $k_\gamma = E_\gamma/\hbar c$, $g_\gamma = 2$ and $E_\gamma = E_{om} + Q_{o,\gamma}$. When deriving this relation it must be assumed, that the denominator $(\exp(E/k_BT)-1)$ of the Planck distribution, appearing in Eq.(2.15), can be replaced by $\exp(E/k_BT)$. Although this approximation is mathematically unsound, it turns out that it introduces an error of less than a few percent for astrophysically relevant temperatures and rate values [108].

2.1.2 Electron and Positron Captures

For nuclear electron capture reactions

$$e^- + (A,Z) \rightarrow (A,Z-1) + \nu_e, \tag{2.17}$$

we can apply a similar procedure as for photodisintegration reactions. Due to the vast mass difference between electrons ($m_e = 0.511$ MeV/c^2) and nuclei ($m_A \approx 931$ MeV/c^2) we can assume that nucleus i is at rest at the center of mass and the relative velocity v, determining the cross section and the rate, is entirely due to the electron velocity. In that case, similar to photodisintegrations, where the relative velocity was c, the rate integral in Eq.(2.2) is independent of nucleus i and dn_i and the integration can easily be performed, to give

$$\begin{aligned} r_{i;e} &= n_i \int \sigma_e\left(v_e\right) v_e dn_e \\ &= n_i \lambda_{i;e}\left(\rho Y_e, T\right). \end{aligned} \tag{2.18}$$

This expression is very similar to Eq.(2.14), but this time the "decay constant" depends on temperature *and on density.* Once the electron capture cross sections are known, temperature and density will determine, whether dn_e represents a Maxwell-Boltzmann or a Fermi distribution, which can be partially or fully degenerate or relativistic. This treatment has been extended to the capture of positrons [47, 48, 49]

$$e^+ + (A, Z) \rightarrow (A, Z+1) + \bar{\nu}_e, \tag{2.19}$$

which are in thermal equilibrium with photons and electrons once the temperature is high enough for photons to produce electron-positron pairs.

2.1.3 Decays

For normal decays, like α- or β-decays, with a half life $\tau_{1/2}$, we obtain an equation similar to Eq.(2.14) and (2.18), with a decay constant $\lambda_i = \ln 2/\tau_{1/2,i}$ and

$$r_i = n_i \lambda_i. \tag{2.20}$$

For the ground state, the half life is constant. However, at higher temperatures, excited states n can also be thermally populated and have different decay constants $\lambda_{i,n}$. The total temperature dependent decay constant for nucleus i then becomes

$$\lambda_i\left(T\right) = \frac{\sum_n \lambda_{i,n}\left(2J_n+1\right)\exp\left(-E_n/k_BT\right)}{G_i\left(T\right)} \tag{2.21}$$

where $G_i\left(T\right) = \sum\left(2J_n+1\right)\exp\left(-E_n/k_BT\right)$.

2.2 Nuclear Reaction Networks

In the previous section we derived two expressions for r, the number of reactions per cm^3 per sec: (i) $r_{i,j} = n_i n_j < \sigma v >_{i,j}$ for two-particle reactions and (ii) $r_i = n_i \lambda_i$ for photodisintegrations, decays and capture reactions. In the first term, we neglected a correction for a gas of identical particles. In such a gas, every particle would be counted twice, since it would act once as a target and once as a projectile. Thus the general form of $r_{i,j}$ is given by

$$r_{i,j} = \frac{1}{1+\delta_{ij}} n_i n_j < \sigma v >_{i,j}\ . \tag{2.22}$$

Without detailed derivation, we introduce a similar formula for three-body reactions:

$$r_{i,j,k} = \frac{1}{1+\Delta_{ijk}} n_i n_j n_k < \sigma v >_{i,j,k}, \tag{2.23}$$

where $\Delta_{ijk} = \delta_{ij} + \delta_{jk} + \delta_{ik} + 2\delta_{ijk}$ is the factor that prevents double counting in three body reactions [40].

For a single reaction $i(j,o)m$, the changes in number densities due to nuclear reactions rather than density changes are given by

$$\begin{aligned} \left(\frac{\partial n_i}{\partial t}\right)_\rho &= \left(\frac{\partial n_j}{\partial t}\right)_\rho = -r_{i;j} \\ \left(\frac{\partial n_o}{\partial t}\right)_\rho &= \left(\frac{\partial n_m}{\partial t}\right)_\rho = +r_{i;j}. \end{aligned}$$

In an astrophysical plasma a whole variety of different reactions, producing and destroying a nucleus i, can occur simultaneously, leading to

$$\left(\frac{\partial n_i}{\partial t}\right)_{\rho=const} = \sum_j N^i_j r_j + \sum_{j,k} \frac{N^i_{j,k}}{1+\delta_{jk}} r_{j,k} + \sum_{j,k,l} \frac{N^i_{j,k,l}}{1+\Delta_{jkl}} r_{j,k,l}. \tag{2.24}$$

The three sums on the right hand side of the equation are over reactions which produce or destroy a nucleus of species i with one, two or three reactant nuclei respectively. The individual $N^i s$ are positive or negative integers and specify how many particles of species i are created (+) or destroyed (-) in a reaction. To avoid changes which are only due to density changes we use abundances rather than number densities. The abundance Y_i of a nucleus i is defined as

$$Y_i = \frac{n_i}{\rho N_A} \qquad \text{and} \qquad \dot{Y_i} = \frac{\dot{n_i}}{\rho N_A} - \frac{n_i}{\rho N_A}\frac{\dot{\rho}}{\rho}. \tag{2.25}$$

The origin of this relation is the definition of the mass fraction X_i of a nuclide i with mass m_i

$$X_i = \frac{\rho_i}{\rho} = \frac{n_i}{\rho N_A} m_i N_A = Y_i A_i. \tag{2.26}$$

Mass fraction and abundance of a nuclide are related via atomic weight. From the definition of the mass fractions it is also clear that they fulfill the relation $\sum_i X_i = 1$. Rewriting Eq.(2.24) in terms of nuclear abundances yields the following set of differential equations

$$\begin{aligned} \dot{Y_i} = &\sum_j N^i_j \lambda_j Y_j + \sum_{j,k} \frac{N^i_{j,k}}{1+\delta_{jk}} \rho N_A \left<\sigma v\right>_{j,k} Y_j Y_k \\ &+ \sum_{j,k} \frac{N^i_{j,k,l}}{1+\Delta_{jkl}} \rho^2 N_A^2 \left<\sigma v\right>_{j,k,l} Y_j Y_k Y_l. \end{aligned} \tag{2.27}$$

This set of equations is usually referred to as *reaction network*. In the next section we will discuss how such a system of coupled differential equations can be solved and which details have to be accounted for.

2.3 Numerical Integration

The nuclear reaction network (Eq.(2.27)) we derived in the previous section, consists of a system of coupled ordinary first-order differential equations (ODE). We can rewrite it in a more compact and general form for the functions y_i, $i = 1, 2, \ldots, N$

$$\frac{dy_i}{dt} = f_i(t, y_1, \ldots, y_N), \tag{2.28}$$

where the functions f_i on the right-hand side are usually known and in our case are given by the change in abundances due to reaction rates.

A problem which involves the solution of ODEs is not completely specified by its equations. In order to solve the problem, we also need boundary conditions. Boundary conditions are algebraic expressions of the values of the functions y_i in (2.28). The nature of these boundary conditions is crucial in determining how to tackle the problem numerically. In general they can be satisfied at specified discrete points, but do not hold between those points, i.e. the differential equations do not automatically preserve them. The differential equations of the reaction network constitute a typical *initial value problem*.

The boundary conditions are such, that all the y_i are given at some initial time t_s and it is desired to find the y_i at some final time t_f, or at some discrete series of points. In postprocessing nucleosynthesis calculations it is very common to use a discrete list of the time evolution of hydrodynamic variables, like temperature and density, and a single initial composition. The integration of the network equations is then performed along these data points.

2.3.1 Euler's Method

The main idea underlying any method for solving an initial value problem is this: rewrite the dy and dt in Eq.(2.28) as finite steps Δy and Δt, and multiply the equations by Δt. This gives algebraic expressions for the functions y_i when the independent variable is stepped by one stepsize Δt. In the limit of very small steps a good approximation to the underlying differential equation is achieved. The literal implementation of this method results in *Euler's method*

$$y_i^{n+1} = y_i^n + hf(t^n, y_i^n), \tag{2.29}$$

which advances a solution y_i from t_n to $t_{n+1} \equiv t_n + h$. The superscript is not to be interpreted as power, but as numbering of the iteration steps. This method is also called *explicit* or *forward* Euler method because the solution y^{n+1} is an explicit function of y^n.

This method, however, is *not* recommended for practical use, but is conceptually important. Because one way or another, all practical methods come down to this same idea: Add small increments, corresponding to derivatives (right-hand sides of the equations) multiplied by stepsizes, to your functions [104].

The formula in Eq.(2.29) is unsymmetric: it advances the solution over an interval h, but the derivative is evaluated only at the beginning of that interval. Thus the step's error is only one power of h smaller than the correction ($O(h^2)$, whereas the correction is $O(h)$), making it *first order* accurate. A method is conventionally called nth order if its error term is $O(h^{n+1})$.

2.3.2 Stiff Equations

Euler's method has several deficiencies that do not recommend it for practical use. Among them: (i) it is not very accurate when compared to other, fancier methods run at the same stepsize and (ii) it is not very stable if the coefficients in the equations are of very different scales. This is a major problem if we want to solve nuclear network equations, since the coefficients of these equations usually span many orders of magnitude. This is because reaction rates have highly nonlinear dependencies on temperature, and because the abundances themselves typically range over many orders of magnitude (which can also be seen in the solar abundances in Figure 1.1). Such a system of differential equations is called stiff. From a mathematical point of view, a set of differential equations $\dot{\boldsymbol{y}} = \boldsymbol{f}(\boldsymbol{y})$ is stiff, if the eigenvalues λ_j of the Jacobian $\partial \boldsymbol{f}/\partial \boldsymbol{y}$ obey the criterion that for negative $\Re(\lambda_j)$ (the real part of the eigenvalues λ_j)

$$\mathcal{S} = \frac{\max|\Re(\lambda_j)|}{\min|\Re(\lambda_j)|} \gg 1 \tag{2.30}$$

for $j = 1, \ldots, N$ [56]. In astrophysics, $\mathcal{S} > 10^{15}$ is not uncommon. A definition of stiff more closely related to physics would be that the abundance of at least one nuclide changes on a much faster timescale (see Eq.(2.9)) than the abundance of another isotope. From that argument arises one of the major problems relating to stiff equations: in order to ensure stability we have to follow the variation in the solution on the shortest timescale, whereas accuracy requirements would allow a much bigger timestep. Or in other words, the size of the timestep is limited by numerical stability rather than accuracy.

A simple modification of the explicit Euler method helps us bypass this limitation. If we evaluate the derivative at the new timestep t^{n+1}, instead of t^n, the explicit Euler method Eq.(2.29) turns into

$$y_i^{n+1} = y_i^n + hf(t^{n+1}, y_i^{n+1}). \tag{2.31}$$

This method is also called the *implicit* or *backward* Euler method. To illustrate how this cures the problem, consider the single equation

$$f(y) = -cy, \tag{2.32}$$

where $c > 0$ is a constant. The explicit Euler scheme to integrate this equation with stepsize h is

$$y^{n+1} = y^n + hf(y^n) = (1 - ch)y^n. \tag{2.33}$$

The method is clearly unstable if $h > 2/c$, because then $|y^n| \to \infty$ as $n \to \infty$. Whereas for $h = 2/c$ the solution oscillates between $+y^0$ and $-y^0$ where y^0 denotes the initial value and the sign is given by $(-1)^n$ (here the superscript refers to the power). Only for $h < 2/c$ the correct solution $y^n = 0$ is achieved for $n \to \infty$.

Applying the implicit Euler method with timestep h to Eq.(2.32) yields

$$y^{n+1} = y^n + hf(y^{n+1}) = \frac{y^n}{(1+ch)}. \tag{2.34}$$

This method is absolutely stable. Even as $h \to \infty$, $y^{n+1} \to 0$, which is in fact the correct solution of the differential equation. In case of time integration, the implicit method converges to the true equilibrium solution (i.e. the solution at late times) for large stepsizes. This nice feature of implicit methods only holds for systems with linear coefficients. But even in the general case, implicit methods give better stability. Of course, we give up *accuracy* in following the solution towards equilibrium, but we maintain *stability.*

Even though we eliminated the stability issues by using an implicit method, the backward Euler method is still only first order accurate. We will discuss this flaw when applying the integration scheme to the nuclear network equation and argue why this method is nevertheless our method of choice.

2.3.3 Newton-Raphson Iteration

For a general system of differential equations with nonlinear and non-constant coefficients we can rewrite Eq.(2.28) as

$$\frac{d\boldsymbol{y}}{dt} = \boldsymbol{f}(\boldsymbol{y}). \tag{2.35}$$

Implict differencing results in rewriting Eq.(2.31) in vector notation

$$\boldsymbol{y}_{n+1} = \boldsymbol{y}_n + h\boldsymbol{f}(\boldsymbol{y}_{n+1}). \tag{2.36}$$

(We resort to indicate the timesteps as subscripts in order not to be confused with powers). In general this is some nasty set of nonlinear equations that has to be solved iteratively at each timestep. By moving all terms of this equation to the left-hand side, we can translate Eq.(2.36) into finding the root of

$$\frac{\boldsymbol{y}_{n+1} - \boldsymbol{y}_n}{h} - \boldsymbol{f}(\boldsymbol{y}_{n+1}) = 0. \tag{2.37}$$

Probably the simplest and most popular root finding algorithm for a nonlinear set of equations is the *Newton-Raphson* method (see e.g. [104]). A typical multidimensional root finding problem gives N functional relations to be zeroed, involving variables x_i, for $i = 1, \ldots, N$

$$G_i(x_1, x_2, \ldots, N) = 0 \qquad i = 1, \ldots, N \tag{2.38}$$

In the neighborhood of the variable vector $\mathbf{x}$ we can expand each of the functions G_i in a Taylor series

$$G_i(\mathbf{x} + \delta\mathbf{x}) = G_i(\mathbf{x}) + \sum_{j=1}^{N} \frac{\partial G_i}{\partial x_j} \delta x_j + O(\delta\mathbf{x}^2). \tag{2.39}$$

The matrix of partial derivatives appearing in the sum is the *Jacobian* matrix $\mathbf{J}$, with entries

$$J_{ij} \equiv \frac{\partial G_i}{\partial x_j}. \tag{2.40}$$

Rewriting (2.39) in matrix notation and neglecting terms of order $\delta \mathbf{x}^2$ gives

$$\mathbf{G}(\mathbf{x} + \delta \mathbf{x}) = \mathbf{G}(\mathbf{x}) + \mathbf{J} \delta \mathbf{x}. \tag{2.41}$$

From this we can derive a set of linear equations for the corrections $\delta \mathbf{x}$, by setting $\mathbf{G}(\mathbf{x} + \delta \mathbf{x}) = 0$, that move each function to zero simultaneously. This corrections are then added to the solution vector

$$\mathbf{x}_{new} = \mathbf{x}_{old} + \delta \mathbf{x}_{old} = \mathbf{x}_{old} - \mathbf{G}(\mathbf{x}_{old}) \cdot \mathbf{J}(\mathbf{x}_{old})^{-1} \tag{2.42}$$

and the process is iterated until convergence is reached.

When applying this to Eq.(2.37) we have to be careful with the subscripts, because we are basically using an iterative method (Newton-Raphson) inside an other iterative method (implicit Euler), and the individual iteration steps of both are usually denoted by subscripts. Thus we will end up with a nested series of iterations. In order to avoid misconceptions we will keep the subscripts n and $n+1$ for the timesteps of the implicit integration and use superscripts *new* and *old* for subsequent Newton-Raphson iteration steps. Rewriting Eq.(2.42) for the desired solution vector $\boldsymbol{y}_{n+1}^{new}$ yields

$$\boldsymbol{y}_{n+1}^{new} = \boldsymbol{y}_{n+1}^{old} - \left(\frac{\boldsymbol{y}_{n+1}^{old} - \boldsymbol{y}_n}{h} - \boldsymbol{f}(\boldsymbol{y}_{n+1}^{old}) \right) \cdot \mathbf{J}(\boldsymbol{y}_{n+1}^{old})^{-1} \tag{2.43}$$

where the Jacobian $\mathbf{J}(\boldsymbol{y}_{n+1}^{old})$ is the derivative of Eq.(2.37) with respect to $\boldsymbol{y}_{n+1}^{old}$

$$\mathbf{J}(\boldsymbol{y}_{n+1}^{old}) \equiv \frac{\mathbf{1}}{h} - \frac{\partial \boldsymbol{f}(\boldsymbol{y}_{n+1}^{old})}{\partial \boldsymbol{y}_{n+1}^{old}} \tag{2.44}$$

which itself contains the Jacobian of the functional of time integration.

The Newton-Raphson method provides a very efficient mean of converging to a root, given that the initial guess is sufficiently good. If the timestep is not too big ,or in other words sufficiently small, already one iteration of the Newton-Raphson method may be enough to reach the desired convergence level. In other words, at each timestep we have to invert the Jacobian in order to find $\boldsymbol{y}_{n+1}$. We will see below how we can ensure stability and accuracy by choosing an appropriate timestep and a good initial guess.

2.3.4 Solving the Reaction Network Equations

We will now apply the implicit Euler method to our problem of a nuclear reaction network, and explain our motivation to use this scheme. For a given set of nuclear abundances $\mathbf{Y}$ the time-derivative $\dot{\mathbf{Y}}$ can be calculated using Eq.(2.27). The desired solution is the abundance at a future time, $\mathbf{Y}(t + \Delta t)$, where Δt is the network timestep (we also denote this as h). By doing this, the implicit Euler method Eq.(2.31) translates into

$$\mathbf{Y}(t+\Delta t)=\mathbf{Y}(t)+\Delta t\dot{\mathbf{Y}}(t+\Delta t). \tag{2.45}$$

Following the prescription above, we solve this by transforming it into a root-finding problem and applying the Newton-Raphson scheme. Thus Eq.(2.43) can be written as

$$\mathbf{Y}^{new}(t+\Delta t)=\mathbf{Y}^{old}(t+\Delta t)-\left(\frac{\mathbf{Y}^{old}(t+\Delta t)-\mathbf{Y}(t)}{\Delta t}-\dot{\mathbf{Y}}^{old}(t+\Delta t)\right)\cdot\tilde{\mathbf{J}}^{-1}. \tag{2.46}$$

In order to solve this equation we have to invert the Jacobian $\tilde{\mathbf{J}}$

$$\tilde{\mathbf{J}}\equiv\frac{\mathbf{1}}{\Delta t}-\frac{\partial\dot{\mathbf{Y}}(t+\Delta t)}{\partial\mathbf{Y}(t+\Delta t)} \tag{2.47}$$

at each iteration step. We will discuss the detailed structure of the Jacobian and how we can take advantage of it in the next section. For now we put the focus on how to ensure stability and accuracy.

The relatively simple implicit Euler scheme has a comparably low computational cost per timestep [130]. In order to get a solution within an iteration we only need one evaluation of the right-hand side, one matrix inversion and on backsubstitution. This makes it the preferred method for cost efficient calculations. Higher order methods are always computationally more involved, but have the advantage that we get an estimate of the accuracy of a timestep, which is not the case for our first order method. In order to compensate for that shortcoming, we check at every iteration for mass conservation

$$\sum_{i=1}^{n}X_i=1, \tag{2.48}$$

where the X_i are the dimensionless mass fractions (Eq.(2.48)). In practice, we demand that the difference between the sum over all massfractions and 1 is less then a certain threshold (usually 10^{-7}). If Eq.(2.48) is violated, an additional Newton-Raphson step is performed, or, if convergence is not reached within 3-4 iterations, the time step is cut in half and the time integration restarted with the new timestep. Satisfying Eq.(2.48) also prevents an unphysical buildup (or decay) of abundances over long timescales.

Since every rejection of a timestep results in additional computational effort, we are encouraged to choose the timestep in such a way, that convergence is reached as fast as possible. We implemented the adaptive timestep calculation proposed in [12]

$$\Delta t\leq\eta\frac{Y_i}{dY_i/dt}, \tag{2.49}$$

η is a constant less than unity (we used $\eta=0.1$ for all calculations) and only nuclei, whose abundance is bigger than 10^{-10} are taken into account. Additionally, we make sure, that the thermodynamic variables do not change more than 5% within a timestep. Furthermore, the growth of the timestep is limited to a factor of two for subsequent steps.

The convergence of the Newton-Raphson scheme depends strongly on the initial guess. Choosing the abundances from the previous timestep $\mathbf{Y}(t)$ as an initial guess for the desired abundances, Eq.(2.46) turns into

$$\mathbf{Y}^0(t + \Delta t) = \mathbf{Y}(t) + \dot{\mathbf{Y}}(t + \Delta t) \cdot \tilde{\mathbf{J}}^{-1}. \tag{2.50}$$

For the evaluation of the time derivative at $t + \Delta t$, density and temperature (needed to calculate the reaction rates in Eq.(2.27) are taken at the new timestep whereas the abundances correspond to the previous timestep. This method is very common in nucleosynthesis calculations and using an appropriate solver usually converges using only one Newton-Raphson iteration step. A discussion and comparison of different solvers and their application in nucleosynthesis calculation can be found in [130].

2.4 Taking Advantage of Matrix Sparseness

A we have seen in the previous section, our numerical integration scheme involves at least one inversion of a $N \times N$ Matrix. Since the inversion of a dense matrix scales as $O(N^3)$ solving our system of differential equations gets more and more involved as N gets bigger. For r-process calculations we can easily reach network sizes of $N \sim 6000 - 7000$. Furthermore, the Jacobian matrices that arise from nuclear reaction networks are not positive definite or symmetric, since the forward and backward reactions are in general not equal.

In theory, the matrix should be completely dense, since every nuclide can react with itself and each of the hundreds or thousands of others. But in practice it is possible to neglect most of this reactions. Because of the $Z_i Z_j$ dependence of the repulsive Coulomb term in the nuclear potential, reactions with free neutrons or isotopes of Hydrogen and Helium on heavy nuclei occur on much faster timescales than fusion of heavier nuclei. Additionally, since the kinetic energy needed for nuclei to overcome the Coulomb barrier increases with growing charge number, heavy nuclei would actually be photodisintegrated much faster than heavy ion fusion would occur. For example, at temperatures of $\sim 5 \cdot 10^9 K$, where the kinetic energy of ^{28}Si nuclei would be sufficiently high for $^{28}\mathrm{Si} + ^{28}\mathrm{Si}$-fusion to occur, it is far more likely that the silicon nuclei are photodisintegrated. In the same manner, photodisintegrations tend to eject free nucleons or α-particles. Thus, with a few exceptions, for each nuclide we only have to consider 12 reactions linking it to its neighbors via capture of a n, p, α or γ, and release of a different one of these four. The exceptions are the few reactions with heavy ions, important for stellar burning phases like carbon or oxygen burning, where the lack of light elements causes heavy ion fusion reactions to dominate.

For the example case of a 300 nuclei network (consisting of all isotopes from hydrogen to chloride, ranging from the proton to the neutron dripline) Figure (2.1) illustrates the sparseness pattern of the resulting Jacobian matrix. Of the 90000 entries, less than 5000 are nonzero. It is obvious, that entries are predominantly located at borders and the diagonal. In the standard classification of sparse matrices, this matrix could best be described as doubly bordered band diagonal. The width of the side and diagonal bands depends strongly on the choice of network. Since the nuclides are ordered by element and since reactions involving α-particles link next but one neighboring elements, the width of the diagonal ΔD is approximately 4 times the mean number of isotopes per element. In our example, ΔD is 136, but for large networks it can also reach values of ~ 400. The width of the sideband ΔB is given by the location of the heaviest fusion

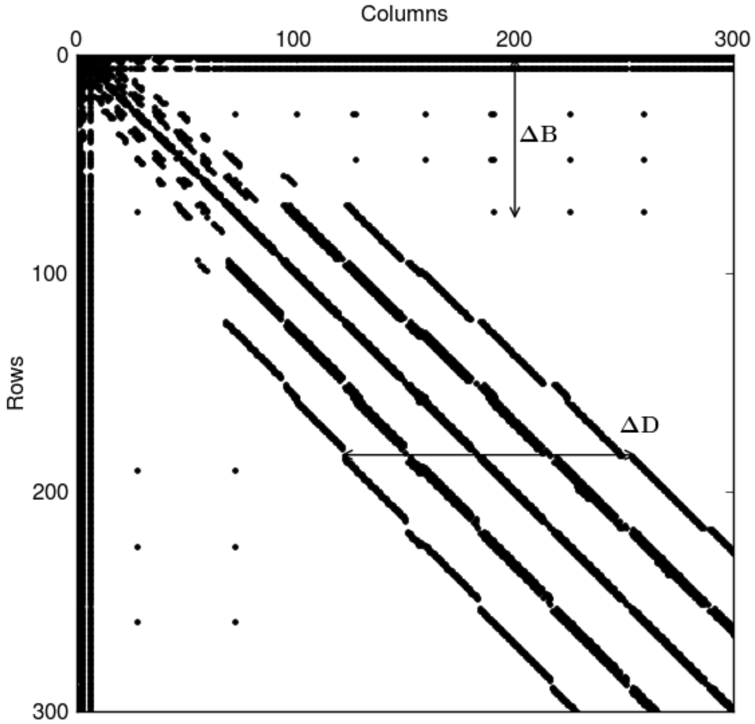

Figure 2.1: Graphical representation of the sparseness of the Jacobian Matrix. The dots indicate nonzero elements.

partner in the series of nuclei that comprise the network (here $\Delta B = 72$). For larger networks, the value of ΔB does not increase by much, because heavy ion fusion is only possible for a limited number of elements.

2.4.1 Sparse Matrix Solver

The inversion of the Jacobian consumes most of the computational time, so there is clearly a need for custom tailored solvers that take advantage of the sparseness of the matrix. For small networks ($N < 100$), the best results are obtained with machine optimized dense solvers (e.g. LAPACK), since the sparseness is less pronounced. For larger matrices, there is a variety of solvers available (see e.g. [130]). In an intermediate regime ($N \leq 2000$), good results are achieved with a solver taking advantage of the doubly bordered band diagonal structure, which is getting more and more inefficient as the density of entries decreases with increasing network size. Already for the small example above, the bands contain almost 40000 entries, of which only ~5000 are nonzero. In order to perform large scale calculations we had to use a different solver. We decided to use PARDISO [115, 116] a *thread-safe, high-performance, robust, memory efficient and easy to use software for solving large sparse symmetric and unsymmetric linear systems of equations on shared-memory and distributed-memory multiprocessors*[1]. We will not go into the details of how the solver works but an additional benefit comes from the fact that it uses an efficient sparse matrix storage format.

2.4.2 Compressed Sparse Column Format

For an efficient computation it is not only important which solver to use, even though this accounts for the main part of computational time, but also how the Jacobian matrix is stored throughout the program. We have to consider that the Jacobian has to be set to zero at the beginning of each iteration step, since the nonzero entries are added one by one. For a sparse matrix, where usually less than 1% of the entries are nonzero, most of the assignments are unnecessary. The easiest way to counteract this waste of computational time would be to store only the nonzero entries. In [113] we can find different storage schemes to achieve this. One of the most popular, which is also used by PARDISO, is the *compressed sparse column format* (cscf).

We will demonstrate the scheme, following the example in [113]: The matrix

$$A = \begin{pmatrix} 1. & 0. & 0. & 2. & 0. \\ 3. & 4. & 0. & 5. & 0. \\ 6. & 0. & 7. & 8. & 9. \\ 0. & 0. & 10. & 11. & 0. \\ 0. & 0. & 0. & 0. & 12. \end{pmatrix}$$

with Nz nonzero elements, can be stored in three arrays

AA	1.	3.	6.	4.	7.	10.	2.	5.	8.	11.	9.	12.
JA	1	2	3	2	3	4	1	2	3	4	3	5
IA	1	4	5	7	11	13						

with the following functions:

- The real array AA contains the real values a_{ij} stored column by column, from column 1 to n. The length of AA is Nz
- The integer array JA contains the row indices i of the elements a_{ij} as stored in the array AA. The length of JA is Nz.
- The integer array IA contains the pointers to the beginning of each column in the arrays AA and JA. Thus, the content of $IA(i)$ is the position in arrays AA and JA where the i-th column starts. The length of IA is $n+1$ with $IA(n+1)$ containing the number $IA(1)+Nz$, i.e. the address in AA and JA of the beginning of a fictitious column number $n+1$.

Using this scheme, the process of setting the full Jacobian to zero at every iteration is reduced to Nz assignments. Since the nonzero pattern of the Jacobian does not change much over time, the arrays JA and IA only need small modifications. To get an estimate of the computational savings, we can compare the time needed to set a 6500×6500 matrix to zero and, assuming that 1% of the entries are nonzero, the time it takes to set an array of length 422500 to zero. The computational time needed is a factor 100 lower in the latter case, which means that the time needed to set an array or a matrix to zero depends linearly on the number of assignments that have to be performed.

When switching from a full matrix representation to a compressed storage format, it is necessary to know for every reaction, which entries in AA have to be modified, i.e. which position in AA represents $\partial\dot{Y}_i/\partial Y_j$ for given i and j. We solve this problem by creating once, in the beginning, the full Jacobian, where every possible nonzero entry is set to one. This matrix is then translated into cscf and we assign to every nonzero entry in the Jacobian its position in AA. Simultaneously the position of the diagonal elements in AA are stored in a separate array. In a last step we assign to every nuclide in a reaction the positions in AA where its Jacobian entries are located. For example considering the reaction $k + l \to o + p$ we have to store for the target k the position of $\partial\dot{Y}_k/\partial Y_k$ and $\partial\dot{Y}_k/\partial Y_l$. In the same manner the locations of the derivatives of the other nuclides with respect to Y_k and Y_l have to be known. Despite the additional memory needed to store this information, using a compressed sparse storage format is much more memory saving and computationally efficient.

2.5 Nuclear Statistical Equilibrium

We can also take advantage of nuclear properties (rather than computational), to simplify the solution of the network equations (Eq.(2.27)). At temperatures high enough, every nucleus in an astrophysical plasma is connected to every other by bidirectional reaction links. Capture reactions can take place, because the temperature is high enough to overcome coulomb barriers. In the inverse direction, photodisintegrations occur due to the high-energy tail of photons in a Planck distribution at high temperatures. Under such conditions a complete chemical equilibrium is established. In such an equilibrium, also called *nuclear statistical equilibrium* (NSE), the chemical potentials fulfill

$$\begin{aligned} \bar{\mu}\,(Z,N) + \bar{\mu}_n &= \bar{\mu}\,(Z,N+1) \\ \bar{\mu}\,(Z,N) + \bar{\mu}_p &= \bar{\mu}\,(Z+1,N) \end{aligned} \tag{2.51}$$

for individual proton and neutron captures. In the same manner we can create a nucleus (Z,N) via N neutron and Z proton captures equivalent to

$$N\bar{\mu}_n + Z\bar{\mu}_p = \bar{\mu}\,(Z,N) = \bar{\mu}_{Z,N}. \tag{2.52}$$

Assuming once again, that nuclei and nucleons obey Maxwell-Boltzmann statistics, the chemical potentials given as

$$\bar{\mu}_i = k_B T \ln\left(\frac{\rho N_A Y_i}{G_i}\left(\frac{2\pi\hbar^2}{m_i k_B T}\right)^{3/2}\right) + m_i c^2. \tag{2.53}$$

Putting this into Eq.(2.52) and solving for the abundance $Y\,(Z,N)$ we get

$$Y\,(Z,N) = G_{Z,N}\,(\rho N_A)^{A-1}\,\frac{A^{3/2}}{2^A}\left(\frac{2\pi\hbar^2}{m_u k_B T}\right)^{\frac{3}{2}(A-1)} \exp\left(\frac{B_{Z,N}}{k_B T}\right) Y_n^N Y_p^Z, \tag{2.54}$$

where $G_{A,Z}$ is the partition function and $B_{A,Z} = (Nm_n + Zm_p - m_{Z,N})\,c^2$ the binding energy of nucleus (Z,N). Additionally, we assume that $A = N + Z$, $m_n \approx m_p \approx m_u$ and $m_{Z,n} \approx Am_u$. The same equation can also be derived using detailed balance

Eq.(2.10) for a series of N neutron captures and Z proton captures (see e.g. [23]).

We see that the nuclear abundances in Eq.(2.54) do not depend on individual reaction rates, but only on temperature, density, partition functions and binding energies. Quantities which are better known than many reaction rates [55]. From this equation we can already guess the abundance distribution at certain conditions. At high temperatures, the term $(k_BT)^{-\frac{3}{2}(A-1)}$ dominates, and free nucleons and small nuclei are favored, since the Planck distribution contains high-energy photons, which photodisintegrate heavier nuclei. At high densities, due to the $(\rho N_A)^{A-1}$ term, large nuclei are favored, since for a given cross section, the number of collisions is enhanced. Under intermediate conditions, where $\exp\left(\frac{B_{Z,N}}{k_BT}\right)$ dominates, tightly bound nuclei are most abundant. These nuclei are found in the vicinity of ^{56}Fe, where the binding energy per nucleon is at its maximum (see Figure 2.2).

In order to solve Eq.(2.54) for the detailed NSE abundances, we need two additional constraints for the determination of the free proton and neutron abundances Y_n and Y_p. These are the total mass conservation Eq.(2.48) and the definition of the electron fraction Y_e

$$Y_e = \sum_i Z_i Y_i. \tag{2.55}$$

We solve these equations for free neutron and proton abundances using a 2 dimensional Newton-Raphson iteration scheme similar to the one derived in Section (2.3.3). We can rewrite Eqs.(2.48) and (2.55) using the abundances $Y\left(Y_n, Y_p\right)$ from Eq.(2.54)

$$\begin{aligned} f\left(Y_n, Y_p\right) &= \sum_i Z_i Y_i\left(Y_n, Y_p\right) - Y_e \\ g\left(Y_n, Y_p\right) &= \sum_i A_i Y_i\left(Y_n, Y_p\right) - 1 \end{aligned} \tag{2.56}$$

which both should be equal to zero. The abundances $Y_n^{(n+1)}$ and $Y_p^{(n+1)}$ at iteration step $n+1$ are then given by [104]

$$\begin{pmatrix} Y_n^{(n+1)} \\ Y_p^{(n+1)} \end{pmatrix} = \begin{pmatrix} Y_n^{(n)} \\ Y_p^{(n)} \end{pmatrix} - \begin{pmatrix} \frac{\partial f^{(n)}}{\partial Y_n^{(n)}} & \frac{\partial f^{(n)}}{\partial Y_p^{(n)}} \\ \frac{\partial g^{(n)}}{\partial Y_n^{(n)}} & \frac{\partial g^{(n)}}{\partial Y_p^{(n)}} \end{pmatrix}^{-1} \begin{pmatrix} f^{(n)} \\ g^{(n)} \end{pmatrix}. \tag{2.57}$$

For better readability we replaced $f\left(Y_n^{(n)}, Y_p^{(n)}\right)$ and $g\left(Y_n^{(n)}, Y_p^{(n)}\right)$ with $f^{(n)}$ and $g^{(n)}$. The derivatives needed for the Jacobian can be calculated straightforwardly

$$\begin{aligned} \frac{\partial f}{\partial Y_n} &= \frac{\sum_i Y_i Z_i N_i}{Y_n} \quad , \frac{\partial f}{\partial Y_p} = \frac{\sum_i Y_i Z_i^2}{Y_p} \\ \frac{\partial g}{\partial Y_n} &= \frac{\sum_i Y_i A_i N_i}{Y_n} \quad , \frac{\partial g}{\partial Y_p} = \frac{\sum_i Y_i A_i Z_i}{Y_p}. \end{aligned} \tag{2.58}$$

Using the well known algebraic formula to calculate the inverse of a 2 × 2 matrix we

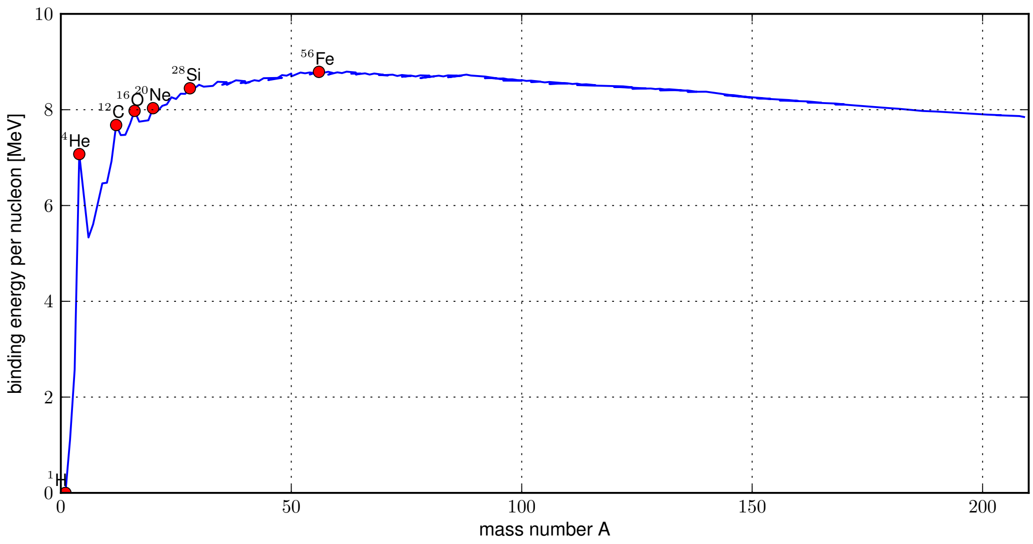

Figure 2.2: Average nuclear binding energy per nucleon of stable isotopes, based on data from [15]. Courtesy of U. Frischknecht.

can easily solve Eq.(2.57) to give

$$\begin{aligned} Y_n^{(n+1)} &= Y_n^{(n)} - \frac{1}{D}\left(\frac{\partial f^{(n)}}{\partial Y_p^{(n)}} g^{(n)} - \frac{\partial g^{(n)}}{\partial Y_p^{(n)}} f^{(n)}\right) \\ Y_p^{(n+1)} &= Y_p^{(n)} - \frac{1}{D}\left(\frac{\partial g^{(n)}}{\partial Y_n^{(n)}} f^{(n)} - \frac{\partial f^{(n)}}{\partial Y_n^{(n)}} g^{(n)}\right) \end{aligned}, \tag{2.59}$$

where $D = \frac{\partial f}{\partial Y_n}\frac{\partial g}{\partial Y_p} - \frac{\partial f}{\partial Y_p}\frac{\partial g}{\partial Y_n}$ is the determinant of the Jacobian. Convergence is reached, when both equations in Eq.(2.56), as well as the change in free neutron and proton abundance over one iteration step are smaller than a certain tolerance level (usually around 10^{-6}).

We note, that in most cases where the fast reactions governed by the strong and electromagnetic force reach equilibrium, the reactions governed by the weak force do not. Since these reactions are the only ones to change Ye, i.e. the electron fraction or equivalently, the total (not the free) proton fraction, they have to be considered explicitly, even in NSE. Thus, a limited reaction network consisting only of reactions described by Eqs.(2.18) and (2.20) has to be solved alongside the NSE equations.

In general it is assumed that complete NSE is established at temperatures $T \gtrsim 6$ GK [56, 79]. At lower temperatures, NSE breaks down, as soon as the slowest reactions are not in equilibrium anymore. Then, a *quasi-statistical equilibrium* (QSE) is established, where different regions on the nuclear chart are still in equilibrium, but connected via reactions that are not in equilibrium anymore (for more information about QSE see e.g. [29, 56, 79]). We do not use the QSE approximation in our code but switch from NSE directly to the full network. For our calculations we will use a rather conservative limit of $T = 9$ GK. Since we use reaction rates where forward and inverse direction are connected via detailed balance, equilibrium is also maintained when solving the network equation Eq.(2.27). Besides being computationally less costly, there are further benefits from NSE. It gives us the possibility to follow the abundance evolution at temperatures beyond 10 GK (this limit is imposed by the reaction rate fits, which are only valid up to this temperature (see Section 2.6.1). Additionally, assuming NSE, we can calculate an abundance distribution for a given set of temperature, density and Y_e using $Y_p = Y_e$ and $Y_n = 1 - Y_p$ as initial values.

2.6 Implementation of Reaction Rates

In section 2.1 we presented the theoretical background for the various kinds of reactions occuring in an astrophysical plasma. The expressions that were derived are usually not calculated within reaction network calculation. Instead, depending on the character of a reaction, one uses directly reaction rates, half-lives or transition probabilities. The combination of different reaction channels is not always trivial, and some reactions, in fact, even require a special treatment in order to be applicable in network calculations. In this section we first present the standard method how reaction rates are implemented, as well as the implementation of the more involved types of reactions.

2.6.1 Reaclib

In general, reaction rates, experimental as well as theoretical ones, are published in tables as function of temperature. In course of a nucleosynthesis calculation these reaction rates have to be evaluated thousands of times at varying temperatures, which would make interpolating in these tables a rather cumbersome task. In order to facilitate the calculation of reaction rates, we will use the well accepted and widespread REACLIB parametrization [129]

$$\left.\begin{array}{r} N_A \langle \sigma v \rangle \\ \lambda_\gamma \end{array}\right\} = \exp(a_0 + a_1 T_9^{-1} + a_2 T_9^{-1/3} + a_3 T_9^{1/3} + a_4 T_9 + a_5 T_9^{5/3} + a_6 \ln(T_9)), \tag{2.60}$$

with seven open parameters $a_0 - a_6$, and temperature T_9 given in units of 10^9 K. The parametrization proves to be flexible enough to accommodate the different temperature dependencies of the various reaction types across the fitted temperature range $0.01 \leq T_9 \leq 10$ [129]. Whenever possible we use reaction rates from compilations, which are already in this parametrization, e.g. [110, 99] or convert those, which are not, like [86]. In this thesis, we only do this for constant decay rates, for which the conversion reduces to

$$a_0 = \ln\left(\frac{\ln(2)}{\tau_{1/2}}\right) \tag{2.61}$$

$$a_1 - a_6 = 0. \tag{2.62}$$

Another integral part of any REACLIB reaction rate compilation are partition functions for all involved nuclei. As we already pointed out in Section 2.1, reverse reactions are calculated using detailed balance. Using temperature dependent partition functions $\tilde{G}_i(T)$ normalized to the ground state degeneracy $g_i = \left(2J_i^0 + 1\right)$ we can rewrite

Eq.(2.12) for the inverse direction

$$N_A \left\langle \sigma v \right\rangle_{m;o,j} = \left(\frac{A_i A_j}{A_o A_m} \right)^{3/2} \frac{g_i g_j}{g_o g_m} \frac{\tilde{G}_i\left(T\right)}{\tilde{G}_m\left(T\right)} e^{-Q_{i;j,o}/k_B T} N_A \left\langle \sigma v \right\rangle_{i;j,o} . \tag{2.63}$$

The spin and mass factors, and the exponential factor are accounted for in the parameters a_0^{rev} and a_1^{rev} of the reverse rate respectively. The only factor which has to be taken into account explicitly, is the ratio of the partition functions of the final nucleus and the target. To calculate the actual (endoergic) reaction rate, the reverse fit has to be multiplied by $\tilde{G}_i\left(T\right)/\tilde{G}_m\left(T\right)$ at the appropriate temperature. Normalized partition functions are available in tabular form at 20 temperatures in the range $0.1 \leq T_9 \leq 10$ [110] and at higher temperatures on a grid of 48 temperatures in the range $12 \leq T_9 \leq 275$ [106]. To get consistent results, the same partition functions have to be used in NSE as well.

2.6.2 Electron and Positron Captures

Electron and positron capture calculations have been performed by [47, 48, 49] for nuclei with $A \leq 45$ (*sd*-shell) and by [70] for $45 < A \leq 65$ (*pf*-shell). Initially (in [47, 48]) the rates, the capture rates as well as the corresponding β decays, have been calculated on a grid of temperature and ρY_e (in gcm^{-3}) points, i.e. for temperatures (in 10^9 K) 0.01, 0.1, 0.2, 0.4, 0.7, 1, 1.5, 2, 3, 5, 10, 30 and 100, and for all integer values of $\log\left(\rho Y_e\right)$ between 1 and 11. Unfortunately, the extreme sensitivity of the capture rates to variations of temperature or density makes interpolation between this grid points rather inaccurate. In the newer tables [49, 70], the capture rates are replaced by so called *effective log-ft* values, which are defined by introducing an effective phase space integral I for ground-state to ground-state transitions, which approximates to first order the temperature and density dependence of the rates [70]. The "decay constant" in Eq.(2.18) is then given by

$$\lambda = \ln\left(2\right) \frac{I}{\left\langle ft \right\rangle} \tag{2.64}$$

where $\left\langle ft \right\rangle$ is the tabulated effective rate. The phase space integral is defined as

$$I = \int_{w_0}^{\infty} w^2 \left(Q_{00} + w\right)^2 S\left(w\right) dw. \tag{2.65}$$

Q_{00} is the ground-state to ground-state transition energy or Q-value of the reaction and w_0 is the maximum of 1 and $-Q_{00}$. Depending on the reaction, S is the Fermi-Dirac distribution of the electron (S_e) or of the positron (S_p), with Temperature T and chemical potential μ. For electrons

$$S_e = \frac{1}{\exp\left(\frac{w m_e c^2 - \mu_e}{k_B T}\right) + 1}, \tag{2.66}$$

and the positron distribution is defined similarly with $\mu_p = -\mu_e$. The chemical potentials are calculated using a table based on the Helmholtz equation of state [131] (The table and a helpful subroutine can be found in [2]). The integral is evaluated using a numerical method provided by the *numerical algorithms group* [3].

2.6.3 β-delayed Neutron Emission

In the β transition of a neutron-rich precursor nucleus, a neutron-unbound excited state in the daughter nucleus can be populated. The decay of this unbound state can result in emission of either a neutron, a gamma-ray or even a conversion electron. In the case of a neutron, the process is called *β-delayed neutron emission*. The corresponding energy window is given by

$$\Delta E = Q_\beta - S_n,$$

where Q_β is the precursor β decay energy and S_n is the neutron separation energy in the daughter nucleus. Move away from stability, towards neutron-rich nuclei, Q_β typically gets larger and S_n typically gets smaller. As the energy window increases so does the probability for delayed neutron emission. For nuclei very far from stability, other decay channels like β-delayed two or even three neutron emission become energetically possible. The neutron emission follows promptly after the decay, thus *delayed* does not mean that the neutron emission channel occurs on a different timescale than the pure decay.

From experiments [15] and theoretical calculations [86], we know the half life $\tau_{1/2}$ and the probabilities p_0, p_1, p_2 and p_3 for the pure decay and β-delayed one, two or three neutron emission respectively. As we have seen in Section 2.1.3 the total β decay rate is determined by the decay constant

$$\lambda^{tot} = \frac{\ln(2)}{\tau_{1/2}}. \tag{2.67}$$

Including the probabilities for the different decay channels, we can calculate individual decay constants for each channel

$$\begin{aligned} \lambda^{\beta} &= \lambda^{tot} p_0 \\ \lambda^{\beta 1n} &= \lambda^{tot} p_1 \\ \lambda^{\beta 2n} &= \lambda^{tot} p_2 \\ \lambda^{\beta 3n} &= \lambda^{tot} p_3 \end{aligned} \tag{2.68}$$

The corresponding reactions are simply

$$(A, Z) \to (A - \eta, Z + 1) + \eta n \tag{2.69}$$

where η is the number of beta-delayed neutrons.

2.6.4 Fission

The implementation of fission rates into the network code focuses on two different challenges: The different kinds of fission have to be treated differently depending on their origin and the fission fragment mass distribution has to be accounted for. We will first discuss the treatment of the different types of fission and then our simplified model for the fission fragment mass distribution, since this is the same for all fission reactions.

The different kinds of fission, which can be incorporated in the network, are spontaneous fission (SF), β-delayed fission (BF) and neutron-induced fission (NF):

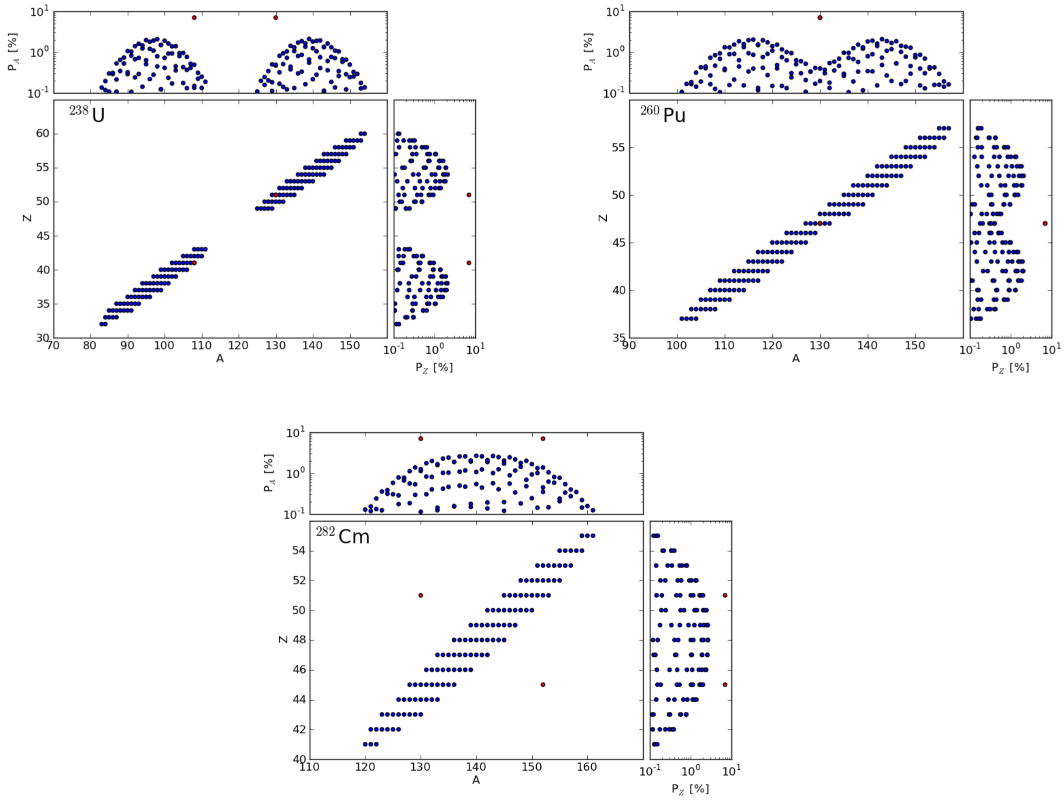

Figure 2.3: The final mass distributions of fission fragments for the compound nuclei (after neutron capture or β-decay) ^{238}U, ^{260}Pu and ^{282}Cm. The blue dots show the distribution and probabilities calculated with the parametrisation from [66], the red dots represent the parametrisation from [98] where the probabilities are set to 7% for illustration.

- SF: $(\mathrm{A}, \mathrm{Z}) \rightarrow (\mathrm{A}_1, \mathrm{Z}_1) + (\mathrm{A}_2, \mathrm{Z}_2) + \eta_n$
- BF: $(\mathrm{A}, \mathrm{Z}) \rightarrow (\mathrm{A}, \mathrm{Z}+1) \rightarrow (\mathrm{A}_1, \mathrm{Z}_1) + (\mathrm{A}_2, \mathrm{Z}_2) + \eta_n$
- NF: $\mathrm{n} + (\mathrm{A}, \mathrm{Z}) \rightarrow (\mathrm{A}+1, \mathrm{Z}) \rightarrow (\mathrm{A}_1, \mathrm{Z}_1) + (\mathrm{A}_2, \mathrm{Z}_2) + \eta_n$

where η_n represents the neutrons, which are emitted during the fission process. The intermediate nuclei in the case of neutron-induced and β-delayed fission are just for illustration and not explicitly taken into account in the implementation. We will refer to the nucleus (A,Z) on the left-hand side of the arrow as mother nucleus and the ones on the right-hand side as daughter nuclei.

In the case of spontaneous fission the reaction rate can simply be treated as a decay rate, which is derived from a half life. The change in abundance of the mother nucleus is then given as

$$\dot{Y}(\mathrm{A}, \mathrm{Z}) = -\lambda^{SF} Y(\mathrm{A}, \mathrm{Z}) = -\frac{ln(2)}{\tau_{1/2}^{SF}} Y(\mathrm{A}, \mathrm{Z}). \tag{2.70}$$

For β-delayed fission, the calculation is a little more involved. The mother nucleus first undergoes a β-decay into an intermediate nucleus which then fissions into the daughter nuclei. Thus the fission channel competes with the other decay channels like β-delayed

(1-, 2-, 3-) neutron emission, β-delayed α-emission or the pure β decay. The BF rates are usually not given as half lifes but only as branching ratios P^{BF}. That means that they have to be incorporated into the already present beta decay rates. We do this by replacing the total rate in Eq.(2.67) by an effective rate

$$\lambda^{eff} = \lambda^{tot} - \lambda^{BF}, \tag{2.71}$$

with

$$\lambda^{BF} = \lambda^{tot} \cdot P^{BF}. \tag{2.72}$$

We point out, that by doing this, the β-decay rates in Eq.(2.68) are reduced.

In neutron-induced fission, the fission process is preceded by a neutron capture. Like in regular neutron captures, the reaction rate $N_A \langle\sigma v\rangle^{NF}$ is temperature dependent and given in the Reaclib parametrization (Eq. (2.60)). The resulting change in abundance of the mother nucleus is thus given as

$$\dot{Y}(\mathrm{A},\mathrm{Z}) = -\rho N_A \langle\sigma v\rangle^{NF} Y(\mathrm{A},\mathrm{Z}) Y_{\mathrm{n}}. \tag{2.73}$$

The proper inclusion of fission in a network code also requires the knowledge of the mass distribution of the fission fragments, which enter the network as reaction products. In principle, such distributions are complicated functions, depending on the properties of the involved nuclei, and have to be calculated for each nuclide individually. Since the realistic calculation of fission fragment mass distributions would go beyond the scope of this thesis we resort to two different empirical parametrizations.

The first, much simpler parametrization was described in [98]:

There it is considered, that 100% symmetric fission only occurs for a small region of nuclei [57] with $255 < \mathrm{A} < 265$. For symmetric fission the mass and charge number of the heavy fragment are given as

$$\mathrm{A}_1 = \frac{\mathrm{A}}{2} \quad , \quad \mathrm{Z}_1 = \frac{\mathrm{Z}}{2}. \tag{2.74}$$

The light fragment can be determined from mass and charge conservation

$$\mathrm{A}_2 = \mathrm{A} - \mathrm{A}_1 \quad , \quad \mathrm{Z}_2 = \mathrm{Z} - \mathrm{Z}_1. \tag{2.75}$$

All other fission processes occur asymmetrically, and the fission products are distributed as in [58], where it is assumed, that the most probable fragment has mass A=130 and is close in nucleon composition to the double-magic ^{132}Sn (Z=52, N=80):

$$\begin{aligned} \mathrm{A}_1 = 130 \quad &, \quad \mathrm{Z}_1 = 52 - \frac{\mathrm{Z} - 80}{10} \\ \mathrm{A}_2 = \mathrm{A} - \mathrm{A}_1 \quad &, \quad \mathrm{Z}_2 = \mathrm{Z} - \mathrm{Z}_1. \end{aligned} \tag{2.76}$$

We plotted the resulting distribution in Figure (2.3) as red dots. We set the probability to 7% in order to be able to compare the distributions, in reality, however, the probability in this parametrization is always 100%. The main advantage of this parametrisation is, that for every fissioning nuclide we get a distinct pair of daughter nuclei, which is easy to implement and computationally very cheap. On the other hand, it might be an over-simplification of the problem. We also have to note, that with the requirement for one fragment ($\mathrm{A_1}$) to be close to ^{132}Sn, the complication arises, that for heavy nuclides ($\mathrm{A} > 265$) the second fragment is heavier ($\mathrm{A_2} > \mathrm{A_1}$) but less charged ($\mathrm{Z_1} < \mathrm{Z_2}$). This can be seen in Figure 2.3 in the bottom panel. Very neutron rich nuclides are produced, which can release many fission neutrons (see below).

The second parametrization was proposed in [66], where the double-humped mass distribution is approximated by Gaussian functions around the light and heavy peaks ($\mathrm{A_L}$ and $\mathrm{A_H}$ respectively), and the charge distribution by that around the most probable charge for each A-chain, $\mathrm{Z_A}$. The probability, that nucleus (A,Z) is a fragment in the fissioning of $(\mathrm{A_{fis}}, \mathrm{Z_{fis}})$ is given by

$$\begin{aligned} P_{A_{fis},Z_{fis}}(A,Z) = & \frac{\exp\left\{-\left(Z-Z_A\right)^2/c_Z\right\}}{2\pi\sqrt{c_Z c_A}} \\ & \times\left[\exp\left\{-\left(A-A_L\right)^2 c_A\right\}+\exp\left\{-\left(A-A_H\right)^2 c_A\right\}\right], \end{aligned} \tag{2.77}$$

where they assume $A_L = 0.85A_{fis} - 104.98$, $A_H = 0.15A_{fis} + 103.87$, $Z_A = Z_{fis}(A + 0.6)/A_{fis}$, $c_Z = 0.8$ and $c_A = 78$. For all possible combinations of A and Z, $\sum P(A,Z) = 1$ is satisfied. For practical use, we set a lower limit for the probabilities (usually 10^{-2}) and in that case the probabilities have to be renormalized in order to fulfill the unity equality. The second fission fragment is determined from mass and charge conservation as above.

This parametrization is computationally very costly since for every fission reaction several tens of different fragment pairs have to be included into the calculation as individual reactions where the reaction rate is multiplied by the corresponding probability. Already for an optimistic lower limit of 10^{-2}, the number of fission reactions can easily outnumber all other reactions by a factor of two. Moving the lower limit to even smaller numbers this factor will increase further since more reactions per fission reaction have to be considered. A qualitative analysis of the influence of differnet fission channels and fragment mass distributions on the outcome of reaction network calculations will be given in Section 5.2.

When implementing any fragment mass distribution into the network code, we have to make sure, that the fission products are actually within the boundaries of the selected part of the nuclide chart. In case the fragment lies outside this boundary we replace it with the heaviest isotope of the fragment, which is within the boundary. The difference in mass is assumed to be overcome with emission of the same amount of neutrons. The sum of released neutrons from both fragments constitutes η_n. Depending on the choice of network as many as ~ 20 neutrons can be emitted in a single fission reaction.

Chapter 3

The Big Bang

The big bang theory, stating that our universe began roughly fifteen billion years ago in an extremely hot and dense state, is, at least among scientists, widely accepted today. The three key observational features supporting this theory are the expansion of the universe, the cosmic microwave background radiation (CMB) and big bang nucleosynthesis (BBN). In the early years of the twentieth century Edwin Hubble discovered that galaxies are receding from us in every direction. Projecting galaxy trajectories backwards in time shows that they converge in a single, dense location. As a direct consequence of the expansion Ralph Alpher and George Gamow formulated in 1948 a first theory on the origin of elements [7] also known as the Alpher-Bethe-Gamow theory ($\alpha\beta\gamma$-theory), indicating that as the universe expands and cools down from an initial state, where photons and matter were in thermal equilibrium, all free electrons and ions would recombine to form neutral atoms. Since photons only scatter infrequently from neutral atoms, photons decoupled from matter and the universe became transparent to radiation. Subsequently, the energy of the photons was redshifted by the expansion of the universe, conserving the power spectrum, but lowering the temperature from an initial value of $\sim 10^4$K down to ~ 3K. Only a few years later in the sixties Arno Penzias and Robert Wilson accidentally discovered a highly isotropic background radiation in the microwave region of the electromagnetic spectrum. The radiation appeared as perfect black body spectrum with Planckian power distribution at a temperature of 2.725 ± 0.001K, thus consolidating the big bang theory.

Big bang nucleosynthesis, the third pillar on which the big bang theory is based, is the topic of this chapter. The abundance evolution in BBN only follows a few nuclides and only depends on a relatively small number of key reactions. This makes it one of the most computationally simple in all of astrophysics and hence presents us with the opportunity to calculate abundances with a precision and accuracy which is unique.

In Section 3.1 we present the physical description of the expansion and the evolution of key quantities. The description is largely based on the explanations in chapter 5 of [29]. Section 3.2 is a qualitative discussion of primordial nucleosynthesis. Section 3.3 is the main part of this chapter where we present the results of our calculations (3.3.1), compare them to observations recently published results (3.3.2) and discuss the lithium problem (3.3.3). Furthermore, we present an alternative to the standard big bang model and discuss the implications for primordial nucleosynthesis (3.3.4).

3.1 Physics of the Expansion

The standard model of a *hot big bang* describes the adiabatic expansion of an isotropic and homogeneous universe without degenerate or exotic particles. The evolution of such an universe is described by the three Friedmann equations:

$$\ddot{R} = -\frac{4\pi}{3c^2}\left(\rho_\epsilon + 3P\right)GR + \frac{1}{3c^2}\Lambda R \tag{3.1}$$

$$\left(\frac{\dot{R}}{R}\right)^2 = H(t)^2 = \frac{8\pi G}{3c^2}\rho_\epsilon - \frac{kc^2}{R^2} + \frac{1}{3c^2}\Lambda \tag{3.2}$$

$$\frac{d\left(\rho_\epsilon R^3\right)}{dt} + P\frac{dR^3}{dt} = 0. \tag{3.3}$$

ρ_ϵ denotes the total relativistic energy density $\rho_\epsilon = u + \rho c^2$ and ρ the mass density. We can interpret Eq.(3.3) as the first law of thermodynamics $dQ = dU + PdV = 0$ for an adiabatic expansion of an ultra-relativistic gas where the chemical potentials of all particles vanish. In this very early and hot phase of an expanding universe the temperature is so high that the rest mass is negligible in comparison to the kinetic energies, thus $\rho_\epsilon = u$. In the relativistic limit $kT \gg mc^2$, which is the case for the whole early radiation-dominated phase, the equation of state (EoS) is given as

$$P = \frac{u}{3} = \frac{\rho_\epsilon}{3}. \tag{3.4}$$

After the quark-hadron phase transition (where quarks and gluons combined into nucleons) no free quarks and gluons exist anymore. At temperatures $k_BT > 1\text{MeV}$ the plasma is composed of neutrons, protons, electrons, positrons, photons and the electron-, muon- and tau-neutrinos and their antiparticles. Basically all particles with $2m < k_BT/c^2$ exist because the respective particle-antiparticle pairs can be created in photon collisions. Scattering reactions thermalize all plasma constituents to the same temperature and reactions like $\gamma + \gamma \rightleftharpoons e^+ + e^-$, $\nu_e + \nu_e \rightleftharpoons e^+ + e^-$, $p + e^- \rightleftharpoons \nu_e + n$ and $n + e^+ \rightleftharpoons \bar{\nu}_e + p$ are all in chemical equilibrium.

All of the aforementioned particles are highly relativistic, except for nucleons which are slower due to their large mass. At temperatures of about 1MeV, nucleons follow a Maxwell-Boltzmann distribution and their pressure contribution will be nk_BT. The linear temperature dependence is negligible compared to the T^4 dependence of the pressure of ultra-relativistic particles and thus the pressure contribution of nucleons is not important in a radiation dominated regime. The EoS Eq.(3.4) for the above mixture of particles calculates as

$$\begin{aligned} P &= \frac{\rho_\epsilon}{3} = \frac{1}{3}\frac{g}{2}aT^4 \\ g &= \sum_{bosons} g_i + \frac{7}{8}\sum_{fermions} g_i \end{aligned} \tag{3.5}$$

with $a = 8\pi^5 k_B^4/(15c^3h^3)$ and the relativistic degrees of freedom g. With this result we can derive a time-temperature relation as a measure for the expansion. Putting

Eq.(3.4) in Eq.(3.3) leads to $d\left(\rho_\epsilon R^4\right)/dt = R\times$Eq.(3.3) and therefore $\rho_\epsilon R^4$=const. In a flat universe with $k = 0$ and a vanishing cosmological constant $\Lambda = 0$, Eq.(3.2) yields $\dot{R} \propto R^{-1}$ with the solution $R(t) = \alpha t^{1/2}$ and $\dot{R}/R = 1/(2t)$. On the other hand we get from Eq.(3.5) $\rho_\epsilon = (g/2)\, aT^4$. Thus we can derive from Eq.(3.2) a relation between $1/t^2$ and T^4 as a function of g, with its precise form being

$$t = \left(\frac{3c^2}{16\pi Ga}\right)^{1/2} g^{-1/2}\frac{1}{T^2}. \tag{3.6}$$

As $g_\gamma = g_{e^-} = g_{e^+} = 2$ and $g_\nu = g_{\bar{\nu}} = 1$ (for all neutrino flavours), and since all particles except the photons are fermions we can calculate the total or *effective relativistic degrees of freedom* [124] and obtain

$$g = 2 + \frac{7}{8}(2+2+6) = \frac{43}{4}. \tag{3.7}$$

With this and Eq.(3.6) the temperature evolution is given by

$$T_9 \approx 10.15\frac{1}{t^{1/2}}. \tag{3.8}$$

Since all ultra-relativistic particles have $\bar{\mu}_i = 0$ the electron and positron captures on protons and neutrons lead to $\bar{\mu}_n = \bar{\mu}_p$. Using the Maxwell Boltzmann expression for the chemical potentials, Eq.(2.53), results in

$$\frac{n_n}{n_p} = \frac{X_n}{X_p} = \exp\left(-\frac{\Delta mc^2}{k_B T}\right), \tag{3.9}$$

where Δm is the mass difference between proton and neutron.

As the universe expands and cools to reach $k_B T \approx 1$ MeV (at $T \approx 10^{10} K$ or slightly lower due to the high energy tails of the thermal distributions), electrons are not energetic enough anymore to overcome the mass difference between protons and neutrons via electron capture. Also, photons are not energetic enough anymore to produce positrons in pair-production processes to support positron capture on neutrons. Therefore, these weak reactions will cease to exist. These reactions are also the channel through which neutrinos communicate thermally with the other constituents. We call this phase *weak freeze-out* and *weak decoupling* because the neutrinos are from this time forward decoupled and can have different temperatures from the other particles. Also the neutron to proton ratio is frozen out at $\exp\left(-\Delta mc^2/k_B T_{weak}\right)$. For $k_B T_{weak} \simeq 0.8$MeV [37] this results in $n/p \simeq 1/6$ and from this point on this ratio can only change via beta-decay of the neutron.

The entropy of ultra-relativistic particles is given by

$$S = \frac{4}{3}\frac{g}{2}aT^3 V, \tag{3.10}$$

with the same definition of g as in Eq.(3.5). After weak decoupling, positrons do not exist anymore and the electrons are no longer ultra-relativistic and therefore have a negligible pressure (and entropy) contribution. Hence, only photon and neutrino contributions have to be considered. The annihilation of electrons and positrons

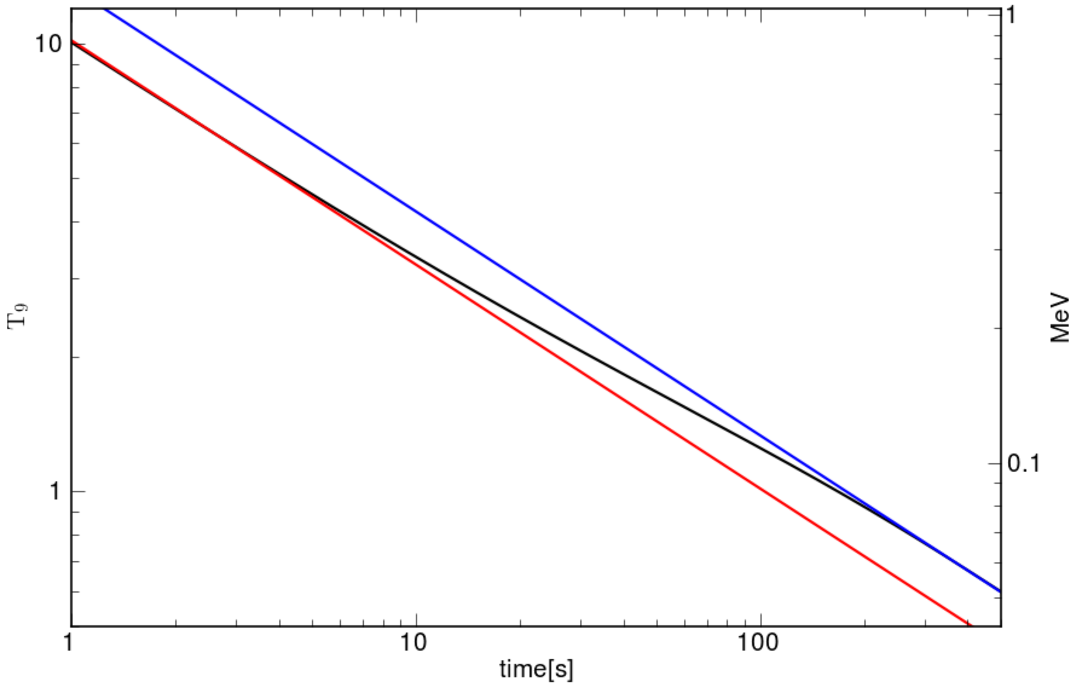

Figure 3.1: Temperature evolution during weak freeze-out. The red and blue line denote the analytic solution before and after weak freeze-out respectively (see text).

produced energetic photons, thus heating up the photon gas. Meanwhile, the neutrinos expand without interaction, based on the original temperature. Since the expansion is adiabatic, the entropy in an expanding volume has to stay constant through the phase of weak decoupling. Therefore, ignoring the common factor 4/3

$$\frac{43}{8}aT^3V = aT_\gamma^3V + \frac{7}{8}\cdot\frac{6}{2}aT^3V \tag{3.11}$$

$$\Rightarrow \frac{T_\gamma}{T} = \left(\frac{11}{4}\right)^{1/3}, \tag{3.12}$$

where T_γ is the photon temperature. Additionally, we can calculate the relativistic degrees of freedom by expressing the right hand side of Eq.(3.5) as function of T_γ, leading to

$$g = 2 + \frac{7}{8}\cdot 6\left(\frac{4}{11}\right)^{4/3} \approx 3.3626. \tag{3.13}$$

During weak decoupling the overall g changes from $43/4 = 10.75$ to 3.3626 when we express the Pressure in terms of the photon temperature. Due to thermalization this is also the nucleon temperature which, at a later phase, will determine nuclear reactions. Furthermore, the temperature evolution changes after weak decoupling, Eq.(3.6) now yields

$$T_9 \approx 13.336\frac{1}{t^{1/2}}. \tag{3.14}$$

In Figure 3.1 we plotted the time evolution (black line) of the temperature as it is calculated from the self-consistent prescription (see Appendix A) as well as Eq.(3.8) (red line) and Eq.(3.14) (blue line). One can clearly see that the weak freeze-out is not a sharp transition but a gradual process which occurs in the region $5 \gtrsim T_9 \gtrsim 1$.

Another quantity we want to discuss is the ratio of baryon density to photon density $\eta = n_b/n_\gamma$. The photon density, like that of all ultra-relativistic particles, only depends on the temperature

$$n_\gamma = \frac{2.404}{\pi^2}\left(\frac{k_B T}{\hbar c}\right)^3 . \tag{3.15}$$

The baryon (or nucleon) density, however, depends on temperature and density. Thus the global $\eta \propto \rho/T^3$ provides a relation between temperature and density. Once such a relation is known, Eqs.(3.2) and (3.3) provide a unique solution of the expanding early universe. From Eq.(3.10) we can also infer $\eta \propto 1/S$ and thus that η has to remain constant in an adiabatic expansion. In our computations the evolution of (photon) temperature and density does not depend on η but we need *eta* to determine the initial density as a function of temperature. Therefore we have to make sure that η has the right T_γ dependence. Since the photon temperature changes during weak decoupling, Eq.(3.12), and thus also η changes like $1/T_\gamma^3$. Hence

$$\eta = \frac{11}{4}\eta_0, \tag{3.16}$$

where η_0 denotes the value after weak decoupling, which has remained constant until today [135]. With a global baryon to photon ratio we can now express the baryon density as a function of temperature

$$n_b = \eta n_\gamma = \frac{2.404\eta}{\pi^2}\left(\frac{k_B T}{\hbar c}\right)^3 . \tag{3.17}$$

With all of the above relations we now have a complete theoretical description of the expansion which only depends on one single parameter, η. The time evolution of temperature and density has to be calculated self-consistently without introducing more free parameters. Our prescription for the self-consistent calculation closely follows the explanations in Appendix D of [65]. A detailed description of the physics and the implementation is provided in Appendix A.

3.2 Building the Elements

After weak decoupling, the plasma is still very hot and consists of photons, electrons, neutrons and protons. The nucleons collide among themselves to produce deuterons ($D = {}^2\mathrm{H}$) via $n+p \rightleftharpoons D+\gamma$. However, the density and average energy of the background photons is very high and the deuterons are almost instantly photodisintegrated. We can estimate the temperature at which deuterium starts to be produced in reasonable amounts by comparing the production rates Γ_p and the destruction rates Γ_d (from detailed balance) [37]

$$\begin{aligned} \Gamma_p &\approx n_B \langle\sigma v\rangle \\ \Gamma_d &\approx n_\gamma \langle\sigma v\rangle e^{-B_D/k_B T}. \end{aligned} \tag{3.18}$$

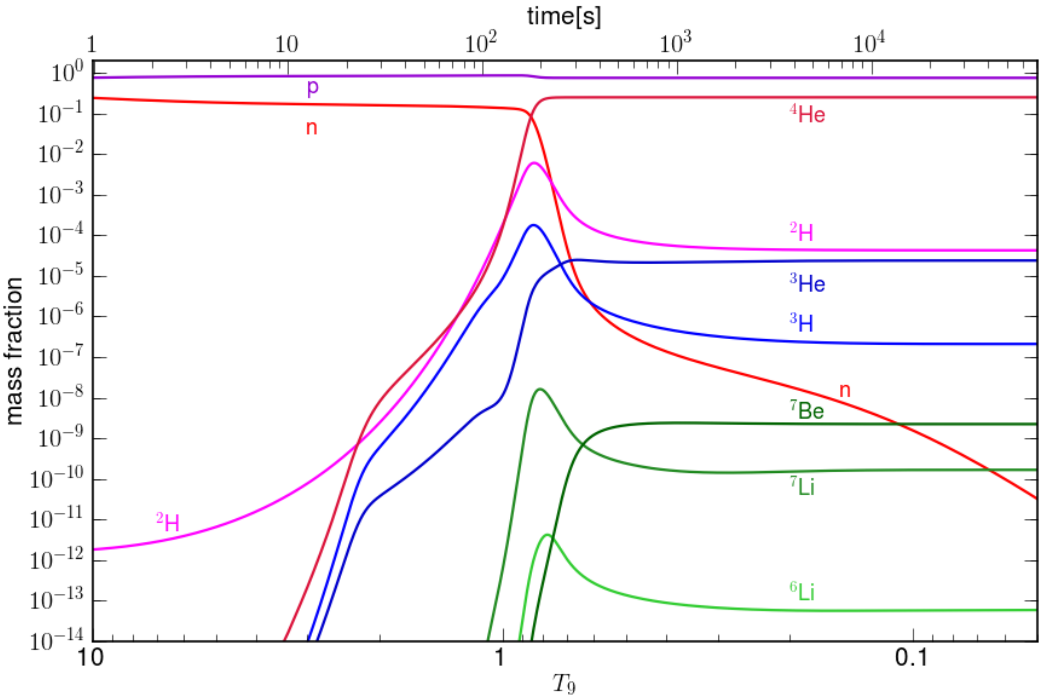

Figure 3.2: An example of the time and temperature evolution of light element mass fractions computed with our self-consistent network evolution code and a baryon to photon ratio of $\eta = 6.1 \times 10^{-10}$. The main part of nucleosynthesis takes place around $T_9 = 1$ as soon as deuterium is produced in significant amounts. The synthesis of elements is completed after about 25 minutes except for the decay of neutrons, ^{3}H and ^{7}Be.

As soon as $\eta \exp\left(B_D/k_B T\right) \sim 1$ the destruction rate falls below the production rate and the nuclear reaction chain sets in. With the binding energy of the deuteron $B_D = 2.23$MeV and $10^{-11} \leq \eta \leq 10^{-7}$ this happens at $k_B T \simeq 0.1$MeV (or $T_9 \simeq 1$). Once the deuterium bottleneck is overcome, neutrons and protons quickly combine to form D, ^{3}H, ^{3}He and ^{4}He. The fact that there is no stable nuclide with mass A=5 prevents this chain from going further via neutron and proton captures. This bottleneck is resolved by ^{3}H and ^{3}He captures on ^{4}He. The Coulomb repulsion between these colliding nuclei reduces the reaction rates ensuring that virtually all neutrons are incorporated into the most stable of the light nuclides, ^{4}He and that the abundances of heavier nuclides are dramatically lower than that of ^{4}He. The primordial mass fraction of ^{4}He can be estimated by $X_\alpha = 4Y_\alpha = 2X_n$ with $X_n = X_n/\left(X_n + X_p\right)$. By the time nucleosynthesis starts (at around 130s), the n/p-ratio has dropped from 1/6 at weak freeze-out to $\sim 1/7$ because of neutron decays. It follows, that

$$X_\alpha \approx \frac{2X_n/X_p}{1 + (X_n/X_p)} = 0.25. \tag{3.19}$$

The few reactions which manage to jump the A=5 mass gap mainly lead to mass-7 nuclides (^{7}Li and ^{7}Be, which will later decay to ^{7}Li). The abundance of ^{6}Li is below that of the more tightly bound ^{7}Li by one or two orders of magnitude. Another mass gap at A=8 inhibits $^4\text{He} + {}^4\text{He}$ reactions and prevents any astrophysically interesting

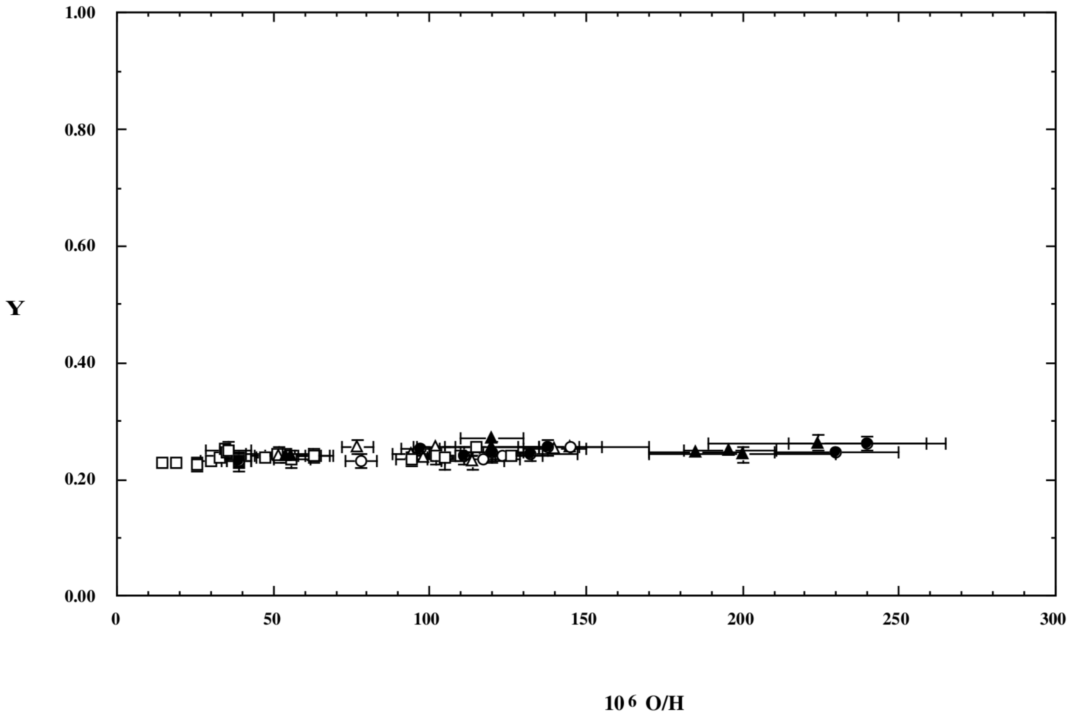

Figure 3.3: The ^{4}He mass fraction, Y, inferred from observations of low-metallicity, extragalactic H_{II} regions versus the oxygen abundance in these regions (figure adopted from [124]).

production of heavier nuclides.

Because of decreasing temperatures and the presence of Coulomb barriers, nuclear reactions cease as soon as the temperature drops below $\sim$ 30keV, when the universe is about 25 minutes old. As a result, there is a "nuclear freeze-out" since no already existing nuclides are destroyed (except for those that are unstable and decay) and no new nuclides are created [124].

At one point in history, big bang nucleosynthesis as a theory to explain the observed element abundances was nearly abandoned, because it fails to explain *all* element abundances. In their seminal paper Burbidge, Burbidge, Fowler and Hoyle [20] crowned stellar nucleosynthesis as leading theory for element production. However, two key demands could not be met. 1) The abundance of ^{4}He as a function of metallicity is nearly flat. In Figure 3.3 is shown a compilation of observational data [93, 94, 60, 59], the figure is taken from [124]. The key feature of Figure 3.3 is that even in systems in which an element as oxygen, which traces stellar activity, is observed at extremely low values (compared with the solar value of $O/H = 5 \times 10^{-4}$ [105]), the ^{4}He abundance is nearly constant. This is very different from the abundances of elements which are produced in stellar nucleosynthesis where the abundance goes to zero as O/H goes to zero. 2) The observed abundance of deuterium cannot come from stellar sources. In fact stars actually destroy deuterium and there is no astrophysical site known for the production of significant amounts of deuterium other than the big bang[35].

Having sketched the basic physics of big bang nucleosynthesis, we now turn to the detailed description of how to model the big bang to get predictions for all relevant elements.

3.3 Nucleosynthesis

The strength of the standard big bang scenario is, as we have pointed out before, that all primordial abundances, ranging over several orders of magnitude, are determined by only one free parameter, the baryon-to-photon ratio $\eta = n_b/n_\gamma$. This cosmological parameter is related to Ω_B, the present-Universe ratio of the baryon mass density to the critical mass–energy density [126]

$$\eta_{10} = 10^{10}\frac{n_B}{n_\gamma} = 273.9\Omega_B h^2, \tag{3.20}$$

where h is the present value of the Hubble parameter in units of 100 km s^{-1} Mpc^{-1}. Basically there are two complementary approaches to testing standard big bang nucleosynthesis (SBBN):

1. Primordial abundances inferred from observations should be consistent with the SBBN predictions for a *unique value* or a *range of values* of η. Since the baryon-to-photon ratio can not yet be determined from basic principles, it can be obtained from a best fit of observed to calculated abundances. In Figure 3.4 we show the abundances of ^{4}He (mass fraction), ^{2}H, ^{3}He and ^{7}Li (by number relative to H) as a function of η, as well as primordial abundances deduced from observations. It is obvious that there is no single value of η, for which all abundance predictions fit observations. Still it is an impressive confirmation of the standard cosmological model that the baryon densities inferred from abundances, which range over some nine orders of magnitude, lie within a factor of three of each other. We will discuss the observational constraints on each element in detail in the next section.

2. If there is a non-BBN constraint on η we can make definitive predictions for light element abundances which can then be compared to observations. The *Wilkinson microwave anisotropy probe* (WMAP), measuring the cosmic microwave background radiation with very high precision, provides such a constraint. The seven year WMAP data [67] gives $\Omega_B h^2 = 0.02249 \pm 0.00056$, corresponding to $\eta = 6.16 \pm 0.15 \times 10^{-10}$. The vertical line in Figure 3.4 labelled *WMAP7* marks this value. The resulting differences between calculation and observation can be due to inaccurate data and/or unidentified systematics in the observations, incorrect models for analysing the data and/or extrapolating from abundances determined at present to primordial values or the fact that the standard models of particle physics and cosmology are incomplete and need to be revised. They also shed new light on the nucleosynthesis after the big bang.

Having a closer look at Figure 3.4 we note that the light elements show quite different dependencies on η. The primordial abundance of ^{4}He is relatively insensitive to the baryon density (note the linear scale compared to the logarithmic scale for the other elements). Since virtually all neutrons available in BBN are incorporated in ^{4}He, it does depend on the competition between the weak interaction rate (largely fixed by the neutron lifetime) and the expansion rate of the universe (which depends on g_{eff}). This makes ^{4}He a *cosmological chronometer* [125]. The higher the nucleon density, the earlier the deuterium-bottleneck can be breached. At earlier times there are more neutrons (since they had less time to decay) and therefore more ^{4}He will be synthesized.

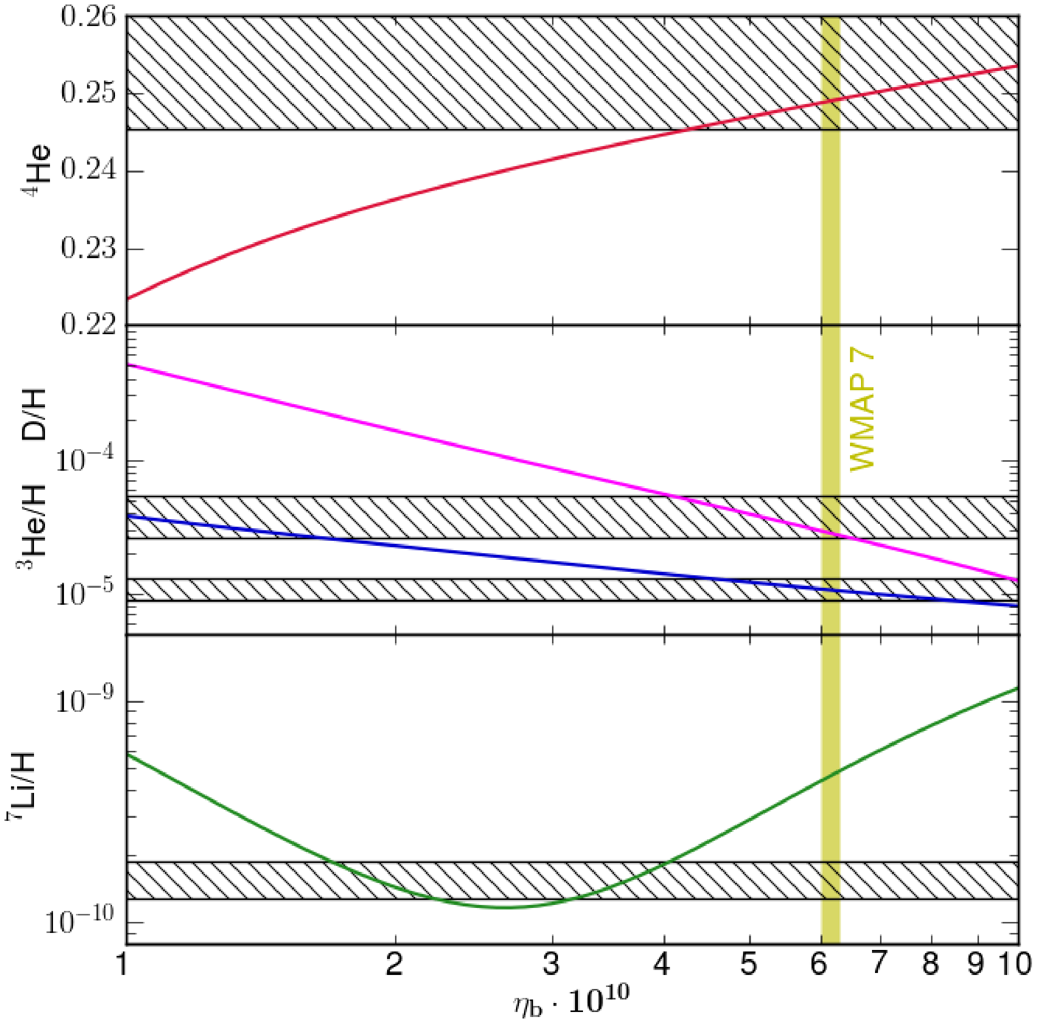

Figure 3.4: Abundances of ^{4}He (mass fraction), ^{2}H, ^{3}He and ^{7}Li (by number relative to H) as a function of the baryon over photon ratio η (or $\Omega_b h^2$). The hatched bands represent the primordial abundances deduced from observations (see text). The vertical stripe is the WMAP7 value $\eta = 6.16 \pm 0.15 \times 10^{-10}$[67].

The latter effect is responsible for the very slow (logarithmic) increase in ^{4}He with η. Similarly, the faster the universe expands, the less time there is for the neutrons to decay, resulting in more neutrons and thus more ^{4}He. In contrast to ^{4}He, the abundances of the other light elements (^{2}H, ^{3}He and ^{7}Li) are rate limited and depend strongly on the baryon density. Thus ^{2}H, ^{3}He and ^{7}Li are potential *baryometers*. The trends in the abundances of ^{2}H and ^{3}He can be understood as follows: ^{2}H and ^{3}He are burned to ^{4}He. The higher the baryon density, the faster this occurs, leaving behind less ^{2}H and ^{3}He. At lower baryon densities the burning is slower, resulting in a less complete burning and therefore more ^{2}H and ^{3}He. The behaviour of ^{7}Li is more complicated. At relatively low values of $\eta \lesssim 3$, ^{7}Li is mainly synthesized directly as ^{7}Li (Figure 3.5), via $^3\mathrm{H}(\alpha,\gamma)\,^7\mathrm{Li}$ reactions, which is easily destroyed in collisions with protons ($^7\mathrm{Li}(p,\alpha)^4\mathrm{He}$). Hence, as η increases at low values, ^{7}Li/H decreases until it

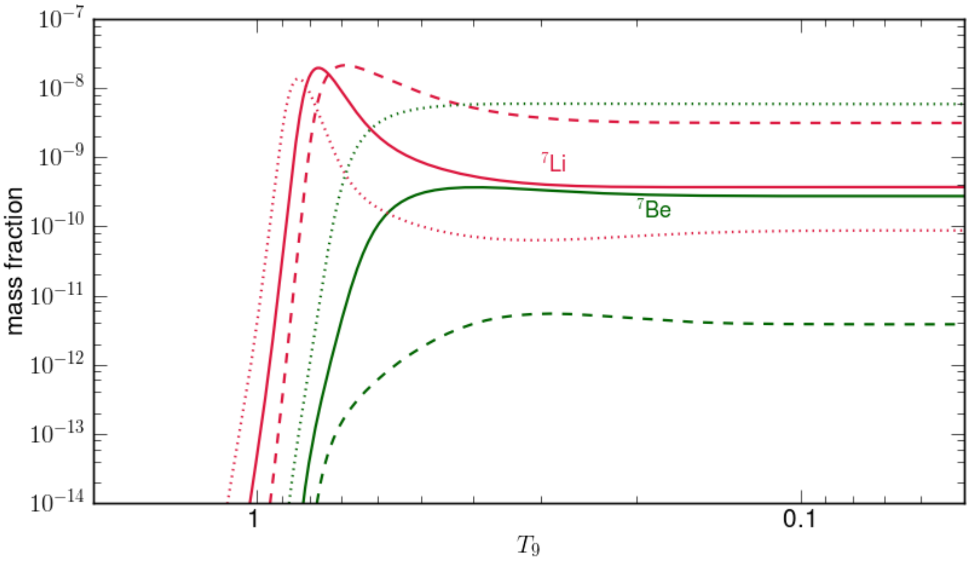

Figure 3.5: Evolution of mass fractions for ^{7}Li (red) and ^{7}Be (dark green) for different values of η. The dashed, solid and dotted lines represent low ($\eta = 10^{-10}$), intermediate ($\eta = 3 \times 10^{-10}$) and high ($\eta = 10^{-9}$) values of the baryon-to-photon ratio. For low baryon densities the synthesis of ^{7}Li dominates the final ^{7}Li mass fraction, for intermediate values of η, which represent the minimum of the ^{7}Li curve in Figure 3.4, the contribution to the final mass fraction is about equal and for high baryon densities the main contribution comes from the synthesis of ^{7}Be, which later decays to ^{7}Li.

reaches a minimum at $\eta \sim 3$ (Figure 3.4). At higher values of $\eta \gtrsim 3$, ^{7}Li is mainly synthesized as ^{7}Be (Figure 3.5), via $^3\mathrm{He}\,(\alpha,\gamma)\,^7\mathrm{Be}$ reactions, which is more tightly bound and therefore harder to destroy. As η increases at high values, the abundance of ^{7}Be increases and with it the late-time abundance of ^{7}Li (Figure 3.4)[124].

3.3.1 SBBN Predictions

SBBN calculations are performed with the nuclear reaction network introduced in chapter 2 and the self-consistent evolution of temperature and density presented in appendix A. The network itself consists of 26 nuclides, ranging from free neutrons and protons to ^{16}O. In table 3.1 we list all nuclides in the network. The thermonuclear reaction rates are taken from the latest compilation of the JINA reaclib database [30]. The weak reactions transforming $n \rightleftharpoons p$, which determine the n/p-ratio at the onset of BBN and thus the ^{4}He abundance, are taken from [117]. The authors present a numerical fit to the improved Born rates, considering electromagnetic radiative corrections, finite nucleon mass corrections, thermal/radiative effects and non instantaneous neutrino decoupling effects. The accuracy of the fit is claimed to be better than 0.06% and satisfies the detailed balance condition

$$\frac{\lambda_{n\to p} n_n}{\lambda_{p\to n} n_p} = 1 \tag{3.21}$$

better than the 1% level for $k_BT > m_ec^2$.The fit is given as a function of $z = m_ec^2/k_BT$ and the neutron lifetime τ_n

$$\lambda_{n\to p} = \frac{1}{\tau_n}\exp\left(-q_{np}/z\right)\sum_{l=0}^{13} a_l z^{-l} \qquad 0.01 \leq k_BT \leq 10 \tag{3.22}$$

$$\lambda_{p\to n} = \begin{cases} \frac{1}{\tau_n}\exp\left(-q_{pn}z\right)\sum_{l=0}^{10} b_l z^{-l} & 0.1 \leq k_BT \leq 10 \\ 0 & 0.01 \leq k_BT < 0.1 \end{cases} \tag{3.23}$$

The fit coefficients are listed in appendix B.1. We also made use of the current value for the neutron lifetime $\tau_n = 881.5 \pm 1.5$s [87].

In order to ensure full equilibrium, even for neutrinos, all calculations were started at $T_9 = 100$. At temperatures this high we can safely assume that baryonic matter consists only of neutrons and protons and their initial abundances can be calculated from Eq.(3.9) and mass conservation Eq.(2.48), hence

$$Y_n = \frac{1}{1+\exp\left(\Delta mc^2/k_BT\right)} \tag{3.24}$$

$$Y_p = \frac{1}{1+\exp\left(-\Delta mc^2/k_BT\right)}. \tag{3.25}$$

The baryon-to-photon ratio was either set as a free parameter to check the dependence of light element abundances on the baryon density (Figure 3.4), or to the seven year WMAP value $\eta = 6.16 \pm 0.15 \times 10^{-10}$ to make abundance predictions which will later be compared to observations and other SBBN calculations. The SBBN predicted abundances resulting from our calculations are

$$\begin{aligned} \mathrm{D/H} &= (2.84 \pm 0.23) \times 10^{-5} \\ {}^3\mathrm{He/H} &= (1.07 \pm 0.09) \times 10^{-5} \\ \mathrm{Y_p} &= 0.2490 \pm 0.0005 \\ {}^7\mathrm{Li/H} &= (4.57 \pm 0.55) \times 10^{-10}. \end{aligned}$$

We use Y_p to denote the primordial ^{4}He mass fraction following the astronomical notation where X, Y and Z represent the mass fractions of H, ^{4}He and metals. The given uncertainties are adopted from [124] where they give theoretical uncertainties at the ~ 8% level for D/H and ^{3}He/H, ~ 12% for ^{7}Li/H and ~ 0.2% for ^{4}He. In the following sections we will discuss the observational status of these elements individually and compare our results with observations and different calculations found in the literature.

3.3.2 Testing the Consistency of SBBN

The SBBN predicts abundances which are essentially determined at the end of nucleosynthesis, when the universe is ~20 minutes old. Observations, however,are made at a much later time, after stellar nucleosynthesis has started. The ejected matter which has been processed in stars can alter the primordial abundances of light elements but also produce heavier elements such as C, N, O and Fe, which are astronomically all *metals*.

Nuclide	A	Nuclide	A
n	1	B	8, 10, 11, 12
H	1, 2, 3	C	11, 12, 13, 14
He	3, 4	N	12, 13, 14, 15
Li	6, 7, 8	O	14, 15, 16
Be	7, 9		

Table 3.1: The 26 nuclides considered in BBN calculations.

In order to minimize the polluting effects of stellar activity, one seeks astrophysical sites with low metal abundances to measure light element abundances, which are close to their primordial value. We will briefly discuss possible sites where one expects to measure primordial D, ^{3}He and ^{4}He and the difficulties in observing them. A much more thorough discussion can be found in [124].

3.3.2.1 Deuterium

It is a widely accepted fact that there is no astrophysical process other than the big bang where D is produced in interesting amounts [35]. The predicted primordial abundance is sensitive to baryon density (D/H $\propto \eta^{-1.6}$)[124]. Furthermore, the loosely bound deuterium is only destroyed and not produced, as gas is cycled through stars. Thus all observations can provide at least a lower limit for the primordial value. All of the above make deuterium the baryometer of choice.

Whereas there are plenty of measurements of D abundances in our solar system and the local interstellar medium, there is only a handful of observations at high redshift and low metallicity where conventional models of galactic chemical evolution do not predict significant D/H depletion. The most promising candidates are so called quasar absorption-line systems (QSOALS) where clouds at high redshift are in the line of sight of distant quasars, thus producing absorption lines in the quasar spectra. The identification of the deuterium lines in the spectra are far from trivial, since there are identical lines in D_I and H_I except for a wavelength/velocity shift.

The most recent analysis of available data [102] lists seven objects where the deuterium abundance is clearly resolved from nearby spectral features. The author of [125] calls it very nearly a sin to claim that the primordial abundance of a cosmologically key light nuclide is determined by five (now seven) data points. Additionally, the data points do not agree within statistical errors but show a wide dispersion with a χ^2 about the mean $\gtrsim 16$, suggesting either that the uncertainties have been underestimated or that some of the data may be contaminated by unidentified systematic errors.

In Figure 3.6 D/H is plotted as function of η. To check the consistency with observations, we plotted the primordial estimates from recent publications. An analysis of six QSOALS [95] yields

$$\mathrm{D/H} = \left(2.82^{+0.27}_{-0.25}\right) \times 10^{-5}, \tag{3.26}$$

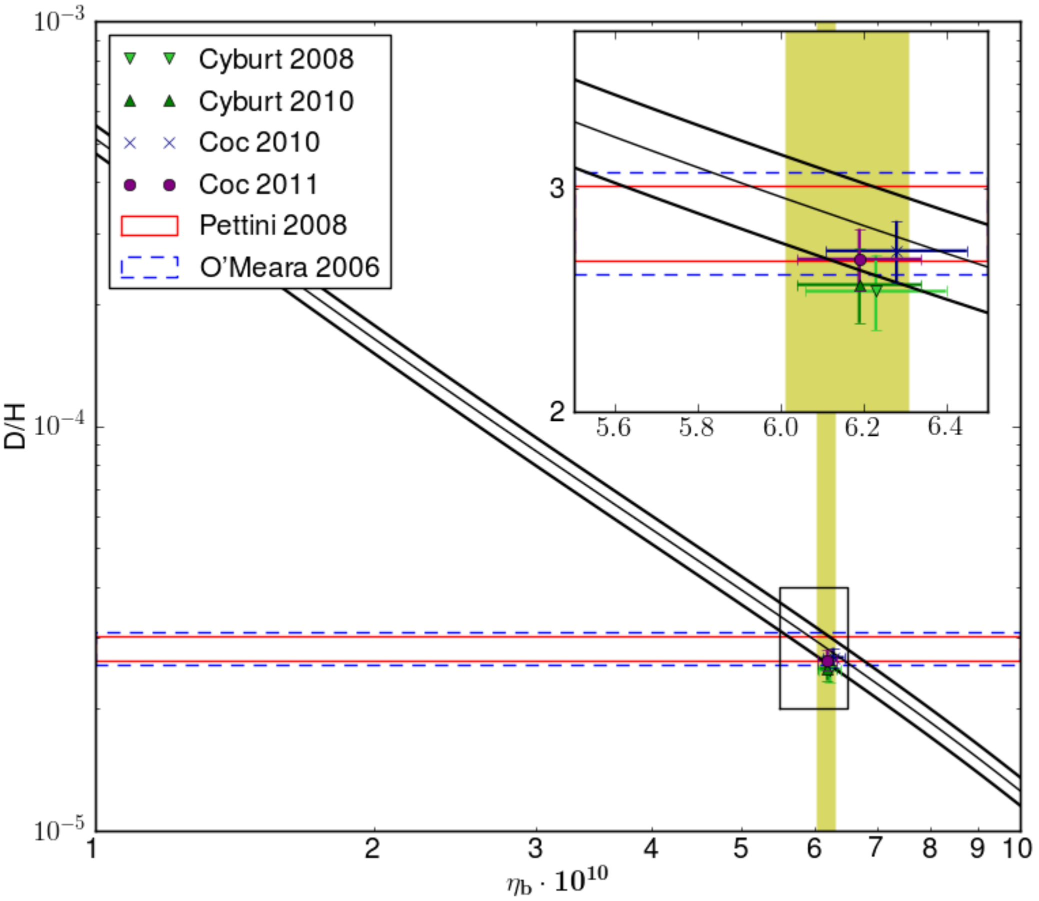

Figure 3.6: The diagonal band is the SBBN-predicted deuterium abundance (relative to hydrogen) as a function of the baryon-to-photon ratio (the width of the band accounts for the theoretical uncertainties). The horizontal bands are the adopted primordial ranges from two recent observational analyses [95, 102]. The datapoints with errorbars are from recent SBBN calculations [24, 26, 31, 32].

a more recent analysis, where an additional data point was available [102], gives

$$\mathrm{D/H} = \left(2.82^{+0.20}_{-0.19}\right) \times 10^{-5}. \tag{3.27}$$

Our predicted value of $\mathrm{D/H} = (2.84 \pm 0.23) \times 10^{-5}$ shows a very nice agreement with these observations for the WMAP7 value of η. For comparison we also plotted recent SBBN predictions from recent calculations. In [26] a value of $\mathrm{D/H} = (2.68 \pm 0.15) \times 10^{-5}$(navy cross) is calculated using updated nuclear data and an older value of $\eta = (6.28 \pm 0.17) \times 10^{-10}$. A more recent work of the same authors [24] with even newer reaction rates and the current WMAP7 value for the baryon density yields $\mathrm{D/H} = 2.64 \times 10^{-5}$ (purple circle). From the people providing the reaction rates we utilized, comes another prediction [31] of $\mathrm{D/H} = (2.52 \pm 0.17) \times 10^{-5}$ (green triangles). We also added an older result from the same authors [32] where they used an older value $\eta = 6.23 \pm 0.17$ to yield $\mathrm{D/H} = (2.49 \pm 0.17) \times 10^{-5}$ (lime green triangles) The theoretical predictions are all lower than our predicted value and close to the lower limit

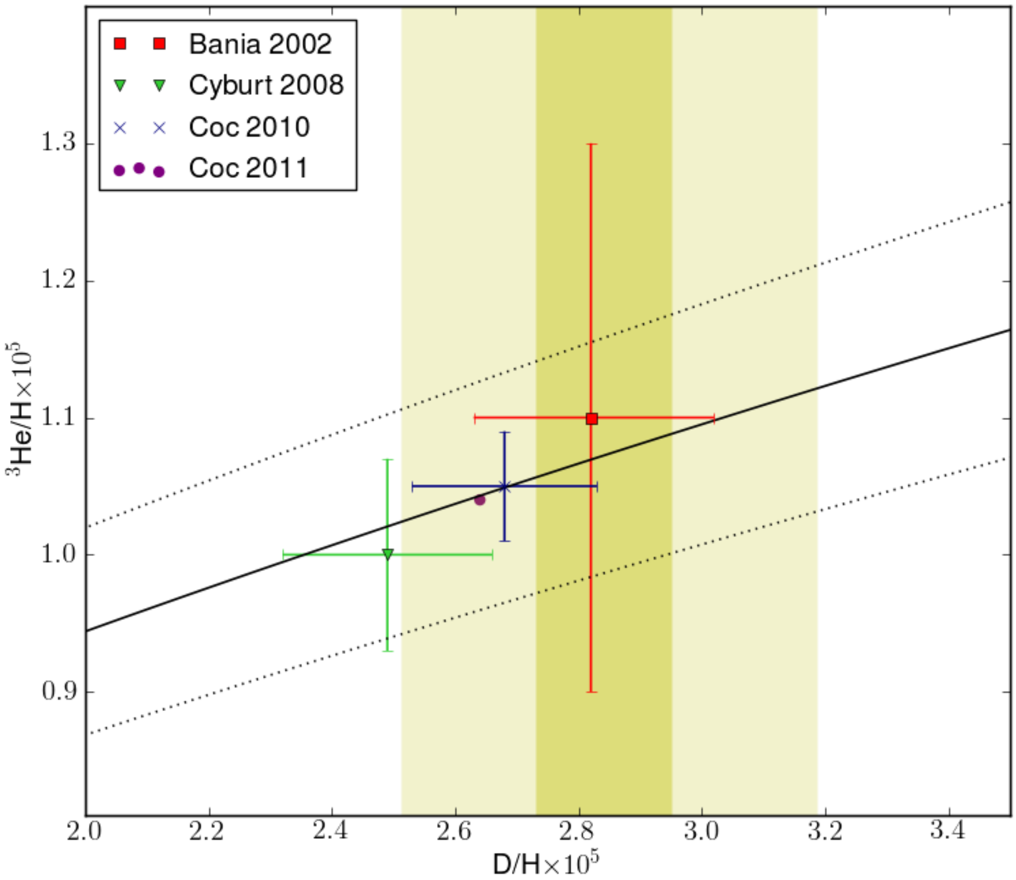

Figure 3.7: The solid line is the SBBN-predicted ^{3}He abundance (relative to hydrogen) as a function of the deuterium abundance (relative to hydrogen). The dotted lines account for the theoretical uncertainties. The vertical bands are the values of D/H consistent with the WMAP7 value of the baryon density (the dark yellow region corresponds to the variation of the mean value with η, the light yellow region includes the theoretical error $\sim$ 8%). The red square with errorbars represents observations of ^{3}He in the milky way [17]. The other datapoints are from recent SBBN calculations [26, 24, 32].

of observational constraints, but the overall agreement is good and within statistical errors. The predicted values of the other light elements will be tested against the D/H abundance to check overall consistency.

3.3.2.2 ^{3}He

The post-BBN evolution of ^{3}He is much more complicated than that of D. D that is incorporated into stars is rapidly burned to ^{3}He, increasing the ^{3}He abundance. Compared to D, ^{3}He is much more tightly bound and has a higher coulomb barrier. Therefore it is more resistant to nuclear burning. Nevertheless, ^{3}He is burned in the hot interiors of most stars to ^{4}He and beyond. In the cooler regions (for most stars these are only the outer layers, for lower mass stars it is most of the volume), however, ^{3}He is not processed. Since in all stars D is burned to increase ^{3}He, but not all of this newly synthesized ^{3}He is further processed, one would expect an increase of ^{3}He with time (and metallicity).

Unfortunately, observations of ^{3}He are limited to the solar system and our galaxy. But since there is a clear gradient of metallicity in the milky way, one would also expect a gradient in ^{3}He abundance. But no such trend is visible in the data [17], which shows no gradient within the galaxy. Whatever the explanation, there seems to be a delicate balance between production and destruction in stellar interiors. The model-dependent uncertainties in extrapolating from present data to primordial values are large, thus limiting the value of ^{3}He as a baryometer. We will still use the recommended value from [17]

$$^3\mathrm{He}/\mathrm{H} = (1.1 \pm 0.2) \times 10^{-5} \tag{3.28}$$

to check consistency between D and ^{3}He. Figure 3.7 shows the ^{3}He/H abundance as a function of D/H. The yellow shaded region represents the D/H values corresponding to the WMAP7 value of η. Our SBBN predicted value lies very well within the error bars of the observed ^{3}He thus showing excellent consistency between the mean values of D and ^{3}He. We also plotted the SBBN predicted values of recent calculations together with their respective D/H abundance, $^3\mathrm{He}/\mathrm{H} = (1.00 \pm 0.07) \times 10^{-5}$ [32] (lime green triangle), $^3\mathrm{He}/\mathrm{H} = (1.05 \pm 0.04) \times 10^{-5}$ [26] (blue cross) and $^3\mathrm{He}/\mathrm{H} = 1.04 \times 10^{-5}$ [24] (purple dot). Also the theoretical predicted values are in good agreement within theoretical errors, indicating a good consistency between D and ^{3}He.

3.3.2.3 ^{4}He

^{4}He is the second most abundant nuclide in the universe after hydrogen. As gas is processed in stars, hydrogen is burned to helium, thus increasing the ^{4}He abundance over generations of stars. At very low metallicity (looking back to a time when the contribution from stellar nucleosynthesis was very small) one expects the ^{4}He abundance to stagnate at its primordial value thus forming a plateau. The most relevant data for inferring this plateau value is from observations of helium and hydrogen recombination lines in low-metallicity, extragalactic clouds of ionized hydrogen ($\mathrm{H_{II}}$ regions). Unlike observations of primordial deuterium, observations of primordial helium are numerous (~ 100), leading to a small statistical uncertainty. The data also shows the expected plateau at low metallicity (Figure 3.3).

Unfortunately, abundance determinations do not only depend on the strength of helium emission lines, but also on a number of physical parameters associated with the $\mathrm{H_{II}}$ region. These include temperature, electron density, optical depth and the degree of underlying absorption [37]. Accounting for all these effects is a very difficult task resulting in large systematic errors and different results depending on the method of analysis. We will not go further into detail but refer to [101] and references therein for a review on the determination of the primordial helium abundance.

To check the consistency of our Y_p prediction we compare it to the adopted values of recent evaluations (Figure 3.8). Using new atomic physics computations of the recombination coefficients of $\mathrm{He_I}$ and of the collisional excitation of the $\mathrm{H_I}$ Balmer lines, the authors of [100] determine

$$Y_p = 0.2477 \pm 0.0029 \tag{3.29}$$

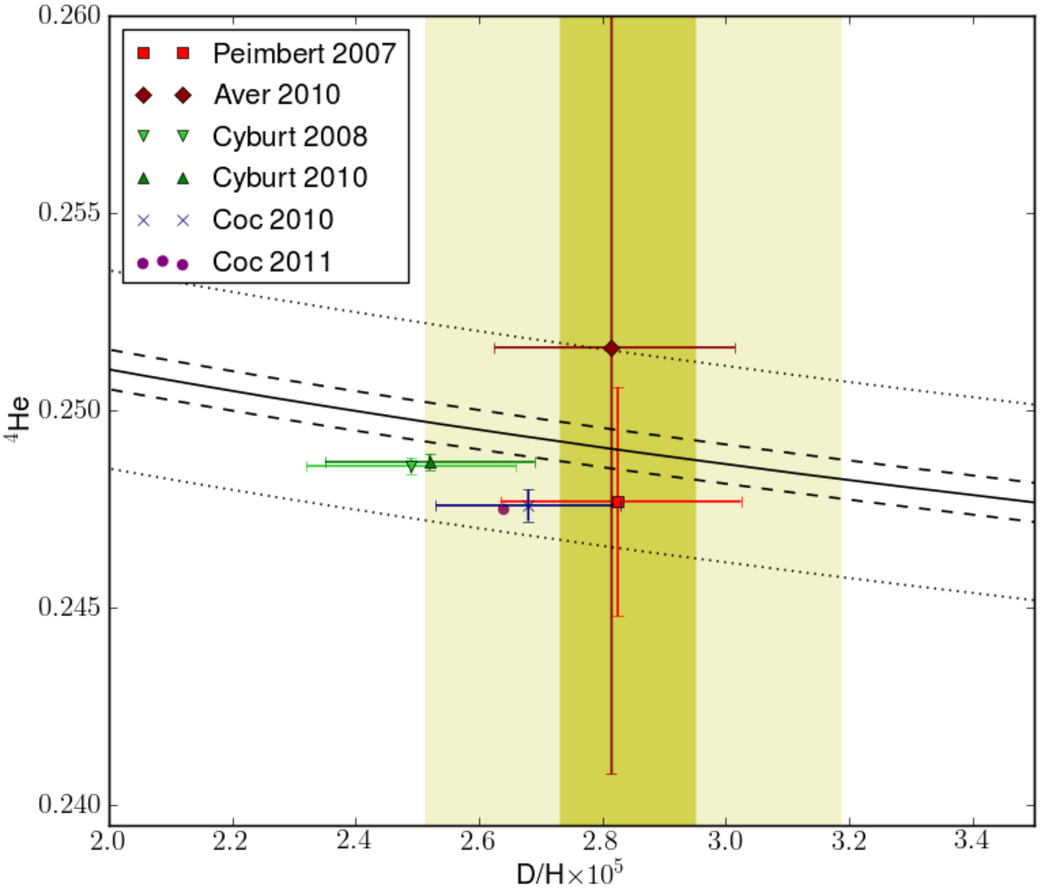

Figure 3.8: The solid line is the SBBN-predicted ^{4}He mass fraction as a function of the deuterium abundance (relative to hydrogen). The dashed lines account for the theoretical uncertainties (0.2%), the dotted lines illustrate an error of 1%. The vertical bands are the values of D/H consistent with the WMAP7 value of the baryon density (the dark yellow region corresponds to the variation of the mean value with η, the light yellow region includes the theoretical error $\sim 8\%$). The red square and dark red diamond with errorbars represent recent analysis of ^{4}He observations by [100] and [16] respectively. The points are slightly shifted in D/H for better readability. The other datapoints are from recent SBBN calculations [24, 26, 31, 32].

as best fit for the primordial helium. A different evaluation with a new approach to systematic uncertainties and self-consistency in helium abundance determinations, [16], leads to

$$Y_p = 0.2561 \pm 0.0108, \tag{3.30}$$

which is, aside from the larger errorbars, identical to the result of [61]. Our predicted value for the WMAP7 value of η is certainly consistent with both determinations from observation. But the large errorbars prevent ^{4}He from being a sensitive probe of the primordial baryon density. Again we also compare our result to recent calculations that give $Y_p = 0.2486 \pm 0.0002$ [32], $Y_p = 0.2487 \pm 0.0002$ [31], $Y_p = 0.2476 \pm 0.0004$ [26] and $Y_p = 0.2475$ [24]. All these theoretical predictions are lower than our predicted value, outside the estimated theoretical error, indicating a systematic difference. The

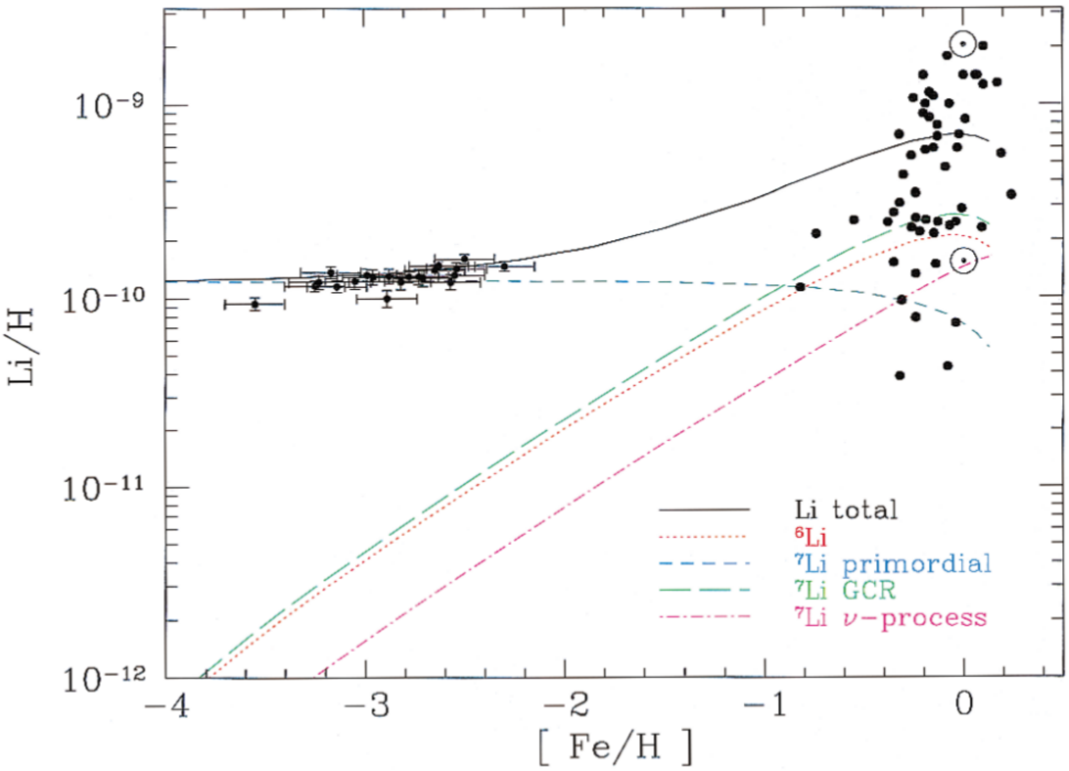

Figure 3.9: Contributions to the total predicted lithium abundance from the galactic chemical evolution model of [38] with $^7\text{Li/H} = (1.23 \pm 0.06) \times 10^{-10}$, compared with low-metallicity stars and high-metallicity stars. The solid curve is the sum of all components (figure adopted from [112]).

most likely source for this difference is the $n \leftrightarrow p$ conversion rate which determines the n/p ratio at weak decoupling and thus Y_p. Unfortunately none of the authors provide the actual rates they used and we can not definitely find the reason for the higher Y_p.

3.3.3 The Lithium Problem

So far the consistency of our abundance predictions for D, ^{3}He and ^{4}He with observations was excellent and in good agreement with other calculations. Looking at Figure 3.4 this does not come as much of a surprise. But what we can also see is that the ^{7}Li abundance prediction for the WMAP7 value of η seems not to agree with observations. Even though ^{7}Li has lost its importance as a baryometer with the advent of more reliable measurements of D and the high precision determinations of η, we will still discuss the *lithium problem*, which remains unsolved to this day.

3.3.3.1 The Missing ^{7}Li

^{7}Li is a very fragile isotope which is burning in stars at relatively low temperature. Consequently, most of the interstellar lithium cycled through stars is destroyed and it is difficult for stars to synthesize ^{7}Li and return it to the ISM before it is burned. ^{7}Li and other intermediate nuclei as ^{6}Li, ^{9}Be, ^{10}B and ^{11}B, can be synthesized via cosmic-ray nucleosynthesis, either by alpha-alpha fusion reactions or by spallation

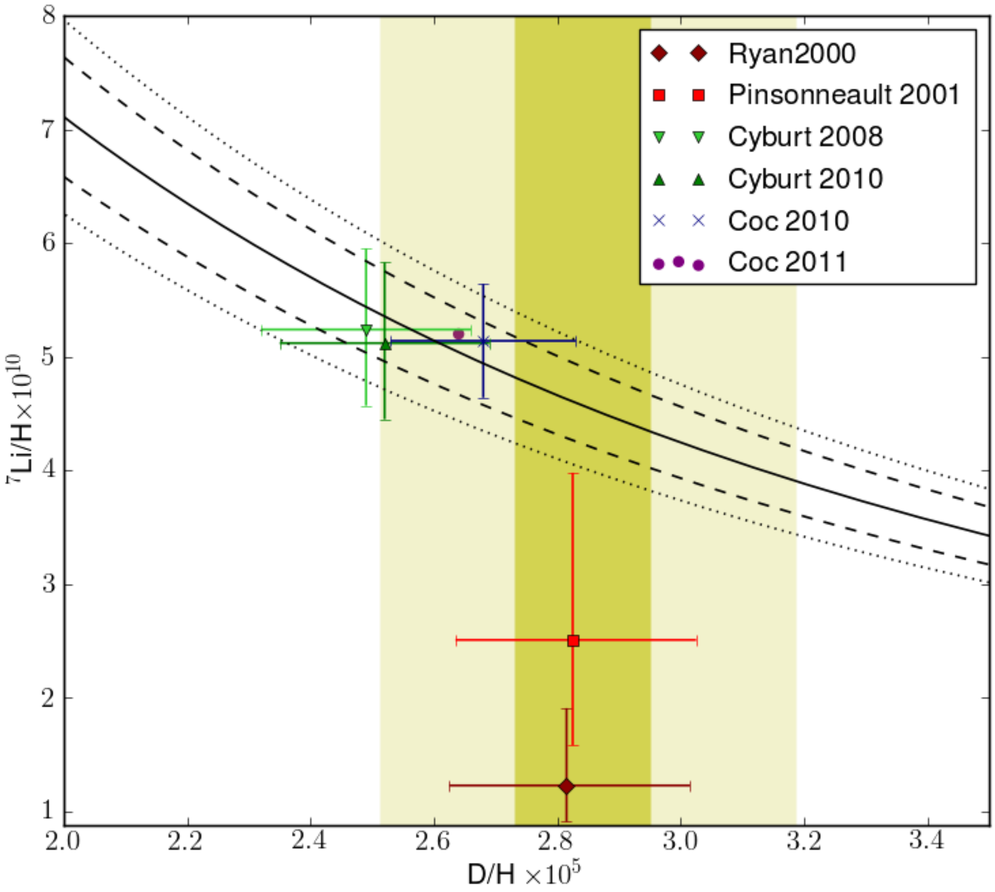

Figure 3.10: The solid line is the SBBN-predicted ^{7}Li abundance (relative to hydrogen) as a function of the deuterium abundance (relative to hydrogen). The dashed lines account for the improved theoretical uncertainties [31] (7.4%), the dotted lines for the adopted uncertainty of 12%. The vertical bands are the values of D/H consistent with the WMAP7 value of the baryon density (the dark yellow region corresponds to the variation of the mean value with η, the light yellow region includes the theoretical error $\sim 8\%$). The red square and dark red diamond with errorbars represent recent analysis of ^{7}Li observations by [112] and [103] respectively. The points are slightly shifted in D/H for better readability. The other datapoints are from recent SBBN calculations [24, 26, 31, 32].

reactions (nuclear breakup). However, in the early universe, when metallicity is low, the post-BBN production of lithium is expected to be subdominant to the BBN abundance. Hence, we would expect a lithium plateau at low metallicity (called "Spite plateau" after the authors of [122] who first discovered this plateau). The systems best suited for the observation of primordial ^{7}Li are warm metal-poor dwarf stars in the galactic halo. The observational data in Figure 3.9 confirms that lithium does not vary significantly for metallicities [Fe/H] [1] < -2. This plateau is a clear signal of the primordial origin of the low-metallicity lithium abundance. Extrapolation to zero metallicity found in a recent analysis [114] gives

---

[1] $[\mathrm{Fe/H}] \equiv \log_{10}(Y_{\mathrm{Fe}}/Y_{\mathrm{H}}) - \log_{10}(Y_{\mathrm{Fe}}/Y_{\mathrm{H}})_{\odot}$, where the subscript $\odot$ denotes the solar value.

$$^{7}\text{Li/H} = (1.58 \pm 0.31) \times 10^{-10} \tag{3.31}$$

which is a factor 3-4 times smaller than our predicted value. Over the last decades many attempts have been made to explain the reason for this difference. There are basically three different problems to tackle. The first is to infer from observations the amount of lithium in a star, the second is to relate the observed value to the primordial one and the third is to correctly model the SBBN of lithium. We will quickly discuss the problems in each field, for a much more detailed discussion see [111, 123] and references therein.

- **How much ^{7}Li do we observe?**
  The lithium abundance of metal-poor halo stars can not be observed directly, but is inferred from an absorption line strength and a model of the stellar atmosphere. The biggest difficulty in these models is to reproduce the temperature structure of the star whose spectrum is observed. The most important source of error is the surface temperature, differences as large as 150-200K between different calibrations are not uncommon. Higher temperatures would result in Li estimates higher by ~ 0.08 dex per 100K. Thus, accounting for a difference of ~ 0.5 dex would require a large offset of the stellar temperature. Another possible source of inaccuracies is the fact that the stellar atmosphere is modelled in 1D only.

- **Is the observed ^{7}Li primordial?**
  Another important source of systematic uncertainty comes from the possible destruction of ^{7}Li over the age of the observed stars. If there is some mixing between the outer layers of the star and the hot interior, lithium is destroyed little by little and disappears from the atmosphere of the star (depletion). There are various mechanisms which could cause such mixing like convection, rotational mixing or diffusion, but the relatively small scatter in the sample of stars that build the Spite plateau constrains the effect of depletion caused by mechanisms which vary from star to star to ~ 0.1 dex. A recent analysis based on both the observed abundance and a theoretical determination of the depletion [103] gives

  $$^{7}\text{Li/H} = \left(2.51^{+1.47}_{-0.93}\right) \times 10^{-10} \tag{3.32}$$

  which is already a factor two bigger than the previous value but also equipped with large errors.

- **Are the predicted values reliable?**
  As we already pointed out earlier, the ^{7}Li prediction carries the largest uncertainty. The most important reaction at the WMAP7 value for the baryon density is $^{3}\text{He}\,(\alpha,\gamma)\,^{7}\text{Be}$. A recent analysis of new experimental data [32] concludes that not only is the uncertainty on the ^{7}Li prediction reduced to $\sim 7.4\%$, but also that the predicted abundance is in fact increased. Thus the "nuclear fix" to the lithium problem is rather unlikely [37]. The discrepancy could also indicate that the standard big bang scenario is incomplete and non-standard effects based on new physics or exotic particles play an important role [25, 31, 64].

All three of these questions can not yet be answered convincingly and without doubt. Hence, the lithium problem remains unsolved for the moment. Nevertheless, in Figure 3.10 we compare our prediction to the above mentioned observations and recent calculations. As expected the agreement between calculation and observation is very poor. Predicted values from recent calculations, ${}^{7}\mathrm{Li/H} = \left(5.24^{+0.71}_{-0.62}\right) \times 10^{-10}$ [32], ${}^{7}\mathrm{Li/H} = \left(5.12^{+0.71}_{-0.62}\right) \times 10^{-10}$ [31], ${}^{7}\mathrm{Li/H} = (5.14 \pm 0.5) \times 10^{-10}$ [26], ${}^{7}\mathrm{Li/H} = 5.2 \times 10^{-10}$ [24], however, are in excellent agreement with our results indicating an overall consistency between SBBN calculations.

3.3.3.2 The Mysterious ^{6}Li

The lighter stable lithium isotope, ^{6}Li, is even more fragile than ^{7}Li and destroyed at lower temperatures. Its importance for BBN is small since it is only produced in tiny amounts. Calculations (including ours) yield an isotopic ratio ${}^{6}\mathrm{Li}/{}^{7}\mathrm{Li} \sim 10^{-5}$. It is thought to be produced predominantly by spallation. Since this mechanism requires cosmic rays, that are thought to be produced mainly by supernovae, elements produced by spallation should cumulate with star formation and thus be roughly proportional to metallicity. However, recent high-resolution observations of metal-poor halo stars [14] suggest the presence of a ^{6}Li plateau similar to the Spite-plateau for ^{7}Li, indicating a primordial origin. The observed isotopic ratios of ${}^{6}\mathrm{Li}/{}^{7}\mathrm{Li} \sim (5 - 10) \times 10^{-2}$ are three to four orders of magnitude higher than what is currently predicted in SBBN. If this large difference is to be explained by nucleosynthesis, we have to turn our attention to the key production reaction ${}^{2}\mathrm{H}\,(\alpha,\gamma)\,{}^{6}\mathrm{Li}$.

Recent measurements of the low energy cross section [52] have raised our hope for an increase of the SBBN predicted ^{6}Li abundance. The reaction rates provided in the original publication [52] as well as in a re-examination of their data [82] have been fitted in the REACLIB parametrization Eq.(2.60) [44]. The resulting fit parameters for the forward and backward reaction are presented in table B.1 and B.2.

The abundance predictions from calculations with these new reaction rates do not differ significantly from the original value, labelled *JINA* in table 3.2. While the ^{7}Li abundance (as well as all other abundances) is unaffected by the ${}^{2}\mathrm{H}\,(\alpha,\gamma)\,{}^{6}\mathrm{Li}$ rate, the ^{6}Li abundance does change, but not more than $\sim 20\%$. Interestingly, the reaction rate from the experimental group [52] leads to an increase of ^{6}Li, whereas the re-evaluated reaction rate of [82] actually reduces the final abundance.

Even with recent reaction cross sections we can not explain the amount of ^{6}Li which is claimed to be observed in metal-poor halo stars. If these observations are confirmed, sources other than SBBN would be required to reproduce these findings. Non-standard effects like annihilation of neutralinos [62] or decay of gravitinos [34] could provide alternative explanations. On the other hand, the detection of ^{6}Li is very difficult and it has only been observed in a handful of stars, so systematic errors cannot be completely excluded.

3.3.4 Nonstandard Big Bang

The standard model for the big bang, assuming a homogeneous and isotropic expansion, is very successful in explaining light element abundances and shows excellent agreement with observations (aside from the problems with lithium isotopes). However,

	JINA	[52]	[82]
^{6}Li/H $\left(\times 10^{-14}\right)$	1.31	1.43	1.06
^{7}Li/H $\left(\times 10^{-10}\right)$	4.58	4.58	4.58
^{6}Li/^{7}Li $\left(\times 10^{-5}\right)$	2.87	3.12	2.32

Table 3.2: Primordial isotopic lithium abundances for $\eta = 6.16 \times 10^{-10}$ and different $^{2}\mathrm{H}\left(\alpha,\gamma\right)^{6}\mathrm{Li}$ cross sections.

among the many extensions to the framework of SBBN we find nonstandard big bang nucleosynthesis (NSBBN) where the early universe is not assumed to be homogeneous, but displaying density fluctuations. Some calculations of such models show increased abundances of heavy elements [63, 76, 88, 109], while SBBN is not able to produce heavy elements at significant amounts. We studied the possibility for an enrichment of heavy elements (C,N,O and F) in NSBBN which would later form molecules important for stellar formation [134].

3.3.4.1 The Model

The model we use depends on small scale density perturbations which could be induced by baryogenesis [76] or some phase-transitions like the quark-hadron phase transition [50]. While the detailed origin is not of importance for our purposes we just assume the occurrence of such fluctuations and use the geometry as open parameter. We apply the two-zone model used in [109] where the densities ρ^h and ρ^l of two zones, with high and low density respectively, are related by the density ratio $R = \rho^h/\rho^l = \eta^h/\eta^l$ and the volume fraction $0 \leq f_v \leq 1$ of zone 1. While f_v and R are free parameters they are constrained by the demand that the averaged density has to reproduce the global value $\rho = f_v\rho^h + (1 - f_v)\,\rho^l$, leading to

$$\frac{\rho^h}{\rho} = \frac{R}{Rf_v + (1 - f_v)} \quad \text{and} \quad \frac{\rho^l}{\rho} = \frac{1}{Rf_v + (1 - f_v)} \tag{3.33}$$

Since the high temperature evolution (until weak freeze-out) is independent of density, the n/p-ratio (and thus the mass fractions of protons and neutrons) in both zones is given by the global value which is the same as in SBBN. From this initial condition the neutrons are assumed to diffuse out leading to an uniform neutron density, whereas the protons remain in place because of the short mean free path resulting from their charge. This will change the density contrast and the neutron density in both regions. Using superscripts 1 and 2 for this new situation while h and l indicate values before neutron diffusion this translates into $X_n^1\rho^1 = X_n^2\rho^2 = X_n\rho$ and $X_p^1\rho^1 = X_p\rho^h$, $X_p^2\rho^2 = X_p\rho^l$. We can now express local densities by the global quantities X_n, ρ and the parameters R and f_v

$$\rho^1 = X_n^1\rho^1 + X_p^1\rho^1 = X_n\rho + (1 - X_p)\,\rho^h \tag{3.34}$$

$$\rho^2 = X_n^2\rho^2 + X_p^2\rho^2 = X_n\rho + (1 - X_p)\,\rho^l. \tag{3.35}$$

Together with Eq.(3.33) the ratios ρ^1/rho and ρ^2/rho can easily be determined:

$$\frac{\rho^1}{\rho} = X_n + \frac{(1-X_n)\,R}{f_v R + (1-f_v)} \quad \text{and} \quad \frac{\rho^2}{\rho} = X_n + \frac{(1-X_n)}{f_v R + (1-f_v)}. \tag{3.36}$$

This relations now allow us to express the neutron and proton mass fractions in regions 1 and 2 as a function of the global freeze-out mass fractions and the parameters R and f_v

$$\begin{aligned} X_n^1 &= X_n \frac{\rho}{\rho^1} = \frac{X_n}{X_n + (1-X_n)\,R/\left(f_v R + (1-f_v)\right)} \\ X_p^1 &= X_p \frac{\rho^h}{\rho^1} = \frac{(1-X_n)\,R/\left(f_v R + (1-f_v)\right)}{X_n + (1-X_n)\,R/\left(f_v R + (1-f_v)\right)} \end{aligned} \tag{3.37}$$

$$\begin{aligned} X_n^2 &= X_n \frac{\rho}{\rho^2} = \frac{X_n}{X_n + (1-X_n)\,/\left(f_v R + (1-f_v)\right)} \\ X_p^2 &= X_p \frac{\rho^h}{\rho^2} = \frac{(1-X_n)\,/\left(f_v R + (1-f_v)\right)}{X_n + (1-X_n)\,/\left(f_v R + (1-f_v)\right)}. \end{aligned} \tag{3.38}$$

These relations now allow us to perform nucleosynthesis calculations for each zone individually, assuming global SBBN values for ρ and X_n at an initial temperature ($T_9 = 10$ in our case). We are aware that this model is an oversimplification, assuming two regions with uniform densities and complete neutron diffusion before the onset of nucleosynthesis, while proton diffusion is treated as negligible. Furthermore, we do not account for neutron (back-) diffusion into the proton rich zones during nucleosynthesis. These effects are discussed in detail in [109].

3.3.4.2 Results

Calculations have been performed for a network containing ~ 150 nuclides, ranging from free nucleons to magnesium. The reaction rates are taken from a recent compilation [4] where reaction rates important for BBN have been updated. At the time when these calculations have been performed the current WMAP value for the baryon to photon ratio was slightly higher than today $\eta = 6.22 \times 10^{-10}$. Table 3.3 gives relative abundances for a SBBN calculation and two selected NSBBN cases (the table is the same as in [134]). Relative abundances

$$[\xi] = n_\xi / n_b, \tag{3.39}$$

where n_ξ is the number density of species ξ and n_b the total number density, were chosen because it is the format needed as input for subsequent big bang chemistry calculations. The NSBBN abundances in the table are final abundances, already mixed from both zones in each model following

$$[\xi] = \frac{f_v \rho^1 \,[\xi]^1 + (1-f_v)\,\rho^2\,[\xi]^2}{\rho}. \tag{3.40}$$

The SBBN light element abundances in Table 3.3, corresponding to D/H $= 2.35 \times 10^{-10}$, $Y_p = 0.2498$ and ^{7}Li/H $= 8.02 \times 10^{-10}$, are in good agreement with observations as presented in the previous section, except for ^{7}Li, which shows an even higher abundance.

	SBBN	NSBBN	
		$(\mathrm{f_v} = 0.8;\ \mathrm{R} = 10)$	$(\mathrm{f_v} = 1 \times 10^{-5};\ \mathrm{R} = 1000)$
[H]	0.889	0.889	0.888
[D]	2.092×10^{-5}	2.45×10^{-5}	2.13×10^{-5}
[He]	0.111	0.111	0.112
[Li]	1.77×10^{-9}	1.97×10^{-9}	2.30×10^{-9}
[C]	2.51×10^{-15}	4.00×10^{-15}	8.45×10^{-14}
[N]	2.32×10^{-16}	2.46×10^{-16}	3.44×10^{-14}
[O]	3.22×10^{-19}	3.37×10^{-19}	8.20×10^{-17}
[F]	3.28×10^{-27}	3.61×10^{-27}	1.63×10^{-24}

Table 3.3: Relative abundances $[\xi] = n_\xi / n_b$ of the elements at the end of Big Bang nucleosynthesis for the SBBN and for two NSBBN scenarios.

This most likely results from an overestimation of the $^3\mathrm{He}\,(\alpha,\gamma)^7$ Be rate.

The values of f_v and R represent two extreme cases discussed below and were chosen in order to achieve the case, where the final NSBBN abundances of protons, deuterium and helium are as close as possible to the SBBN values and thus are still in accordance with observations.

The discussion of the different results follows the explanations given in [134]. The first case ($f_v = 0.8$, $R = 10$) is similar to the scenario discussed in [109]. The density ρ^1 has to stay close to the global value ρ, while ρ^2 is ten times lower. Assuming complete diffusion of free neutrons out of the high density region will lead to a large increase of the neutron abundance in the low density region. In the high density region nucleosynthesis will occur very similar to the standard case and all neutrons are consumed to form ^{4}He. However, in the low-density region neutrons are more abundant than protons, which will result in all protons being incorporated into ^{4}He with free neutrons left over. Neutron captures can then produce neutron-rich isotopes, bypassing the slow triple-*alpha* reaction and leading to heavy elements. We see, that while the heavy element abundances for this case are slightly higher than for the SBBN case, they remain almost at the same level. This was already pointed out in [109], where the finding occured, that light element constraints prevent considerable formation of heavy nuclei.

The second case we investigated ($f_v = 10^{-5}$, $R = 1000$) represents the inverted scenario, where pockets of extremely high density are embedded in a background of almost standard density. It was similarly introduced in [63] and later also discussed (for even more extreme cases) in [76, 88]. In the high density pockets, the path to heavy elements is opened by an efficient triple-α reaction ($\propto \rho^2$). At the same time ^{7}Li is destroyed more effectively which keeps its abundance relatively low. Therefore, this model considerably enhances heavy element production while light element abundances remain in accordance with SBBN. However, due to the small volume fraction of the high density region (which is necessary to reproduce the proper global density) the final heavy element abundances after mixing remain low, although two orders of magnitude higher than in the standard case. The possibility for considerable heavy element production in NSBBN scenarios has been discussed recently in [76]. However, the authors did not specify, whether their model reproduces the light element abundances correctly, leading to follow-up discussions [107, 75]. A recent preprint [88] indicates that appreciable amounts of heavy elements can be produced in an inhomogeneous big bang while retaining light element concordance.

Chapter 4

Formation of Heavy Elements

The term *heavy elements* refers to elements heavier than iron. Heavy elements are rare compared to the lighter elements (see Figure 1.1). But among them are all the elements one can find at the jeweller's: gold, platinum and silver. The question: "How were the heavy elements from iron to uranium made?" was chosen as one of *Eleven Science Questions for the New Century* by the *Committee on the Physics of the Universe* [27]. In this Chapter we try to shed some light on the problems we encounter, regarding the formation of heavy elements.

In Section 4.1 we will give a short description of stellar burning and the death of massive stars. The basic processes responsible for the production of the bulk of heavy elements, the s-process and the r-process are introduced in Section 4.2. After a general introduction on both processes, the r-process is put into focus and we discuss observational indications for the r-process (Section 4.2.1) as well as the conditions under which the r-process operates (Section 4.2.2). The rest of the chapter is dedicated to possible r-process sites (Section 4.2.3), and one scenario in particular, core collapse supernovae with strong magnetic field and rotation, that can form jets during the explosion (Section 4.3).

4.1 The Life and Death of Massive Stars

At the beginning of the life of every star is the gravitational collapse of molecular gas. Due to gravitational contraction, the temperature in the interior of the protostar increases until the central temperature is high enough to fusion hydrogen to helium. Due to the energy released by this fusion process, internal pressure increases and counterbalances the gravitational contraction. This allows for hydrostatic equilibrium in the star. Once hydrogen at the centre is exhausted,thermal pressure decreases and the star undergoes gravitational contraction. Due to this contraction, the central temperature rises until it reaches a critical value, where helium burning is ignited and the star is again in hydrostatic equilibrium. Hydrogen burning continues in a thin shell around the core. This sequence of nuclear burning, fuel exhaustion, contraction and ignition of the next burning stage is repeated a number of times, depending on the mass of the star. In each burning stage, the ashes of the previous stage are burnt. A massive star ($\geq 11\mathrm{M}_\odot{}^2$), remains during all burning stages (from hydrogen burning

---

[2] $\mathrm{M}_\odot = \mathrm{solar\ \ mass} = 1.9884 \times 10^{33}\mathrm{g}$

through helium, carbon, neon, oxygen, magnesium to silicon burning) in hydrostatic equilibrium. At the end of core silicon burning, the star has an onion-like structure, with a core consisting mostly of iron and nickel and alternating layers of nuclear burning shells and the accumulated ashes of each burning shell (Figure 4.1). The iron core does not undergo any further nuclear burning because no more energy can be gained from fusion of iron nuclei. This is due to the fact that iron nuclei are the most tightly bound nuclei (with a binding energy of ∼8 MeV per nucleon see Figure 2.2). The core is instead supported by the pressure of degenerate electrons. The silicon burning shell continuously produces iron nuclei and the mass of the core steadily increases. Once the core mass exceeds the Chandrasekhar mass limit

$$\mathrm{M_{Ch}} \simeq 1.44\,(2\mathrm{Y_e})^2, \tag{4.1}$$

which is the maximum mass of a self-gravitating sphere which can be supported by the pressure of a degenerate electron gas, it is no longer stabilized against gravitation and starts to contract.

The contraction leads to an increase in density and temperature, hence also the electron chemical potential and the electron Fermi energy increase. This facilitates electron captures on iron group nuclei and consequently a reduction of the electron pressure occurs, turning the contraction into a collapse. Additionally, small amounts of photodisintegrations of iron group nuclei convert internal energy into mass and reduce the radiation pressure which further accelerates the collapse. The continuous electron captures reduce Y_e, and $\mathrm{M_{Ch}}$ declines as a function of time, becoming a smaller fraction of the initial iron core. The fraction of the core with mass $\mathrm{M_{Ch}}$ is called *inner core* while the rest of the iron core is referred to as *outer core.*

The inner core collapses homologously, i.e. all layers at all radii collapse at the same rate causing the density to increase uniformly everywhere. The local sound speed is larger than the infall velocity which is proportional to the radius. At the edge of the homologous core the infall velocity reaches sound speed and is supersonic beyond that point (the sonic point). Thus the inner core, falling at subsonic velocities where matter can communicate (with sound speed), cannot communicate with the outer free falling envelope beyond the sonic point.

When the density in the inner core reaches values of the order of the nuclear density $\sim 10^{14}\,\mathrm{g/cm^3}$ the nuclei and free nucleons start to feel the nuclear force, which is repulsive at very short distances. The nuclear potential acts as a stiff spring that stores energy in the compressive phase until it becomes incompressible and rebounds. This creates a pressure wave which accelerates into a shock wave at the sonic point, moving outward with supersonic velocities. Typical kinetic energies in the shock after rebound are of the order of a few times 10^{51} erg. Meanwhile the outer core is still collapsing supersonically.

Unfortunately this so called *prompt shock* mechanism cannot explain why stars explode. As the shock wave moves outward it ploughs through the outer core consisting of iron group material. The temperature beyond the shock wave is high enough to photodisintegrate iron nuclei. The shock wave looses about 8×10^{18} erg per gram of matter which is dissociated. Based on the initial explosion energy only $0.25 - 0.5\,\mathrm{M_\odot}$ can be penetrated until the shock stalls. Taking into account energy loss via neutrinos, leaking out energy from behind the shock, further reduces the amount of matter the

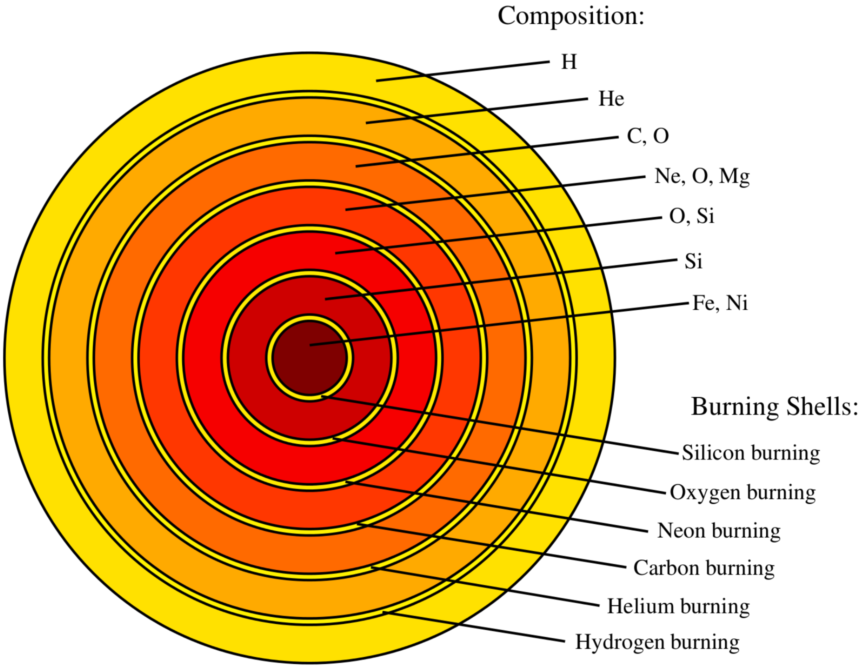

Figure 4.1: Schematic structure of the different shells of a fully evolved massive star (not to scale). The upper right part shows the most prominent constituents of each layer. Between the layers of different composition nuclear burning continues in thin shells. The burning shells are labelled in the lower right part with the corresponding fuel. The iron core at the centre has been accumulated in silicon burning and does not provide any further energy.

shock can pass before losing all its kinetic energy.

How exactly the shock is revived and how it will ultimately propagate through the stellar layers beyond the iron core and disrupt the star in a core collapse supernova explosion is still unknown. A promising scenario is the *delayed neutrino heating mechanism*[18] where the shock is revived by neutrinos emitted by the nascent neutron star at the centre. The collapse of the inner core into a proto-neutron star released a few times 10^{53} erg in gravitational energy which is radiated away by neutrinos. If only $\sim 1\%$ of this energy could somehow be transformed into kinetic energy of the baryonic matter, the typical supernova energy would emerge.

Supernovae are considered to be the main contributors to nucleosynthesis in galaxies. The explosive destruction of a star does not only enrich the interstellar medium with the products of stellar nucleosynthesis but also provide conditions necessary for the synthesis of elements heavier than iron. We will discuss core collapse supernovae as possible r-process site in Section 4.2.3.

4.2 The s- and r-Process

We have seen in the previous section that in stars only elements up to the iron group are synthesized. Because the binding energy per nucleon reaches its maximum in the iron group, the production of heavier elements by direct fusion is endothermic. Another obstacle to the production of heavy elements is the growth of the Coulomb barrier with increasing proton number Z. At sufficiently large Z the energy needed to overcome this

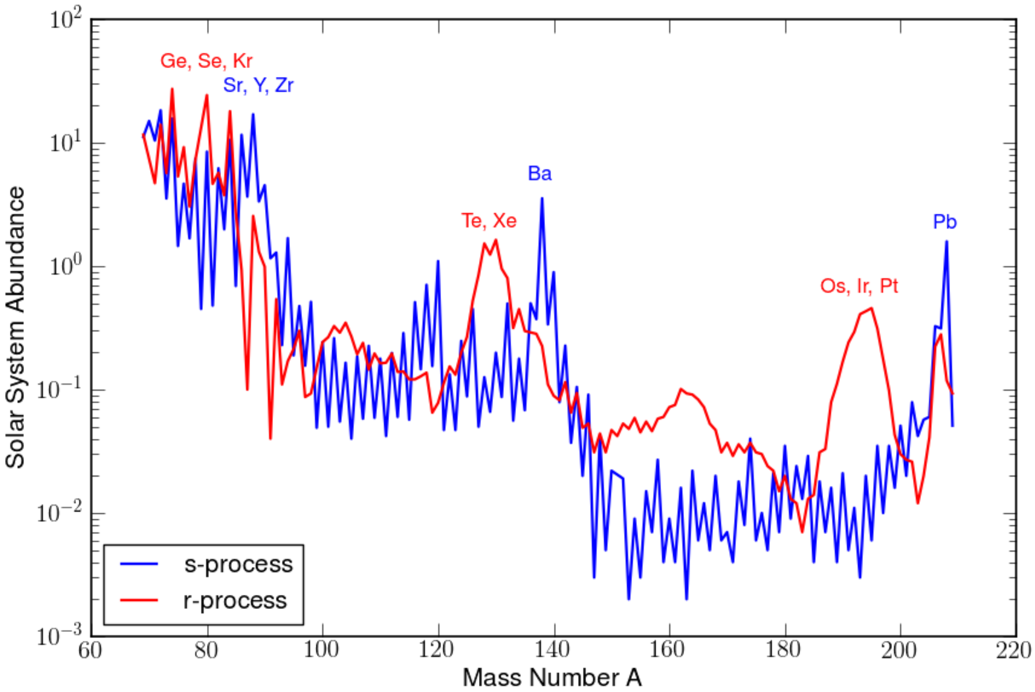

Figure 4.2: Breakdown of solar system heavy element abundances into r-process and s-process contributions. The values are based upon the Si=10^6 (meteoritic) scale (adopted from [119]). The annotated names denote the most prominent element(s) in the individual peaks.

barrier is so high that the synthesized nuclei will be photodisintegrated immediately and reactions with charged particles become impossible. The neutrons, however, are not affected by the Coulomb repulsion and therefore the isotopes of elements beyond Fe are almost exclusively produced in neutron capture processes. In an interplay of neutron captures and β-decays, element production progresses from the Fe group to the heaviest elements of the periodic table [20, 22]. This process can be characterized by the relation between the time it takes for a nucleus to capture a neutron, i.e. the neutron capture timescale τ_n, and the competing timescale τ_β for the nucleus to undergo β-decay. It is important to note that τ_β only depends on the nuclear species, whereas τ_n depends crucially on the neutron density.

If neutron captures are slow, compared to the competing β-decays ($\tau_\beta \ll \tau_n$), the process is called *slow neutron capture process* or **s-process**. In this case, a seed nucleus captures neutrons until a β-unstable nucleus is formed. This nucleus β-decays, before it can capture another neutron, into the isobar with charge Z+1. Thus the path to heavy elements remains close to stability in the s-process. The involved nuclei are in general sufficiently long-lived to be studied in the laboratory. The nature of the s-process is also expressed in the final abundance distribution. For nuclei with closed neutron shells, at N=50, 82 and 126, the neutron capture cross-sections are much smaller than for neighbouring nuclei with different neutron numbers. Therefore, isotopes with magic neutron numbers will be considerably more abundant. This results in three prominent peaks in the solar s-element abundance distribution (Figure 4.2), around A=90, 140 and 208.

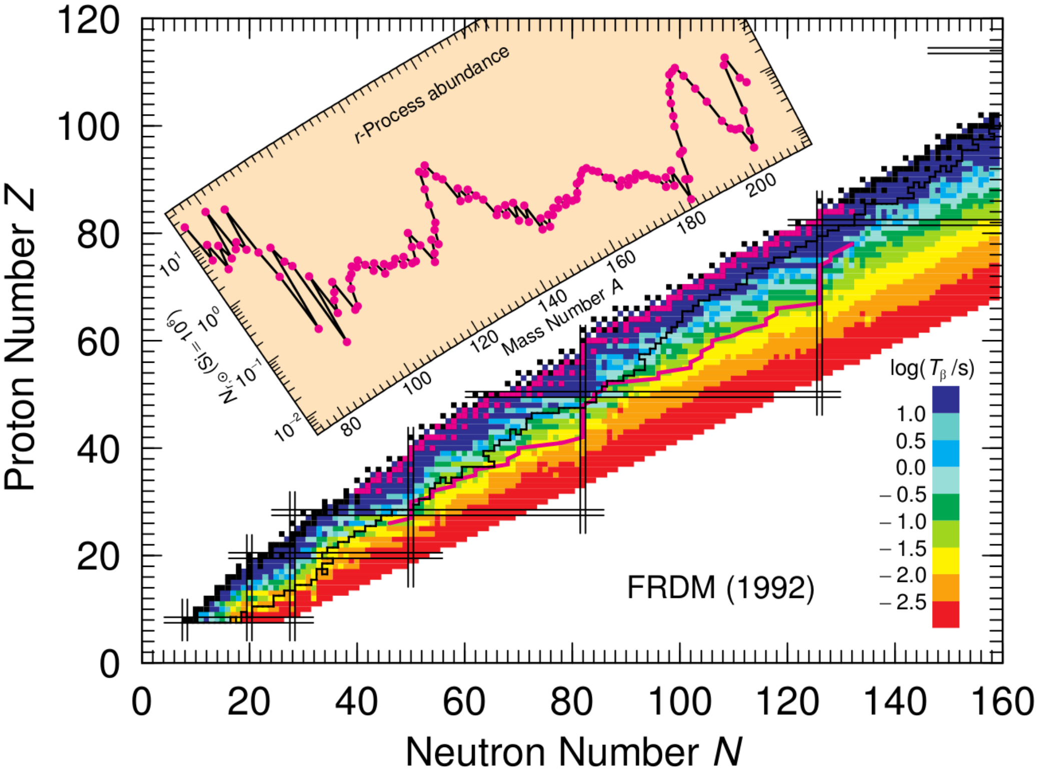

Figure 4.3: Features of the r-process: Black squares denote β-stable nuclei. Where available, experimental masses were used to determine the location of stable nuclei; otherwise, calculated masses were used. The coloured region in the main graph shows calculated half-life with respect to β-decay. The jagged black line gives the right-hand boundary of the region of known nuclei. The thick magenta line corresponds to $S_{1n} = 2.4$ MeV, which is the approximate location of the r-process path for a particular set of stellar conditions. The magenta squares in the region of β-stable nuclei show nuclei that are created in decay from the r-process line. The observed solar r-process abundance is plotted versus the mass number A in the inset (figure adopted from [84]).

In the other extreme case, $\tau_n \ll \tau_\beta$, the timescale for neutron capture is rapid on the competing timescale for β-decay. Thus, the process is called the *rapid neutron capture process* or simply **r-process**. A nucleus will capture many neutrons before an isotope is reached that β-decays before another neutron is captured. This allows to reach nuclei very far from stability and to enter regions where no experimental data exists (see Figure 4.3). Therefore, one has to rely on theoretical models for the nuclear properties of neutron rich nuclei that participate in the r-process.

The high neutron fluxes under which the neutron capture timescale becomes sufficiently short, are usually accompanied by high temperatures (~1 GK) and therefore large quantities of high energy photons causing photodisintegration. If the timescale for photodisintegrations is of the order of τ_n, an equilibrium, the so called $(n,\gamma) - (\gamma,n)$ equilibrium, is established between neutron captures and photodisintegrations. The farther away a nuclide is from stability, i.e. the more neutrons a nucleus has captured, the lower its neutron separation energy, i.e. the energy needed to remove one neutron, becomes and the easier it can be photodisintegrated. Within an isotopic chain in equilibrium, there are usually one or two isotopes which dominate the abundance distribution. These isotopes are called *waiting point* nuclei, because the whole process has to wait until these nuclei β-decay before it can proceed in the next isotopic chain. The line connecting the waiting points of all isotopic chains is referred to as the *r-process path.* The r-process path is located far away from stability in the very neutron rich region of the nuclide chart, typically at nuclei with neutron separation energies around 2-3 MeV (see Figure 4.3). Waiting point nuclei with magic neutron numbers, corresponding to closed neutron shells as in the s-process, are bottlenecks on the r-process path. Their β-decay halflives are considerably longer, typically one or two orders of magnitude, than those of the waiting points between them. Therefore, these nuclei will be by far the most abundant. Once the flux of neutrons is exhausted, the unstable, neutron rich nuclei are not supported by the equilibrium anymore and will decay until they reach the valley of stability. The bulk of matter, concentrated in the waiting point nuclei with magic neutron numbers, will form peaks in the final abundance distribution. Compared to the s-process peaks they are located at lower mass because magic neutron numbers are reached at smaller proton numbers in the r-process.

The s- and r-process contribute almost equally to the total solar system abundance of heavy isotopes. Figure 4.2 shows a decomposition of solar system abundances into s-process and r-process contributions given in [119]. Such a breakdown is done by first determining the s-process contribution from model calculations and then attributing the residual abundances to the r-process.

In general, the s-process is much better understood than the r-process. Not only are the model calculations more reliable, because of the experimentally determined nuclear properties, but also the primary sites where the s-process operates are identified. It could also be seen to operate in situ by detecting the radioactive s-process isotope ^{99}Tc ($\tau_{1/2} = 2.1 \times 10^5$ years) in quiescently evolving stars [77]. For the r-process, however, neither the specific physical conditions and nuclear properties nor its astrophysical sites have been unambiguously identified.

4.2.1 Clues from Abundance Observations

The abundance distribution on the surface of a star does not change much during its evolution. Hence, it reflects the composition of the interstellar matter from which the star formed. Much of the knowledge we have, regarding the formation of the heaviest elements has been gained from high-resolution spectroscopic observations of stars in our galaxy, especially of the so-called *ultra metal-poor halo stars.* These halo stars are circling the galaxy in highly eccentric orbits and are among its very oldest stars. Compared to the sun, their Fe abundances are orders of magnitude lower, but they do already have clear signatures of elements made in the r-process. However, no indication for the presence of s-process elements has been found. This implies that no significant amounts of s-process material had been ejected into the interstellar medium when the very old halo stars formed. Meaning, that the r-process predates the s-process.

One of the most famous and best studied of these halo stars is CS 22982-052. Its metallicity, [Fe/H] ~ -3.1, is less than a thousandth that of the sun. Abundances or significant upper limits are reported for 57 elements in this star, more than for any other star except for our sun [120]. Figure 4.4 shows relative abundances of the

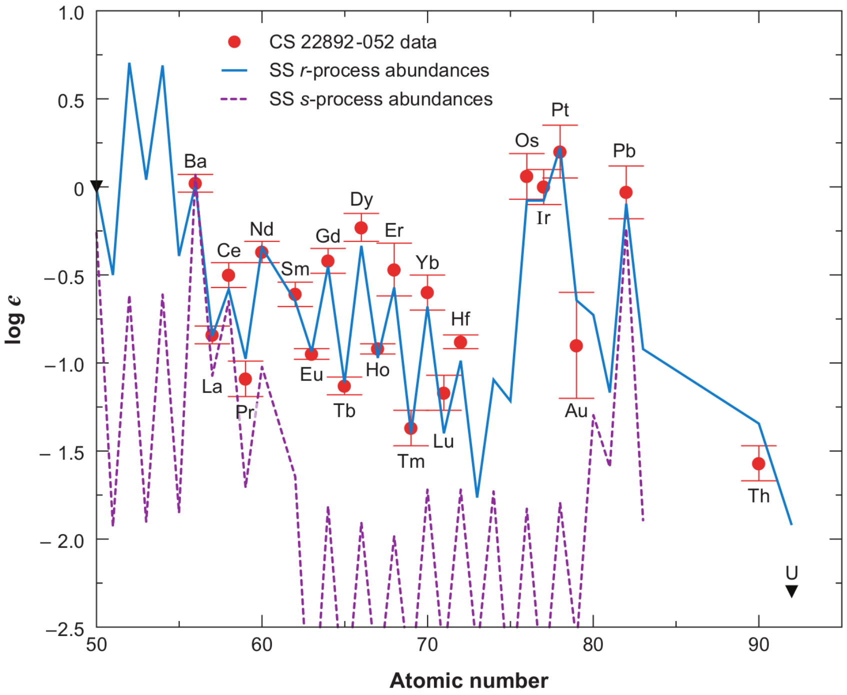

Figure 4.4: Comparison of CS 22892-052 Z$\geq$ 56 abundances with solar-system s-process (*purple dashed line*, normalized to CS 22892-052 Ba) and r-process (*solid blue line* normalized to CS 22892-052 Eu) elemental abundance distributions. Abundances are given relative to hydrogen: $\log \epsilon(\mathrm{A}) = \log_{10}(\mathrm{Y_A}/\mathrm{Y_H}) + 12.0$ (figure adopted from [119]).

measured CS 22982-052 data[121] compared to solar system s- and r-process abundances [28, 118]. The solar system abundances are scaled to compensate for the sun's greater metallicity. The s-process curve clearly does not fit the data at all, whereas the r-process curve shows a remarkable agreement with the measured abundances from Ba (Z=56) through the third r-process peak. Therefore, r-process production must have occurred already at very early galactic epochs. Assuming a relatively short time between the formation of the galaxy and the formation of these stars, the r-process production sites must have been short-lived. This suggests that the first stars, progenitors of the observed halo stars, were massive and evolved quickly. These objects needed to synthesize, eject and mix the r-process material into the interstellar medium prior to the formation of the ultra metal-poor halo stars. This points to a well-confined set of astrophysical and nuclear conditions, that are responsible for r-process nucleosynthesis, and suggests a relatively narrow range of masses for the astrophysical sites; presumably supernovae.[119]

Observations of further ultra metal-poor stars have confirmed the agreement with scaled solar system abundances for elements between barium and lead ($56 < Z < 82$). This indicates that these elements are always produced in the same way by a *robust* process, often referred to as *main r-process*. For elements between strontium and silver ($38 < Z < 47$), there is a large star-to-star scatter with respect to the heavier elements. This indicates an additional contribution for the production of those *lighter heavy elements*. This contribution may be associated with an additional process, the so-called light element primary process (LEPP) [81, 132].

It is still unclear whether different sites are required for r-process nucleosynthesis or even what the sites for these various mass ranges of neutron capture elements observed in the ultra metal-poor halo stars might be. In the next section we will discuss the requirements for a successful r-process and possible candidates that fulfil these. We will, however, only focus on the main r-process and simply refer to it as *r-process.*

As an additional observational constraint we can consider the mass of r-process material in the galaxy. From meteoritic data and observed abundances in the sun, we can infer that the mass fraction of r-nuclei in the Galaxy is $\sim 2 \times 10^{-7}$ [8]. If the mass of our galaxy is about $1.5 \times 10^{11}\,\mathrm{M}_\odot$, the mass of r-process material in our galaxy is about $10^4\,\mathrm{M}_\odot$. Now let's assume that the r-process site is somehow related to core collapse supernovae. The rate of supernovae in our galaxy is between $0.1\,\mathrm{yr}^{-1}$ and $0.01\,\mathrm{yr}^{-1}$ [127, 133] and the galaxy is about 10^{10} years old. Therefore, there have been some 10^8 to 10^9 supernovae in our galaxy's history. If each of these supernovae produced r-process material, we expect each supernova to make 10^{-5} to $10^{-4}\,\mathrm{M}_\odot$ of r-process nuclei. This is only a small amount of the total mass ejected in a supernova, and it's smallness provides an important constraint on the site of the r-process.

4.2.2 Conditions for the r-Process

Regardless of the astrophysical site there are two key ingredients for the r-process to operate (1) a strong flux of free neutrons and (2) an abundance of so called *seed nuclei* (usually Fe group nuclei) to capture them. To synthesize nuclei with A above 200 a seed nucleus needs to capture 100-150 neutrons. The neutron-to-seed ratio at the onset of the r-process is therefore a critical parameter to determine how far it will reach. The large neutron densities that are required (typically $10^{24} - 10^{28}\,\mathrm{cm}^{-3}$) and the fact that the neutrons have to be utilized before decaying with a halflive of 10 min, both point towards explosive environments.

To discuss the detailed conditions for the r-process we will assume a generic scenario of expanding and cooling hot matter, originating from some explosive event (e.g. a supernova). Initially the matter is assumed to be hot and dense enough to be in NSE. The abundance distribution in NSE, Eq.(2.54), depends on temperature, density and the abundance of neutrons and protons. To reduce the number of variables we will rather use entropy (instead of temperature and density) and electron fraction (instead of neutron and proton abundance) to discuss different scenarios. Thus for different values of entropy, the NSE abundance of some heavy nucleus with mass A depends on $\mathrm{S}^{1-\mathrm{A}}$ [78]. The recombination temperature, i.e. the temperature at which the NSE abundance distribution shifts to heavy nuclei, depends only weakly on density. Therefore, the density at which this temperature is reached is given by the entropy of the material. Nucleons expanding at low entropy will combine to heavy nuclei already at high densities, whereas nucleons expanding at high entropy will combine to form heavy nuclei at low densities. This difference gives rise to two very different r-process scenarios.

If the entropy is low, NSE favours iron-group nuclei and by the time the charged particle reactions freeze-out, all protons are bound into seed-nuclei. Because the r-process needs around 100 free neutrons per seed, a typical seed nucleus in a low-entropy freeze-out like ^{78}Ni requires a total neutron to proton ratio of $\sim 5 - 6$ which translates into an electron fraction of $Y_e \approx 0.15$, which is quite neutron rich. This scenario is often called the *low entropy low* Y_e scenario.

For high entropies NSE favours ^{4}He at high temperatures. Heavier nuclei can only be formed once the temperature is low enough that ^{12}C can be synthesized in significant amounts, mostly via the triple-α reaction. As we have already seen in the previous sections, three-body reactions depend strongly on the density. The higher the entropy at a given temperature the lower the density and therefore the slower the three body reactions. Eventually the three-body reactions are too slow to maintain NSE and freeze-out of equilibrium. Thus the higher the entropy, the higher the temperature at which three-body reactions freeze-out and the lower the abundance of heavy nuclei. At the moment NSE breaks down, there will be a lot of α-particles. Some of those are rapidly captured on ^{12}C and heavier nuclei to build up seed nuclei in the mass range $A \approx 100$. Once these reaction also freeze-out the system is left with free neutrons, some seed nuclei and many ^{4}He nuclei. The remaining neutrons will be captured by the seed nuclei but not by the ^{4}He nuclei and an r-process can occur. Because seed nuclei are scarce less free neutrons are needed than in the low entropy case and an electron fraction only slightly below $Y_e = 0.5$ might be sufficient for an r-process to occur. This scenario is called the *high entropy, moderate* Y_e scenario.

The question is, where in nature does on find the appropriate conditions, either very neutron rich matter at low entropies or moderately neutron rich matter at very high entropies.

4.2.3 Possible Candidates

The most promising candidate for the high entropy scenario is the so-called *high-entropy neutrino wind* [136] of core collapse supernovae. After collapse, core bounce and successful launch of a shockwave, the newly formed neutron star at the centre of the supernova is still very hot. It can solely loose energy and cool by the release of copious amounts of neutrinos. These neutrinos interact with the outermost neutron star layers which are heated and ejected in a continuous wind of matter. In the region behind the shock, densities are relatively low because matter is mostly pushed outwards. This cavity is heated by neutrinos, leading to the high entropies that are needed for the r-process. Furthermore, the interaction of neutrinos with free neutrons and protons is supposed to drive matter slightly neutron rich. The mass loss rate in the wind is estimated to be of order $10^{-5}\,\mathrm{M}_\odot\,\mathrm{s}^{-1}$ [33]. If the wind lasts for the early cooling time of the neutron star (~ 10s) and the material forms r-process matter, this would naturally give the correct amount of $10^{-4}\,\mathrm{M}_\odot$ of ejected r-process material.

Large scale parameter studies based on this scenario have been undertaken by many groups (see e.g. [10, 36, 42] or [128] for a recent review) and the solar r-process distribution could be very well reproduced by a superposition of different entropy contributions. Unfortunately, the very high entropies needed for the production of the heaviest elements could not be reproduced in simulations so far. Additional models like the formation of reverse shock in the late phase of the neutrino wind [9] or the triggering of the explosion by a quark-hadron phase transition after the first bounce [39] are currently being investigated. In this thesis, however, we will wander off the beaten track and focus on a candidate of the group of low entropy scenarios.

A possible alternative to supernovae as r-process site are neutron star mergers. The ejecta from the last seconds of a merger between a neutron star and a compact binary

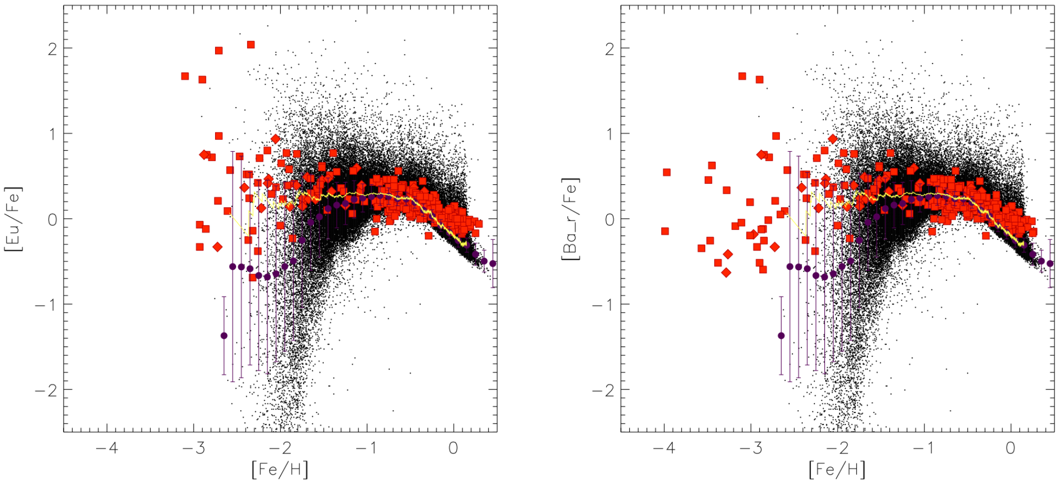

Figure 4.5: Evolution of [EU/Fe] and [Ba^{r}/Fe] abundances as a function of metallicity [Fe/H]. Neutron star mergers with a rate of $2 \times 10^{-4}\,\mathrm{y}^{-1}$, a coalescence timescale of 10^{6} y and $10^{-3}\,\mathrm{M}_{\odot}$ of ejected r-process matter are assumed to be the dominating r-process sources. Black dots denote model stars, observations are marked by filled squares and diamonds. Average ISM abundances are marked by a yellow line. Filled circles with error bars denote average abundances of model stars and their standard deviation in [Fe/H] bins with binsize 0.1 dex (figure adopted from [11]).

partner (either another neutron star or a black hole) could be so neutron rich that a low-entropy r-process could take place [71]. Such a compact binary pair gradually loses energy by gravitational radiation and tidal interaction over billions of years before its cataclysmic merger. The rate of such mergers in the galaxy is, at most, one every 10^{4} years. The enormous density of free neutrons available in these scenarios (about 10^{33} cm^{-3}) leads to the buildup of the heaviest elements and also to fission on very short time scales. That, in turn, leads to a recycling of fission products back to the heaviest nuclei via subsequent neutron captures. The abundance distribution after this so-called fission-cycling depends strongly on uncertain fission details and lacks any r-process nuclei lighter than , $A \approx 130$. Nevertheless, the solar-system r-process distribution can be reproduced very well[43, 92]. The amount of neutron rich matter that is ejected has been estimated in simulations with approximated general relativity [91] to be between $10^{-3}\,\mathrm{M}_{\odot}$ and a few times $10^{-2}\,\mathrm{M}_{\odot}$.

Neutron star mergers seem to be the perfect candidate to explain the r-process element abundances in the universe. Unfortunately studies of chemical evolution seem to rule out neutron star mergers as a major r-process source [11]. Even with a timescale for the mergers which is orders of magnitude lower than the classical estimate (10^{6} y instead of 10^{8} to 10^{9} y) the injection of r-process elements into the interstellar medium would occur very late during galaxy formation ([Fe/H] ≈ -2.5), whereas r-process elements are already observed at [Fe/H] $= -3$ and lower (see Figure 4.5). We will now revert to core collapse supernovae as possible r-process site, but focus on those with high magnetic fields and rotation rates.

4.3 MHD-Jets from Core Collapse Supernovae

An additional explosion mechanism to the ones presented in the first section of this chapter, is to include effects of rotation and magnetic fields. This magnetohydrodynamic (MHD) mechanism [73] results in aspherical supernovae with collimated jets in polar direction along the rotational axis. The neutron rich material inside the jets is expanding at high velocities from an initially dense state and could thus provide the high neutron densities, low entropies and short timescales needed for a successful r-process.

The basic idea behind the MHD mechanism is to extract the free energy, available in differential rotation of the proto-neutron star, with the help of magnetic fields, which in turn power the explosion. The free energy in differential rotation is the difference between the rotational kinetic energy and the kinetic energy for solid body rotation at the same total angular momentum. Depending on the initial spin profile, the free energy available in differential rotation to be tapped to generate strong magnetic fields and MHD jets varies from insignificance ($\sim 0.01\,\mathrm{B}$[3]) to supernova ($\sim 1\,\mathrm{B}$) and hypernova ($\gtrsim 10\,\mathrm{B}$) magnitudes [96].

The collapse of the stellar core leads to matter compression. Magnetic flux conservation would then amplify both the toroidal (B_Φ) and the poloidal (B_P) fields. Differential rotation in the region between the stalled shock and the inner proto-neutron star leads to a winding and stretching of the poloidal field into a toroidal field, thus driving the latter to higher and higher values. Eventually, magnetic pressure reaches high enough values and a magnetically driven jet punches through the stalled shock along the poles, powering a bipolar explosion. The structure of the magnetic field in the jets is that of a tightly coiled spring. Matter moves along the field lines like a bead on a spring, revolving around the poles and thereby being accelerated upwards in a corkscrew motion.

Matter which is accreted along the equator first passes through a shock surface where temperature suddenly rises and iron group nuclei are dissociated almost entirely into free neutrons and protons. During the very short infall near the proto-neutron star the electron fraction decreases through electron captures on protons, which occur on a much shorter timescale than electron captures on iron group nuclei. High temperature and density further facilitate electron captures. Because of the spiralling motion inside the jets, matter stays in the hot and dense region close to the neutron star in the first moments of ejection and additional electron captures decrease Y_e even further. During ejection, temperature and density quickly decrease due to fast expansion, thus possibly providing conditions suitable for the r-process.

---

[3] $1\mathrm{B} = 10^{51}\,\mathrm{ergs} = 10^{44}\,\mathrm{J}$

Chapter 5

Results

Nucleosynthesis calculations investigating the r-process are computationally involved. As we have seen in Section 2.3.4 the solution of the reaction network equations requires the inversion of a matrix, where the number of lines and columns equals the number of nuclides considered in the network. For r-process calculations, the number of involved nuclei is typically $\sim 5000 - 6000$. We performed all calculations in this section with a network code, which was developed in the course of this thesis. The code is a modernized version of the network code by F.-K. Thielemann, based on the same numerical methods, but written entirely new. We have made use of some new features of Fortran 90, that were not available in Fortran 77, like allocatable arrays and modules. Also, the combination of a fast sparse matrix solver and a compressed storage format rendered the code fast enough, that we can follow the evolution of all nuclei throughout the whole calculation. This was not possible with the old version, where the computation was split into a charged-particle part at high temperatures, and a specialized r-process part at lower temperatures (see e.g. [10, 36, 80] for details). The computation time for a calculation evolving the abundances over 10^6 s is typically less than 10 minutes.

The theoretical reaction rates and nuclear properties of all nucleosynthesis calculations in this section are based on the finite range droplet model (FRDM) mass formula [85]. The basic REACLIB, containing neutral and charged particle reactions and decays (theoretical as well as experimental) for $Z \leq 83$ is taken from [110]. For weak interaction rates (electron/positron captures and β-decays) we use the rates of [49] for nuclei with $A \leq 45$ and those of [70] for $45 < A \leq 65$. Neutron capture rates and their inverses, based on FRDM, for nuclei with $Z > 83$ are taken from [99]. Where available we used experimental β- and α-decay halflives from [5]. Theoretical β-decay halflives as well as β-delayed neutron and α-emission probabilities are taken from [86] and theoretical α-decay rates from [85]. We also include neutron induced fission rates from [99] and β-delayed fission probabilities from [97] based on the fission barrier predictions from [83].

This chapter is organized as follows: In Section 5.1 we present results from parametrized calculations and discuss the influence of Y_e, density and expansion velocity on the final abundance distribution. The influence of different fission chanels and fragment mass distributions is explored in Section 5.2. The main results of this thesis are presented throughout Section 5.3. Two different methods to extract initial conditions from 3D simulations are employed. The first is based on Lagrangian tracer particles (Section 5.3.2), the second makes use of the full 3D data from the simulation

Nuclide	A	Nuclide	A	Nuclide	A	Nuclide	A	Nuclide	A
n	1	V	43-83	Pd	102-156	Tm	167-230	U	232-299
H	1-3	Cr	44-86	Ag	105-160	Yb	168-234	Np	235-302
He	3-6	Mn	46-89	Cd	106-163	Lu	173-237	Pu	238-305
Li	6-9	Fe	47-92	In	111-166	Hf	174-240	Am	241-308
Be	7-12	Co	50-96	Sn	112-169	Ta	179-243	Cm	244-311
B	8-14	Ni	51-99	Sb	119-172	W	180-247	Bk	247-314
C	9-18	Cu	57-102	Te	120-176	Re	183-250	Cf	250-319
N	12-21	Zn	57-105	I	123-179	Os	184-253	Es	253-322
O	13-22	Ga	60-108	Xe	124-182	Ir	189-256	Fm	256-325
F	17-26	Ge	61-112	Cs	129-185	Pt	190-260	Md	258-328
Ne	17-41	As	64-115	Ba	130-189	Au	195-263	No	259-331
Na	20-44	Se	65-118	La	135-192	Hg	196-266	Lr	261-334
Mg	20-47	Br	68-121	Ce	136-195	Tl	203-269	Rf	265-337
Al	22-51	Kr	69-124	Pr	141-198	Pb	204-273	Db	267-336
Si	24-54	Rb	74-128	Nd	142-201	Bi	209-276	Sg	271-337
P	26-57	Sr	77-131	Pm	143-205	Po	210-276	Bh	274-337
S	27-60	Y	79-134	Sm	144-208	At	211-279	Hs	278-337
Cl	31-63	Zr	81-137	Eu	151-211	Rn	215-269	Mt	280-337
Ar	31-67	Nb	83-140	Gd	152-214	Fr	218-280	Ds	284-337
K	35-70	Mo	86-144	Tb	155-218	Ra	222-283	Rg	288-337
Ca	35-73	Tc	90-147	Dy	156-221	Ac	224-288		
Sc	39-76	Ru	96-150	Ho	161-224	Th	227-293		
Ti	40-80	Rh	101-153	Er	162-227	Pa	230-296		

Table 5.1: Nuclei contained in the r-process network, the range of mass number (A) is determined by the mass formula FRDM for each element. The total number of nuclides adds up to 5831.

(Sections 5.3.3 and 5.3.4). In Section 5.3.5, the results of both methods are compared, and contrasted with results from literature. Finally, in Section 5.3.6 we present a preliminary exploration of the influence of our results on galactic chemical evolution.

5.1 Results from Standard Calculations

To study the effects of different input parameters on the r-process abundance distribution we performed a series of parametrized calculations. The main goal was to test whether the conditions we expect inside the jets from CCSN are suitable for a successful r-process. We assume that matter inside the jets is expanding adiabatically once it has reached a certain distance from the proto-neutron star. We also assume that the jet traverses the outer layers with approximately constant velocity v_0. The position, density and

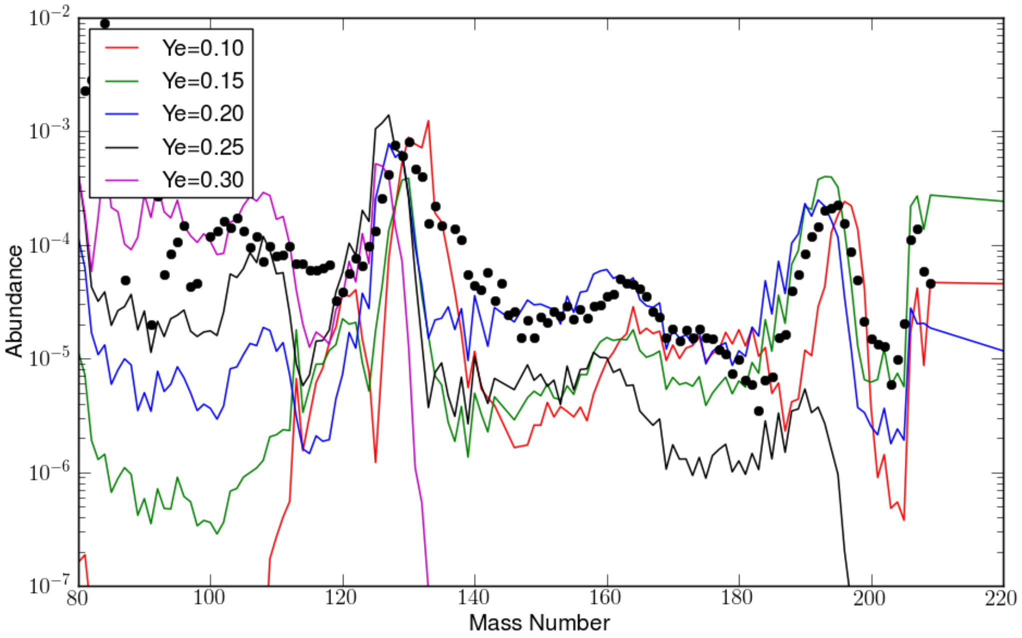

Figure 5.1: Results of standard calculation (see text) with different values of the initial electron fraction. Scaled solar r-process abundances from [119] are plotted for comparison (black dots).

temperature of a particle are then set to be [45]

$$\begin{aligned} R(t) &= R_0 + v_0 t \\ \rho(t) &= \rho_0 \left[\frac{R_0}{R(t)}\right]^3 \\ T(t) &= T_0 \frac{R_0}{R(t)}. \end{aligned} \tag{5.1}$$

We set the reference initial values for these parameters to

v_0	R_0	$T_{9,0}$	ρ_0
30000 km/s	350 km	10	2×10^9 g/cm^3

corresponding to a dense MHD Jet with a radial velocity of 0.1 c. The initial temperature is sufficiently high that it is safe to assume that matter is in NSE. In that case the abundance distribution depends only on the thermodynamic conditions, the electron fraction and the abundance of neutrons and protons. The initial composition can then be calculated from NSE by assuming that only free neutrons and protons exist. Their initial abundances are defined by charge neutrality $Y_p = Y_e$ and mass conservation $Y_n = 1 - Y_p$. Once the temperature has dropped below 9 GK we switch from the simplified NSE calculation to the full network calculation. At such a high temperature we can assure a smooth transition from NSE to the network. The physical breakdown of NSE occurs only later at temperatures around 6 GK. Using the full network calculations, the freeze-out proceeds consistently as soon as the first reactions fall out of equilibrium. Calculations are performed over a time of 10^7 s, after which the remaining unstable nuclei with a halflive of less than 10^9 y instantaneously decay to stability.

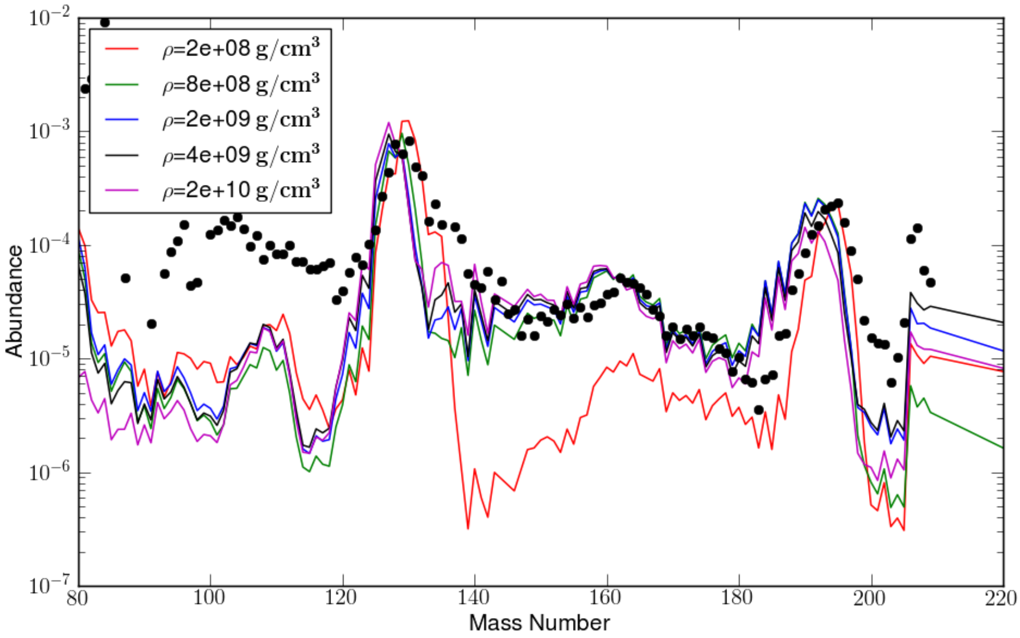

Figure 5.2: Results of standard calculation (see text) for different initial values of the density. Scaled solar r-process abundances from [119] are plotted for comparison (black dots).

Figure 5.1 shows the results of standard calculations for initial electron fractions of 0.1, 0.15, 0.2, 0.25 and 0.3. The outcome of the calculations depends strongly on the value of Y_e. In the three most neutron rich scenarios the full range of r-process elements over the second ($A \sim 130$) and third peak ($A \sim 195$) are produced. Under less neutron rich conditions ($Y_e = 0.25$) only the second peak can be reproduced, including some material with higher mass. For the least neutron rich calculation only lighter heavy elements with mass lower than 130 are synthesized. The crucial quantity in determining how far in mass the r-process can proceed is the neutron-to-seed ratio which is directly related to the electron fraction.

Under the most neutron rich conditions the solar r-process peaks are well reproduced in size, but slightly shifted to the right, to higher mass numbers. Values for the electron fraction as low as 0.1 resemble the conditions expected in neutron star mergers [43]. The neutron-to-seed ratio in this extreme scenario reaches values of over 200, due to the large neutron densities $n_n > 10^{31}\,\mathrm{cm}^{-3}$. With so many neutrons available, the r-process reaches regions in the nuclide chart where fission becomes the dominant reaction channel. Simultaneously the iron group nuclei are almost completely consumed in this process and the supply of material from the low mass range dries up before neutrons are exhausted. This results in an abundance distribution devoid of almost any nuclei below $A \sim 110$. The fission products typically populate the A=130 region and continue capturing the still abundant neutrons until they again reach mass regions where fission occurs. Even after freeze-out ($Y_n/Y_{seed} = 1$), neutron density remains high and neutrons are continuously being captured. Thus the abundance distribution is shifted to heavier masses. This effect was also observed in nucleosynthesis studies based on neutron star mergers [43]. We will further discuss the influence of fission on the final abundance pattern in the next section.

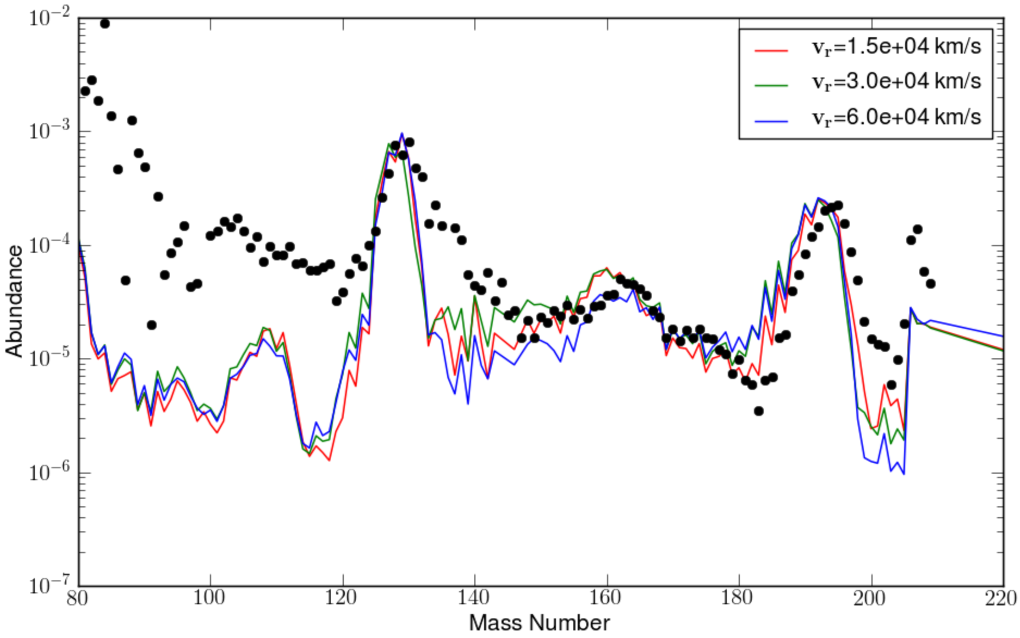

Figure 5.3: Results of standard calculation (see text) for different values of the expansion velocity. Scaled solar r-process abundances from [119] are plotted for comparison (black dots).

Only for the slightly less neutron rich conditions with $Y_e = 0.15$, the heaviest stable isotopes around Pb are produced in large amounts. At the onset of the r-process the neutron-to-seed ration adds up to ~ 110 which is enough to synthesize the heaviest elements from seed nuclei, which are typically around ^{80}Ni and heavier, but not quite enough for fission to have a strong effect.

The best overall agreement with solar abundances is achieved with an initial electron fraction of $Y_e = 0.2$. A neutron-to-seed ratio of only about 60 seems to be sufficient to reproduce both r-process peaks and also the region between the peaks. We therefore take $Y_e = 0.2$ as reference value for further parametric calculations to study the influence of density and expansion velocity.

With an initial Y_e around 0.25 there are only very little neutron captures occurring, not enough to build up material beyond A=130 in appreciable amounts. However, the second r-process peak is well populated. With even larger electron fractions and consequently only around 15 neutrons per seed nuclei the reaction flow does not proceed beyond A=130.

Comparing the results from our model calculation with the solar system r-process abundances we notice that the peaks, with the exception of the one corresponding to the calculation with the lowest Y_e value, are slightly shifted to the left, to lower mass numbers. This indicates that the r-process path lies very far from stability, maybe too far to exactly reproduce the solar abundances. The location of the path in $(n, \gamma) - (\gamma, n)$ equilibrium is determined by the relation between photodisintegrations and neutron captures and therefore between temperature and neutron density.

Fixing the electron fraction to a value of $Y_e = 0.2$, we performed further calculations to invesitgate the influence of density on the final abundance distribution. The results of these calculations are presented in Figure 5.2. An increase in the initial density results in a slightly lower entropy. Neutron capture rates depend strongly on the neutron density. At the same time photodisintegrations only depend on the temperature and therefore, capture reactions are slightly favoured at higher density. This is particularly important for the reaction flow at waiting point nuclei with closed neutron shells. Once the r-process flow reaches a nuclide with magic neutron number far from stability it can not continue via neutron captures because the isotope with N+1 neutrons has a very low neutron separation energy and is almost instantly photodisintegrated. By subsequent β-decays and neutron captures, matter accumulates in a sequence of nuclei with magic neutron number. Consequently, the r-process path moves closer to stability until eventually a nuclide is reached, where neutron capture is more efficient than photodisintegration of its neighbour. Once this bottleneck is breached, the r-process proceeds very quickly, until the next magic neutron number is reached. For which nuclide a magic neutron number barrier is surpassed depends strongly on temperature and neutron density. Already a small increase in the neutron capture rate allows the flow to continue earlier and at higher temperature and thus to reach higher mass regions. In Figure 5.2 this is expressed by a slight enhancement, with increasing density, of the mass regions following a r-process peak. In case of initial densities around $2 \times 10^8\,\mathrm{g/cm^3}$, the r-process does not operate properly. Because of the low density, the reaction flow can only proceed beyond the N=82 closed neutron shell at lower temperature and closer to stability. However, the abundance flow through closed shell waiting points quickly ceases due to the decreasing density. Thus leaving a large amount of free neutrons unprocessed. These neutrons are captured on nuclei in the mass range $140 < A < 160$, moving them to higher mass numbers. Without the fresh supply from the mass range below the magic neutron number this results in a trough in the mass range $A = 140 - 160$, while the higher mass region differs less from calculations with higher initial densities. In general the r-process abundance pattern is very similar for densities above $8 \times 10^8\,\mathrm{g/cm^3}$. We also note that the shift of peaks towards lower mass numbers is decreasing for lower initial densities, indicating that the r-process path is moving closer to stability.

The differences in the abundance distributions in Figure 5.3 can be explained in a similar manner. Shown are final abundances for standard calculations, where only the expansion velocity was varied. The higher the expansion velocity, the faster the density decreases. Therefore, there is less time for waiting point nuclei to capture a neutron or to decay into the next isotopic chain while the strong neutron flux sustains the r-process. This results in a dip in the abundances behind the peaks that grows with increasing velocity, indicating that the abundace flow through nuclei with magic neutron numbers is less effective. Again we see a relatively robust abundance pattern for expansion velocities in the investigated value range.

Variation of the initial radius has the inverse effect on the expansion as variation of the velocity. The expansion factor $R_0/R(t)$ in Eq.(5.1) can also be expressed in terms of the initial radius and the expansion velocity $1/(1 + t(v/R_0))$. Increasing the initial radius by some factor has the same effect on the expansion and therefore on the outcome of the r-process calculation as reducing the velocity by the same factor.

From these calculations we can draw the conclusion that, if the approximation of adiabatically expanding matter at constant velocity is valid, the jets from MHD core-collapse supernovae could provide the conditions for a successful r-process. Variations on either density or velocity alone only have a weak effect on the outcome of the r-process

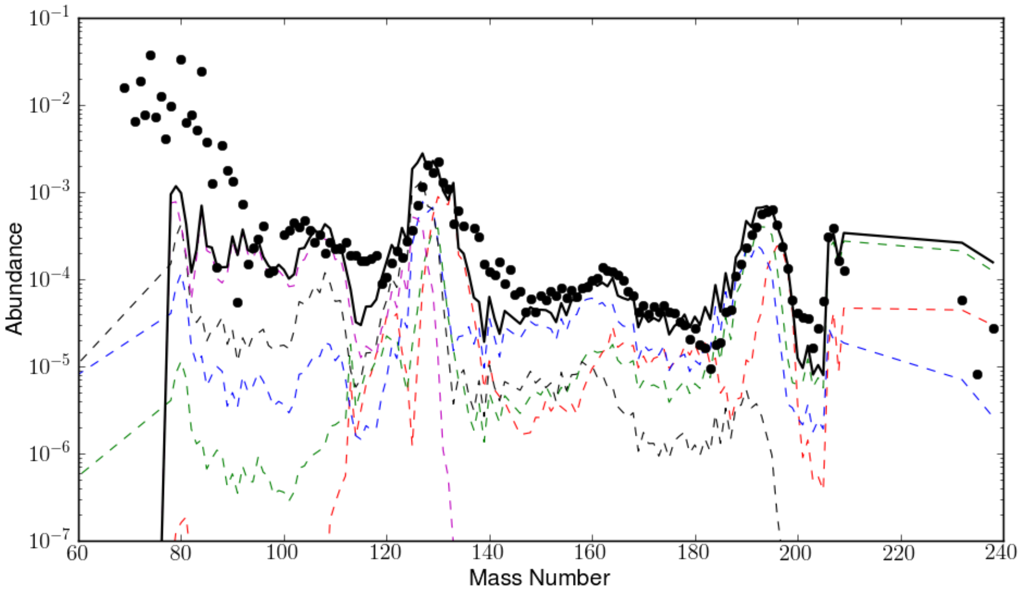

Figure 5.4: Linear superposition (solid black) of the different electron fraction components in Figure 5.1 (dashed lines with corresponding colours). Scaled solar r-process abundances from [119] are plotted for comparison (black dots).

in the given parameter range, indicating a rather robust mechanism. The dominant parameter in determining the final abundance pattern is clearly the electron fraction and with it the neutron-to-seed ratio. The solar r-process abundance distribution could then be reproduced by a superposition of different Y_e components. Already the linear superposition of the different Y_e components presented in Figure 5.1 shows an almost perfect fit to the solar r-process abundance distribution (Figure 5.4). To test this hypothesis with more sophisticated input, we will perform postprocessing calculations on data from 3D simulations of MHD core collapse supernovae [68] in section 5.3.

5.2 The Influence of Fission

We have seen in the previous section that fission plays an important role in determining the final abundance distribution under very neutron rich conditions. In this section we will give a short discussion of the influence of different fission modes and fission fragment distributions on the final abundances. A detailed quantitative analysis, however, is beyond the scope of this thesis. We performed four sets of calculations in the framework of our parametrized expansion, for two initial values of the electron fraction (0.1 and 0.15) and two models for the fission fragment mass distribution discussed in Section 2.6.4: one from Panov et al. [98](*Panov*), the other from Kodama&Takahashi [66] (*Kodama*). For each combination of Y_e and distribution model final abundances were calculated including different types of fission reactions: no fission (*nofiss*), neutron-induced fission only (*nf*), β-delayed fission only (bf) or both (*nf+bf*). Results of these calculations are presented in Figures 5.5 and 5.6 for $Y_e = 0.1$ and $Y_e = 0.15$ respectively.

In the extremely neutron rich scenario of $Y_e = 0.1$ fission reactions play an important

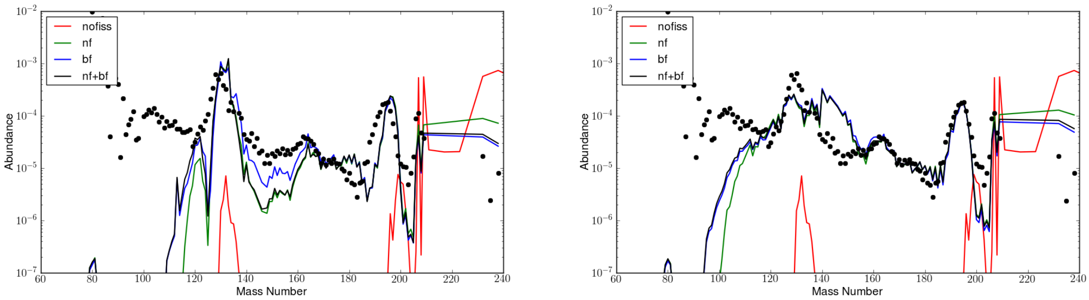

Figure 5.5: Final abundance pattern for standard calculations with $Y_e = 0.1$. Plotted are the results of 4 calculations including different fission modes, no fission (nofiss), neutron-induced fission only (nf), β-delayed fission only (bf), neutron-induced and β-delayed fission (nf+bf). Scaled solar r-process abundances from [119] are plotted for comparison (black dots). Two different fission fragment distributions were employed, Panov et al.[98] (left side) and Kodama&Takahashi [66].

role in preventing the reaction flux from converting basically all seed nuclei into heavy nuclei with mass numbers $A > 200$. What happens if this limiting factor is missing, is illustrated by the red line in Figure 5.5 representing a calculation not including any fission reactions. With the exception of two small peaks in the region of the solar r-process peaks, all material is accumulated in nuclei with mass larger than 200. Including neutron induced fission rates prevents the reaction flux from proceeding beyond nuclei in the region $Z = 93 - 95$. When neutrons are still abundant, these nuclei are reached at neutron numbers $N > 180$, populating the mass numbers $A = 132$ and $A = 140 - 150$ via asymmetric fission in the *Panov* model. During the decay to stability delayed neutrons from β-decays, as well as neutrons from previous fission reactions and some left-over neutrons, induce further fission reactions on nuclei in the mass range $A = 250 - 270$ leading to two characteristic peaks in the green line in Figure 5.5 (left). The first peak around $A = 120$ is fed by the lighter product of asymmetric fission of nuclei with $A < 255$, the second peak around $A = 130$ results from symmetric fission in the mass range $A = 255 - 265$ and from the heavy fragment of fission in the $A < 255$ region. The abundances of nuclei with $A > 210$ are enhanced in the case where only neutron induced fission is considered. Without β-delayed fission reactions present, the very heavy nuclei can decay almost unhindered towards the $N = Z$ region. From there they finaly decay back to stable nuclei via alpha-decays, thus effectively increasing the final abundance of nuclei with $A > 210$.

If only β-delayed fission is taken into account the reaction flow can initially pass almost unhindered to the heavy mass region. As soon as nuclei start to decay, β-delayed fission reactions begin to effectively populate the same mass ranges as neutron induced fission in the previous case. However, the heavier nuclei with $Z = 95 - 100$ and $A > 265$, which can not be reached in the cases where neutron induced fission is present, decay asymmetrically with the heavier fragment lying in the mass range $A = 140 - 170$. This leads to increased final abundances in this mass region compared to the other calculations in Figure 5.5 assuming *Panov* fission fragment distribution. β-delayed fission is also more prominent than neutron induced fission in the lower mass region. This leads to effectively increased abundances in the $A = 110 - 120$ region.

Combining both fission channels results in an enlarged peak around $A = 120$,

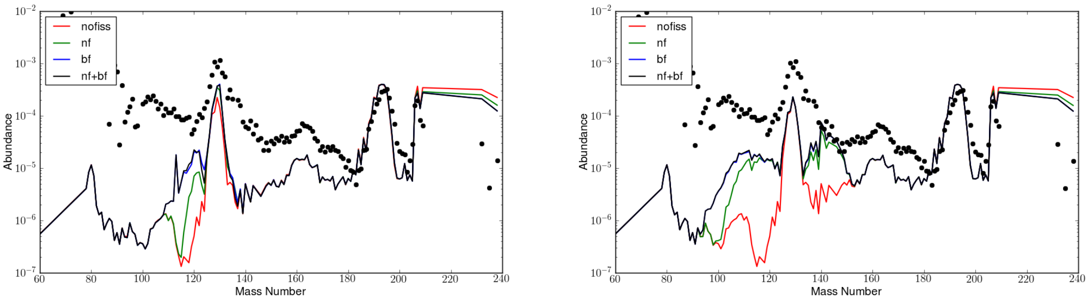

Figure 5.6: Final abundance pattern for standard calculations with $Y_e = 0.15$. Plotted are the results of 4 calculations including different fission modes, no fission (nofiss), neutron-induced fission only (nf), β-delayed fission only (bf), neutron-induced and β-delayed fission (nf+bf). Scaled solar r-process abundances from [119] are plotted for comparison (black dots). Two different fission fragment distributions were employed, Panov et al.[98] (left side) and Kodama & Takahashi [66].

which is mostly populated by β-delayed fission during decay to stability, but lacks the enrichment in nuclei with $A = 140 - 160$, because the heavy nuclei with fission fragments in this region are not reached with neutron-induced fission effectively blocking the reaction path. When employing the *Kodama* fission fragment mass distribution (Figure 5.5, right) the effects of different fission reaction channels are less pronounced, because the distribution is much more smeared out than the binary *Panov* distribution. The only visible effects are enhanced actinide abundances, and less nuclei with $A < 120$ in the case where only neutron induced fission is considered. The enhancement of abundances in the $A = 140 - 160$ region in the case where only β-delayed fission is included is less pronounced. In any case, this mass region is generally overproduced utilizing the *Kodama* fragment distribution.

For the calculations starting at $Y_e = 0.15$, fission is much less important than in the previous case. Even with no fission reactions present, the abundance distribution shows the same peak structure for all calculations. When using the *Panov* fission fragment distribution abundances in the A=120 mass region are only slightly enhanced when only neutron induced fission is considerd. In the case where only β-delayed fission is included, this effect is much stronger. The fact that the mass region beyond $A = 130$ is not affected by fission indicates that the reaction flux does not reach the region where neutron induced fission becomes a limiting factor. Again the *Kodama* fission fragment distribution shows a much broader distribution around the $A = 130$ peak.

For an initial $Y_e \gtrsim 0.17$ fission reactions do not change the final abundance distribution noticeably. We will consider the different fission fragment distributions when calculating ejecta compositions in Section 5.3.4.

5.3 3D MHD CCSN Simulations

To further investigate Jets from MHD CCSN as possible r-process site, apart from the parametric study in the previous section, we have to rely on input data from Simulations. Studies of heavy element nucleosynthesis in MHD jets have already been performed in 2D for collapsar models [45, 46] and CCSN [89]. In both scenarios the r-process was seen to operate successfully in the jets. With the recent advent of 3D

Model	Resolution [km]	3D domain(max) $(x \times y \times z)$ [km]	B_0 [G]	Ω_0 [rad/s]
1	2	$600 \times 600 \times 1000$	1×10^{13}	π
2	1	$700 \times 700 \times 1400$	5×10^{12}	π

Table 5.2: Parameters of the computational setup

MHD CCSN simulations [68] we are in the fortunate position to extend the analysis of this promising r-process candidate.

5.3.1 Simulation Setup

The data presented throughout this section originates from two different 3D simulations performed by R. Käppeli [68]. The ideal MHD equations are solved with the three-dimensional parallel magnetohydrodynamics code FISH [69]. To close the system of equations the equation of state (EoS) table of Lattimer & Swesty [72] is included. A spectral neutrino leakage scheme by A. Perego is used to approximate the effect of neutrino cooling by electron neutrinos and anti-neutrinos. Heating effects from neutrino interactions are not considered. However, in the most microphysically complete study of magneto-rotational CCSN in 2D axisymmetry to date [21] it was shown that the contribution from neutrino heating accounts only for 15-25% of the total explosion energy. All calculations are based on the presupernova model of a $15\mathrm{M}_\odot$ star from Heger et al [53]. For a detailed description of the numerical methods employed in this simulations, we refer to [68].

The 3D computational domain consists of a central cube of $600^3\,\mathrm{km}^3$, covering the innermost regions of the massive star where the explosion is supposed to set in. To follow the fast expansion of the jets for longer timescales, the 3D domain can be enlarged dynamically during the calculation. The 3D domain is embedded in a larger spherical symmetric domain, encompassing the iron core and parts of the silicon shell, treated by the time-implicit hydrodynamics code AGILE [74].

In Table 5.2 we give a summary of initial conditions and Table 5.3 lists some resulting quantities of the simulation and the postprocessing for the two models. Model 1 represents an early model with a lower resolution of 2 km but larger initial magnetic field (10^{13} G). The computation was performed until the jet reached the border of the enlarged 3D domain of $600 \times 600 \times 1000\,\mathrm{km}^3$ (in x- ,y- and z-direction respectively)

Model	$t_{f,pb}$ [ms]	tracers ejected/total	M_{ej} $M_\odot$	$M_{r,ej}$ $M_\odot$
1	12	294/9852	2.87×10^{-2}	1.59×10^{-2}
2	33	136/20005	6.72×10^{-3}	5.64×10^{-3}

Table 5.3: Combined results from the simulation and the postprocessing. $t_{f,pb}$ indicates the final time relative to core bounce at which simulation was stopped. M_{ej} is the sum of the masses of all ejected zones, $M_{r,ej}$ is the integrated mass of r-process elements ($A \geq 63$) which are ejected.

corresponding to ∼12 ms after core bounce. Model 2 is a high resolution calculation where the evolution of the explosion was followed until ∼33 ms post bounce. The 3D domain was extended to $700 \times 700 \times 1400\,\mathrm{km}^3$. The initial magnetic field was reduced by a factor of two compared to model 1. In order to reduce the computational time the initial magnetic fields are set to be about 3 orders of magnitude higher than the prediction for the presupernova model [54]. To reach the same grade of amplification with flux compression and field winding alone would require a much longer simulation time and hence dramatically increase the computational time.

5.3.2 Postprocessing of Tracer Data

To follow the time evolution of physical quantities like temperature, density and electron fraction, a Lagrangian component in the form of tracer particles was added to the models. In the following we will refer to tracer particles simply as *tracers*. These virtual, massless particles do not influence the calculations, but are advected with the fluid and thus follow the effective motion of matter during all stages of the explosion. Desired quantities are calculated at each timestep by interpolating the 3D data according to the position of the tracer. Tracers are initially distributed homogeneously within a sphere of radius 1000 km. The huge task of efficiently implementing the tracers into the parallelized 3D MHD code was accomplished by R. Käppeli as part of his PhD thesis [68].

Figures 5.7 and 5.8 show the time evolution of Y_e, density, radial velocity and temperature for selected ejected tracers of model 1 and 2 respectively. Following the solid black line in Figure 5.7 we can discuss general effects, observable in all tracers. In the initial phase ($t < 0.5\,ms$) the tracer is still infalling, indicated by the negative radial velocity. Once it reaches the shock front, the velocity turns positive but initially remains at relatively low value. At the same time, temperature and density increase quickly by about an order of magnitude and reach values over $100\,GK$ and $10^{12}\,g/cm^3$ respectively. The electron fraction drops rapidly as a result of electron captures first on Fe nuclei, and as those are dissociated even more efficiently by electron captures on free protons. During the next $\sim 4\,ms$ the particle is accelerated inside the jets, until its velocity reaches a value of $\sim 3 \times 10^4\,km/s$, corresponding to 10% the speed of light. Density and temperature decrease exponentially to more and more moderate values. Simultaneously, the electron fraction keeps decreasing as long as electron captures are permitted by the local conditions. After $\sim 5\,ms$ the radial velocity of the particle stays approximately constant, thus supporting the assumptions we made in the parametric calculations. Temperature and density keep decreasing, slowly approaching values where matter is not in NSE anymore and the composition has to be determined from nucleosynthesis calculations. Once the electron fraction has reached its minimum, around $Y_e = 0.2$, it can not change anymore in the simulation because neutrino heating is not considered at the moment, as the influence on the dynamics is negligible. Future nucleosynthesis calculations will show whether the inclusion of neutrino heating in the postprocessing has a significant influence on the composition. However, for all nucleosynthesis calculations in this thesis we did not consider neutrino capture reactions.

The evolution of tracers in model 2 is analogous to the one in model 1. We have to note however, that the density reaches maximum values about an order of magnitude higher than in model 1, and consequently, the electron fraction drops to lower values.

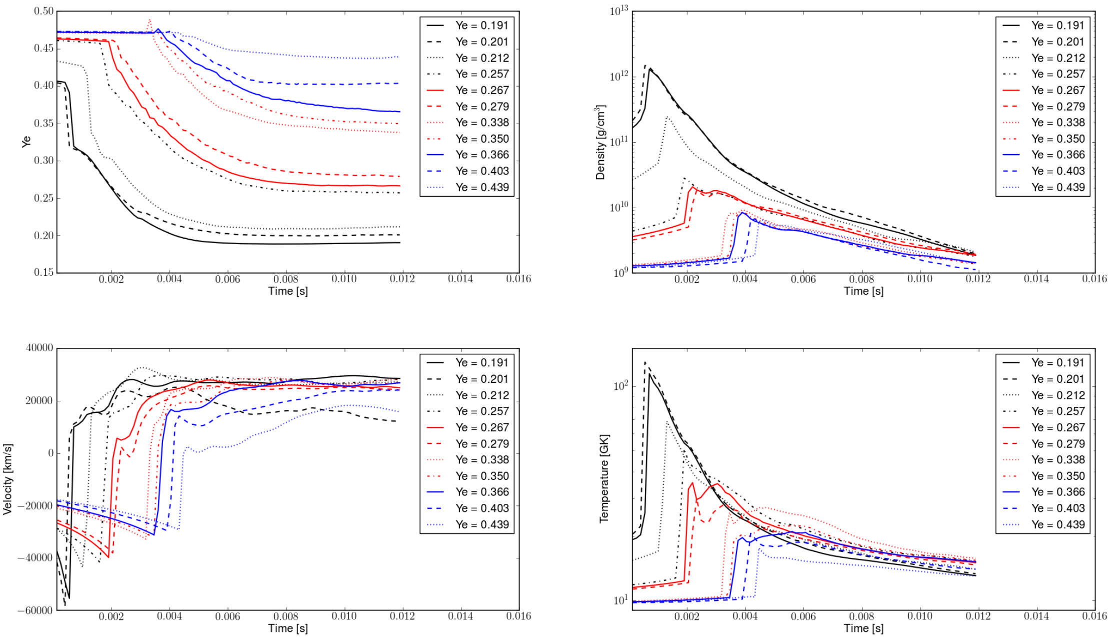

Figure 5.7: Evolution of the electron fraction (top left), density (top right), velocity (bottom left) and temperature (bottom right) for selected ejected particles of model 1.

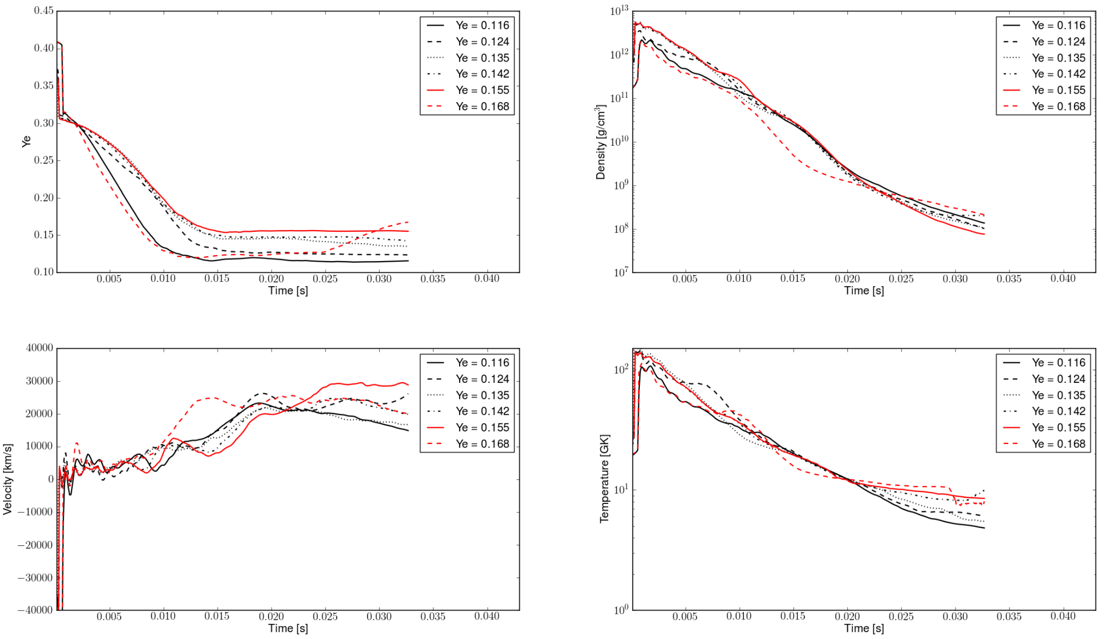

Figure 5.8: Evolution of the electron fraction (top left), density (top right), velocity (bottom left) and temperature (bottom right) for selected ejected particles of model 2.

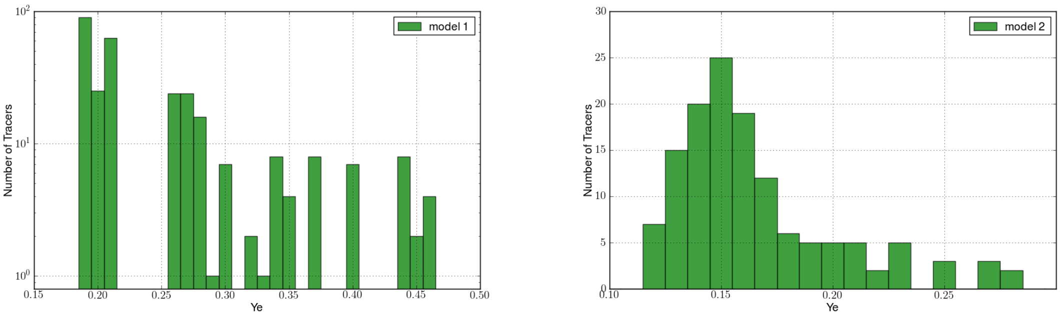

Figure 5.9: Histogram of the Y_e distribution in tracers of model 1 (left) and model 2 (right). The total number of particles in model 1 (model 2) is 294 (136).

Also, the whole process is considerably slower, due to the weaker initial magnetic field. The tracers stay longer in the dense region close to the proto-neutronstar, revolting around the polar axis where the jets are formed. This is expressed by the oscillations of the radial velocity in the initial phase. Velocities around $\sim 3 \times 10^4\, km/s$ are only reached after $\sim 25\, ms$. Owing to the longer simulation time, the temperature reaches values below 10 GK, where nuclear reactions become important for nucleosynthesis.

To determine whether a particle is ejected, we demand that its total energy, i.e. the sum of the kinetic and internal energy of the particle, the gravitational potential and magnetic pressure, at its current location is bigger than zero [90]. In addition we only consider particles that are actually moving outwards, i.e. with a radial velocity bigger than zero. Therefore, the combined ejection criterion in terms of specific energy is given by

$$\begin{aligned} \varepsilon = \frac{1}{2}v_r^2 + \varepsilon_{int} + \Phi + \frac{B^2}{8\pi\rho} &> 0 \\ v_r &> 0. \end{aligned} \tag{5.2}$$

In model 1, the above criterion is met by 294 of the 9852 tracers that were initially positioned in the simulation. In model 2 the number of ejected particles, 136, is considerably lower than in model 1, even more so bearing in mind that twice as much particles were initial put into the simulation (see Table 5.3). To perform nucleosynthesis calculations, in particular r-process calculations, the temperatures at the end of tracer evolution (at t_f) are still too high. Hence, after t_f we assume that temperature and density evolve according to the expansion we introduced for the parametric calculations (Eq.(5.1)). It was shown that the exact form of the expansion does not affect the abundance changes in the expansion phase dramatically [45, 89]. Figure 5.16 shows a comparison of expansions with different initial conditions and the influence on the final abundance distribution. It will be discussed in more detail in the next section.

Figure 5.10 shows a superposition of mass fractions for all 294 tracers ejected in model 1. The agreement with the solar r-process element distribution is very good. Both r-process peaks are well reproduced, even though they are slightly shifted to the left. In general the curve is very similar to the abundance distribution, obtained in the parametric calculations, for an initial $Y_e = 0.2$ (Figure 5.1, blue line). This can be easily explained by looking at the Y_e-histogram in the left panel of Figure 5.9. About half of the tracers are accumulated in the range $0.19 \leq Y_e \leq 0.21$, making this the

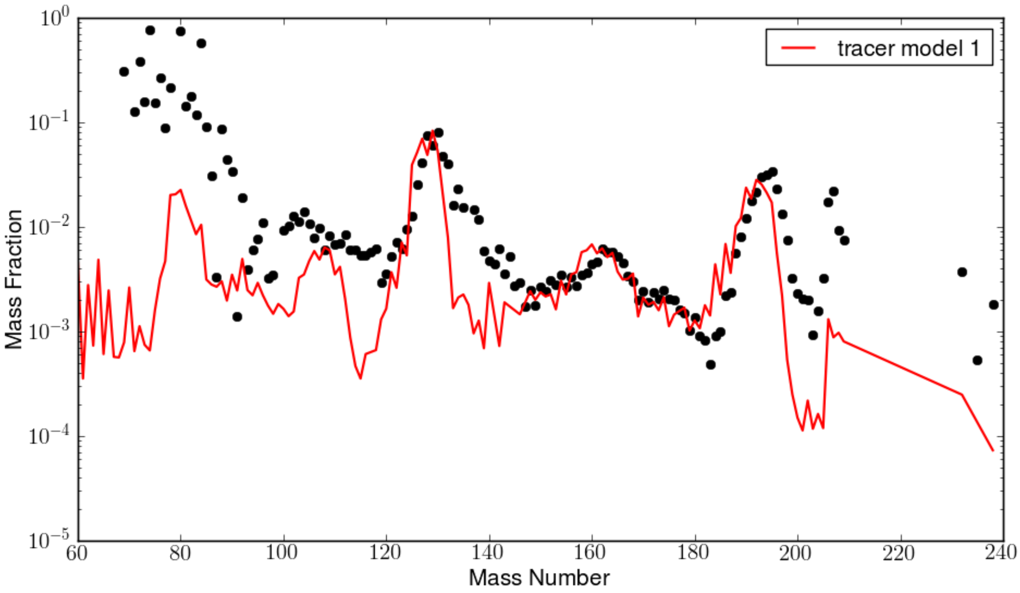

Figure 5.10: Integrated mass fractions of all 294 ejected tracer partricles of model 1. Black dots represent the solar r-process element distribution [119], scaled to fit the graph at A=162.

dominant contribution in the superposition. It was also shown in the parametric study, that calculations with $Y_e > 0.25$ do not contribute much to the abundances in the mass region $A > 130$.

The Y_e histogram of model 2 looks very different compared to the one from model 1. The distribution of the electron fraction somehow resembles a Planck distribution with a maximum at $Y_e = 0.15$ and a high-Y_e tail up to values of $Y_e = 0.27$. Compared to the results from model 1 the maximum is shifted to lower values and the region with $Y_e > 0.27$ is completely missing. Judging from this distribution we would expect a resulting abundance distribution similar to the green line in Figure 5.1, corresponding to an initial $Y_e = 0.15$. The superposition of the final mass fractions of all 136 tracers of model 2, shown in Figure 5.11, confirms our prediction. The third r-process peak and the Pb region agree very well with the solar r-process element distribution. Because of the lack of significant contributions with $Y_e = 0.2 - 0.25$, the region of mass numbers between the r-process peaks is significantly underproduced. At low mass numbers, the distribution drops to very low values because there are no contributions from initially high electron fractions which contribute almost entirely to this region.

In summary, the results obtained from postprocessing of tracers look promising and agree well with solar abundances. In order to make sure that the tracers provide a representative sample of the ejecta, we will discuss an alternative method to get input data for nucleosynthesis directly from the 3D data of the simulation in the next section.

5.3.3 Extraction of 3D Data

In addition to using tracers as input for the postprocessing calculations, we decided to extract initial conditions directly from the 3D data at the last time step of the

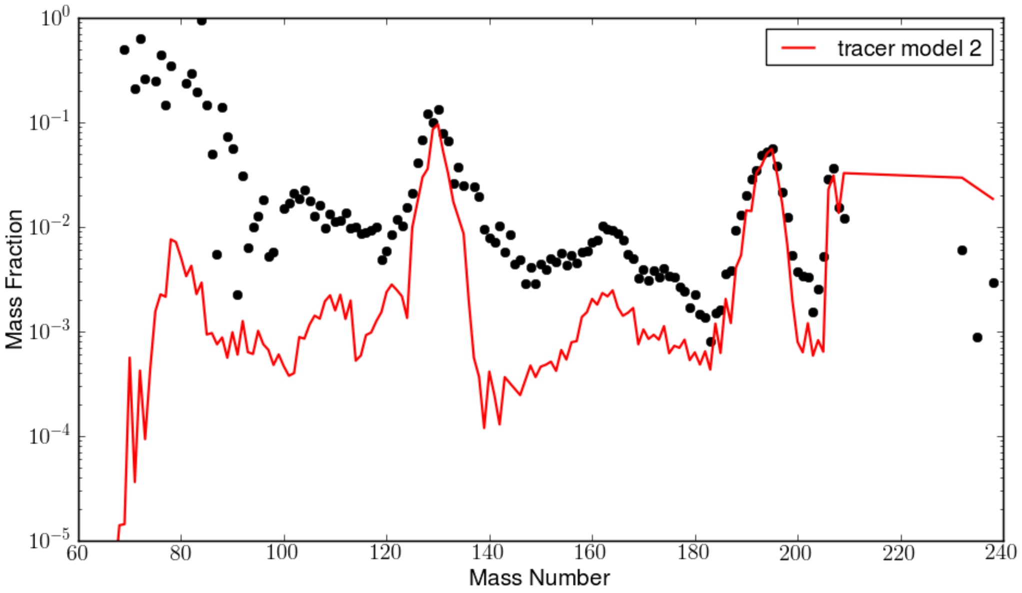

Figure 5.11: Integrated mass fractions of all 136 ejected tracer partricles of model 2. Black dots represent the solar r-process element distribution [119], scaled to fit the graph at A=195.

simulations. These initial values are then time evolved using the adiabatic expansion that was already used for the parametrized calculations and the expansion of tracer trajectories. This data should yield a complete picture of the composition of the ejecta, and any potential bias in the tracers would be detected. As an additional benefit, the mass of the ejecta appears naturally in this method.

For the MHD simulations the 3D domain is subdivided into cubes (we also refer to this cubes as zones) with side length according to the resolution (2km in model 1, 1km in model 2). To determine whether matter in such a cube is ejected or not, we use the same criterion as for the tracers (Eq.(5.2)). The number of zones fulfilling this criterion is approximately 5×10^6 for model 1 and 5×10^7 for model 2. This corresponds to roughly 10% of the computational domain in both models. Figures 5.12 and 5.13 illustrate the spatial distribution of the ejecta in the yz-plane, color coded in the electron fraction, for model 1 and 2 respectively. In Figure 5.12 the distribution of the electron fraction inside the jets is rather homogeneously at a value of 0.2-0.25 and without turbulent effects. This is mostly due to the strong magnetic pressure which is pushing the jets outwards at high velocities, thus effectively rendering convection impossible at this stage. The ejected section consists mainly of the neutron rich tip of the jet carrying with it some of the material it is ploughing through. This results in a bow shock with $Y_e \sim 0.45 - 0.5$. The bottom of the jet is located at a distance of about 200 km from the center of the core. Figure 5.13 shows large fluctuations of the electron fraction and strong turbulent effects. The electron fraction is generally lower than in model 1 and larger regions with very low Y_e are encountered. The ejected part has a droplike shape emerging from the vicinity of the proto-neutronstar. A region with high Y_e is formed at the tip of the jet, where it pushes through the outlying matter.

To extract initial conditions from the large number of ejected zones, we basically

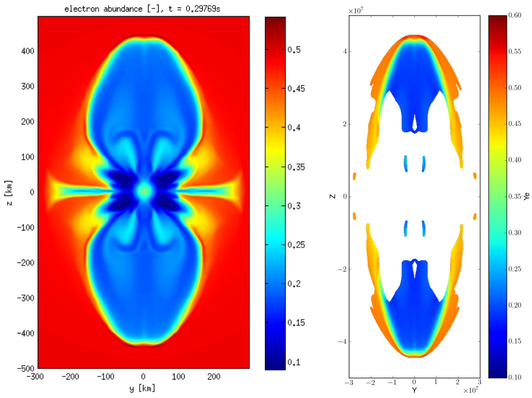

Figure 5.12: Colour map of the electron fraction for all computational zones (left) and the ejected zones(right) of model 1. Note that the time indicated is the total simulation time, not the time since core bounce.

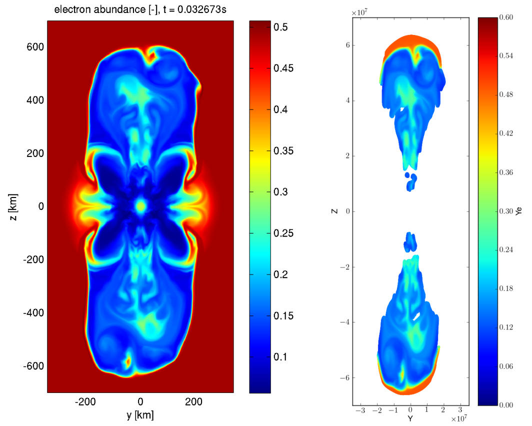

Figure 5.13: Colour map of the electron fraction for all computational zones (left) and the ejected zones(right) of model 2.

generate a two-dimensional histogram for each relevant quantity with respect to the electron fraction, weighted by the mass of the individual zones. We will discuss the exact procedure on the example of density. The range of electron fractions is divided into equidistant bins with a width of 0.01. The center of each bin is located at integer multiples of 0.01. The density range is also subdivided, but this time into 100 exponentially spaced bins. Because of the different data ranges we decided to divide temperature and radius into 100 equidistant bins, but density and velocity in 100 exponentially spaced bins. The mass of each ejected zone is then added to the bin that corresponds to the combination of Y_e and density that prevails in this zone. Once this is done for all zones, the density bin that accumulates the most mass for a given Y_e is taken as initial density for the corresponding Y_e. This results in a single combination of density, temperature, radius and expansion velocity for each Y_e bin. This combination is then taken as representative for the total mass contained in this Y_e bin.

The resulting histograms are presented in Figures 5.14 and 5.15 for model 1 and model 2 respectively. The colour map represents the mass of each bin. Black crosses denote the initial conditions that are extracted from each figure. One can clearly see that the spread in the data from model 1 is much smaller than for the corresponding data from model 2, indicating much more homogeneous ejecta. In general, density, temperature and radial velocity are at higher values in model 1. On the other hand the electron fraction does certainly reach lower values in model 2. We also have to point out that the calculated initial temperatures for the three lowest Y_e bins in model 2 are below 10 GK. Because we rely on an initial temperature above 9 GK to infer the initial composition in the postprocessing from NSE, we need to extrapolate backwards to higher temperatures and density. To check whether such an extrapolation changes the final abundance distribution, we performed calculations with different initial values for the extrapolation, based on data from a tracer (the one labelled $Y_e = 0.116$ in Figure 5.8). The results of this comparison are presented in Figure 5.16. Starting at an initial temperature of 10 GK we first followed the time evolution given in the tracer data

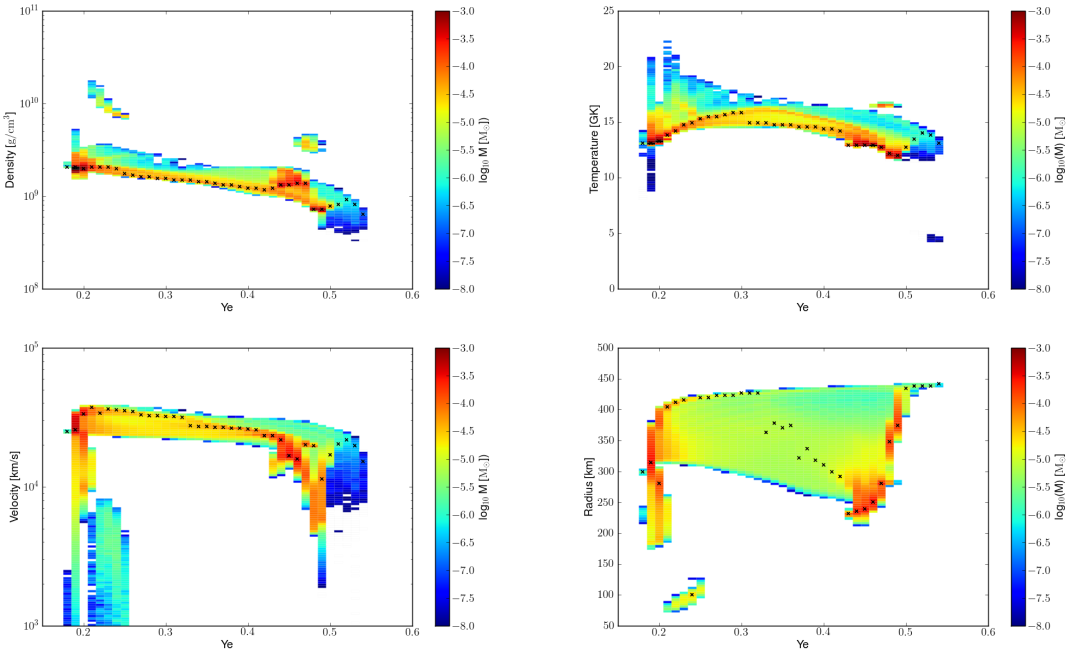

Figure 5.14: Mass weighted histogram of density (top left), temperature (top right), velocity (bottom left) and radius (bottom right) with respect to the electron fraction for the ejected zones of model 1. Black crosses denote the most massive data bin for each Y_e-bin. The corresponding value of the respective quantity is then taken as input value for the postprocessing calculation.

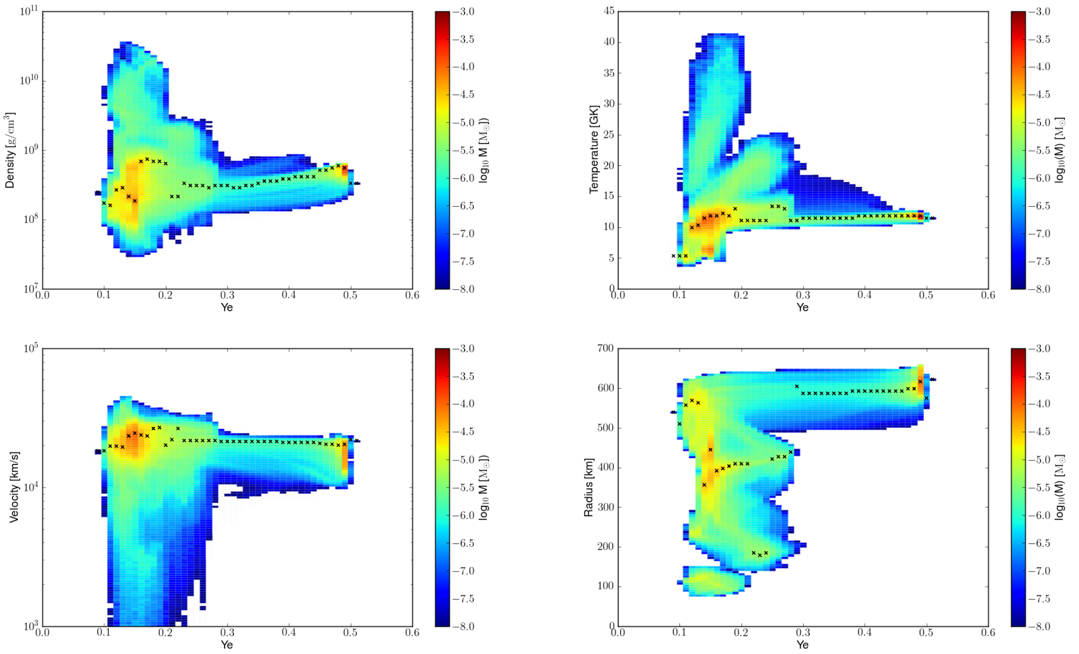

Figure 5.15: Mass weighted histogram of density (top left), temperature (top right), velocity (bottom left) and radius (bottom right) with respect to the electron fraction for the ejected zones of model 2. Black crosses denote the most massive data bin for each Y_e-bin. The corresponding value of the respective quantity is then taken as input value for the postprocessing calculation.

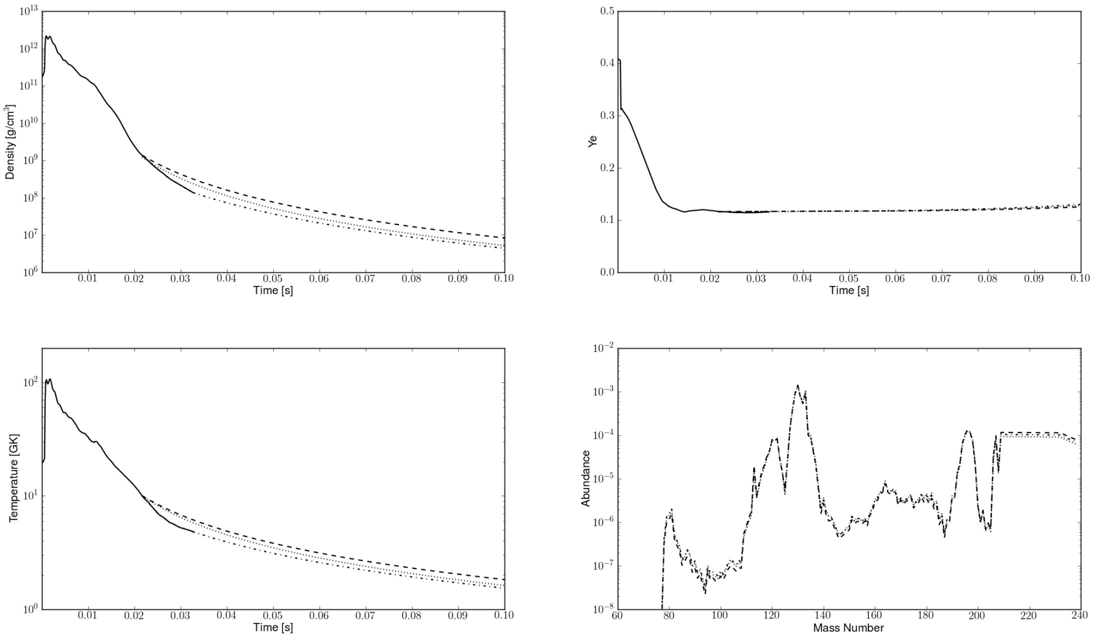

Figure 5.16: Comparison of different extrapolations of density (top left), temperature (bottom left), electron fraction (top right) and the final abundance distribution (bottom right). The tracer data (solid line) is extrapolated either from the last tracer data point (dash-dotted line) or from a time t($T_9 = 10$) with temperature, Y_e, radius and velocity corresponding to this time step (dashed line) or extrapolated back from the last tracer data point (dotted line) (see text for more details).

(solid line) until the end. From there on we performed an extrapolation based on the final values of temperature, density, radius and velocity from the tracer (dash-dotted line). A second calculation was performed, again starting at a temperature of 10 GK, but this time directly extrapolating based on the conditions given in the tracer data corresponding to this temperature (dashed line). The final calculation (dotted line), representing the method we apply in the postprocessing calculations, was again started at an initial temperature of 10 GK, however, the initial values for the expansion are extrapolated backwards starting from the tracer data at the final timestep. From Eq.(5.1) follows that initial radius and density are calculated as

$$\mathrm{R}_0 = \mathrm{R}_\mathrm{f}\frac{\mathrm{T}_\mathrm{f}}{10} \qquad \text{and} \qquad \rho_0 = \rho_\mathrm{f}\left(\frac{10}{\mathrm{T}_\mathrm{f}}\right)^3, \tag{5.3}$$

where the subscript f denotes the final values from the tracer. We assume that the electron fraction does not change during the time of this backwards extrapolation. Comparing the final abundance distribution of the different calculations, we see that the influence of the approximation is negligible.

5.3.4 Postprocessing of 3D Data

Based on the initial values, extracted from the 3D data and presented in the previous section, we performed nucleosynthesis calculations for both models. We used the same network and reaction rates as for the parametrized standard calculations and

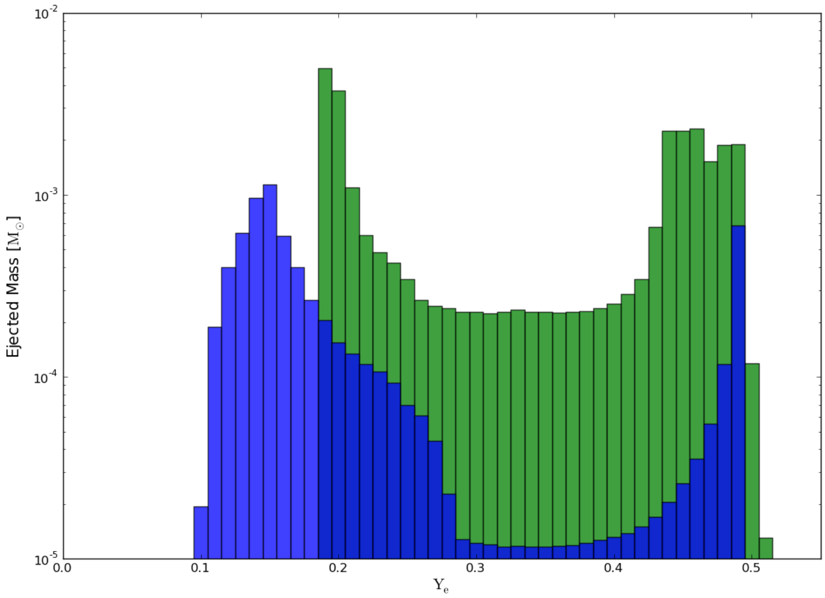

Figure 5.17: Mass distribution with respect to the initial Y_e for the nucleosynthesis calculations for model 1 (green) and model 2 (blue).

postprocessing of tracers. The final mass fractions, resulting from individual calculations for each Y_e bin within a model, are weighted with the respective mass as shown in Figure 5.17 and summed up to represent the integrated composition of the ejecta.

Figure 5.18 shows the final abundance distribution integrated over all calculated Y_e zones for model 1. The solar r-process element distribution is well reproduced, however, the peaks are slightly shifted to the left. From Figure 5.17 we can infer that the dominant mass contribution comes from regions with $Y_e = 0.2$. As it was the case for the tracer results, the peak structure of the integrated distribution shows a striking resemblance with the one presented in Figure 5.1 for an initial $Y_e = 0.2$ (blue line). In Figure 5.17 one can clearly see that bins with $0.22 \lesssim Y_e \lesssim 0.4$ are about an order of magnitude less massive compared to the outlying regions. Therefore, we do not expect large contributions from this region to the final abundances. We have also seen in the parametrized calculations, that only for $Y_e \leq 0.25$ elements with A$>$ 130 can be produced. Hence, zones with $Y_e \geq 0.25$ only contribute to the mass range below A=130. We note, that the zones with initial $Y_e \gtrsim 0.4$ accumulate quite a lot of mass. But under these conditions, mostly Fe-group nuclei are produced, which results in the staggerd line at the low-mass end of Figure 5.18. The influence of fission in these calculations is negligible, since the electron fraction does not reach low enough values for the r-process to proceed to the very heavy mass region where fission becomes relevant.

In Figure 5.17 one can see that the mass distribution for model 2 is shifted to lower values of Y_e, and that the range $0.3 < Y_e < 0.45$ is significantly suppressed. The most prominent structure is located around $Y_e = 0.15$. In Figure 5.19 the integrated abundance distribution of model 2 for two calculations with different fission fragment distribution is shown. In both cases the third r-process peak around A=195 and the Pb region provide an almost perfect fit to the scaled solar distribution. The overall peak

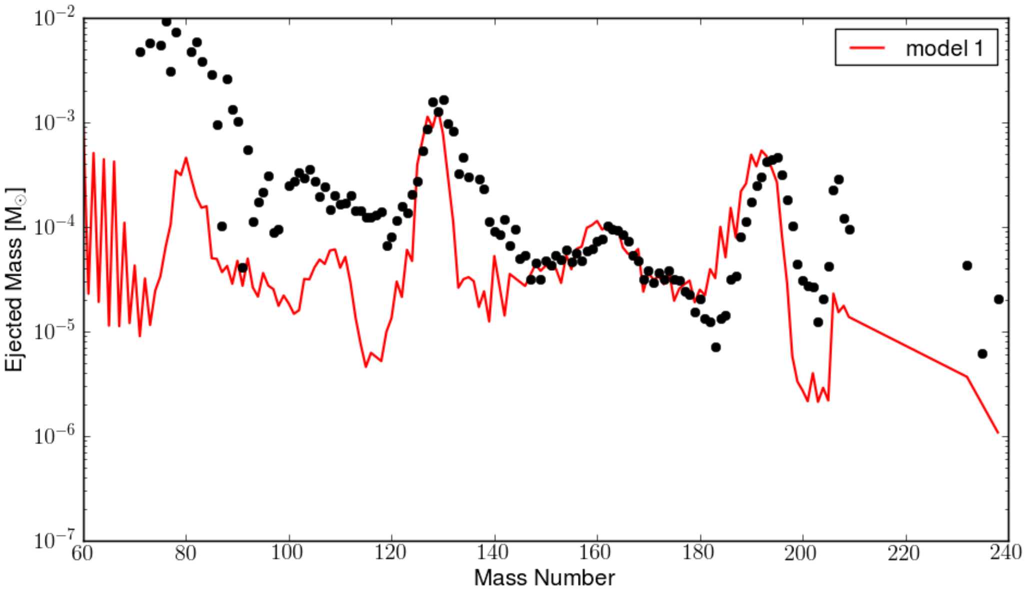

Figure 5.18: Integrated abundances of the ejecta of model 1. Black dots represent the solar r-process element distribution [119], scaled to fit the graph at A=162.

structure looks very similar to the green line in Figure 5.1 corresponding to $Y_e = 0.15$. As in model 1, this can clearly be attributed to the fact, that the dominant mass contribution is located at this value. Using the *Kodama* fission fragment distribution, the hole in the $A = 140 - 160$ region is filled up at the cost of a slightly lower $A = 130$ peak. The mass region around $A = 160 - 180$ is clearly underproduced, independent of the fragment distribution. To increase the abundances in this mass regions would require larger contributions from either very neutron rich zones with $Y_e \sim 0.1$ or slightly less neutron rich zones with $Y_e \sim 0.2$. The relatively large mass of ejecta with high values of $Y_e \sim 0.5$ results in the same oscillating line at low mass as was observed in model 1, but does not contribute to the abundances in the mass region of the r-process.

5.3.5 Discussion

In the previous sections we have presented results for two different methods to extract initial conditions for postprocessing calculations from the data obtained in 3D MHD simulations. The first is based on so called tracers, that are advected with the fluid and provide a time evolution of local quantities. The latter extracts initial conditions directly from a single snapshot in time of the full 3D computational domain. Figure 5.20 shows a comparison of these results for both models considered in the calculations. The mass fractions resulting from the tracer calculations were scaled to fit the integrated mass distribution. One can clearly see that the results agree in both models almost perfectly for the mass range relevant for the r-process. Only the mass region below $A = 80$ is underproduced in the results from calculations based on tracer data. This can be explained by a lack of tracers with $Y_e \sim 0.5$, which can be seen by comparing Figure 5.9 with Figure 5.17. The reason for this difference can be explained by looking

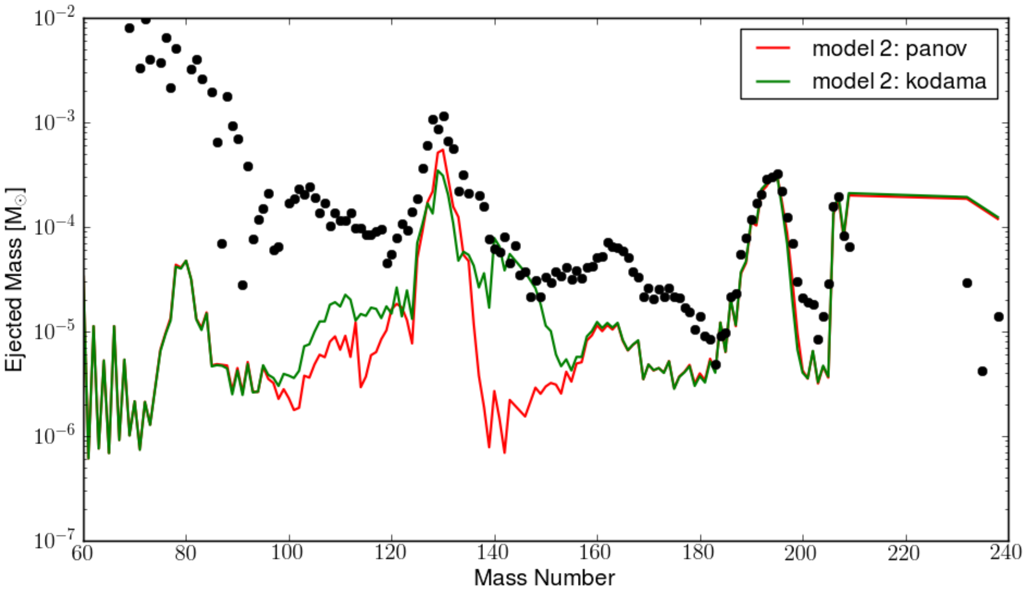

Figure 5.19: Integrated abundances of the ejecta of model 1. Plotted are the results for two fission fragment mass distributions: *Panov* (red) and *Kodama* (green) (see text for references). Black dots represent the solar r-process element distribution [119], scaled to fit the *Panov* graph at A=195.

at the Y_e distribution in the ejecta (Figures 5.12 and 5.13). The matter with high values of the electron fraction is mostly located at the tip of the jet and represents matter that was still infalling when the jet formed, and is now simply pushed by the jet. The tracers, however, were located in a sphere with radius 1000 km at the onset of core collapse. During collapse and jet formation the tracers move closer to the center and are mostly located inside the shock front. Once the jet is moving outwards there are no more tracers infalling and therefore the region in front of the jet is not sampled by the tracers. For the prediciton of r-process abundances this is negligible, since this region does not contribute to the mass range produced by the r-process.

From these results we conclude that the tracers used in the presented simulations provide a representative sample of matter inside the jets. A superposition of contributions from all tracers yields the same qualitative result as calculations of representative conditions based on the full 3D data. We will now compare our predictions with result obtained in previous calculations.

In summary we find that the abundance distribution in the ejecta from model 1 fits the solar abundances very well in the mass region $120 < A < 200$. However, heavier nuclides with $A > 200$ are underproduced. The results based on the data from model 1 also agree with results presented in [89]. Their model 4 also has a dominant contribution from tracers with $Y_e = 0.2$, resulting in an abundance distribution very similar to the one we present for model 1. The final abundance pattern for the ejecta in model 2 are characterized by a dominant contribution from $Y_e = 0.15$. Due to the strong influence of fission, the mass range $100 < A < 160$ depends heavily on the fission modes which are included and the fission fragment distribution. Independent of the treatment of fission reactions, the mass range $160 < A < 180$ is underproduced which

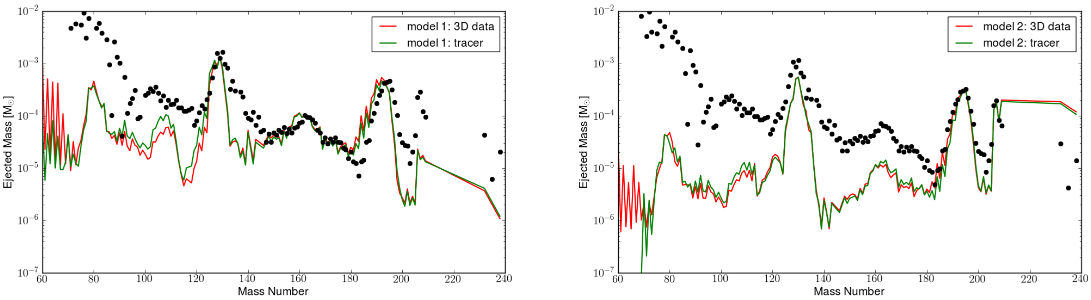

Figure 5.20: Comparison of results from tracer calculations (green) with integrated abundances obtained from 3D data extraction (red). The left frame corresponds to model 1, the right frame to model 2. Mass fractions from tracer calculations are scaled to match the 3D data results at A=162 (model 1) or A=195 (model 2). Black dots represent the solar r-process element distribution [119], scaled to fit the abundance curves at A=162 and A=195 for model 1 and model 2 respectively.

was also seen in the calculations in [45]. The third r-process peak, however, almost perfectly fits the scaled solar abundance distribution which could not be seen in the calculations in [89].

The total mass of the ejected matter is obtained by simply summing up the mass of all zones which fulfill Eq.(5.2). For model 1 (model 2) this results in $2.87 \times 10^{-2} M_\odot$ ($6.72 \times 10^{-3} M_\odot$). The stronger magnetic field in model 1 leads to an increase in the amount of ejected matter by about a factor of four compared to model 2, even though the mass of ejecta for the latter was calculated at later times. However, we have already seen before that the MHD mechanism is operating slower in model 2. Due to the expected continuous ejection of matter in the MHD jets, the total mass which is ejected is most likely to grow with time. Hence, the numbers we present should be taken with care. In any case, they provide a lower limit to what can expected from long time simulations. Comparing our results with those from [89] and [45] we first have to note that the progenitor model used in both references represents a $13 M_\odot$ which is slightly less massive than the one used in our models. Nevertheless, the amount of ejected matter, $1.65 \times 10^{-2} M_\odot$ ([89]) and $8.1 \times 10^{-2} M_\odot$ ([45]) is comparable to our model 1 or larger. Whether this is an effect of the longer simulation time (hundreds of milliseconds) or the computational setup (2D instead of 3D, different rotation rates, different initial magnetic field) is still to be investigated.

In addition to the total amount of matter which is ejected, we are also, or even more, interested in the amount of r-process elements which can be fed to the interstellar medium by a MHD CCSN. Following the notation in [89] we consider all nuclei with $A \geq 63$ as r-process elements. The amount of r-process elements ejected in model 1 (model 2) calculates to $1.59 \times 10^{-2} M_\odot$ ($5.64 \times 10^{-3} M_\odot$) accounting for 55% (83%) of the total ejecta. The relative amount of r-process material is considerably higher than in [89], where r-process elements make up only about 10% of the total mass of ejecta. This huge difference can be explained by the very different mass distribution with respect to Y_e. In our models the mass distribution shows a similar structure for both models (Figure 5.17), with pronounced peaks at very low values of $Y_e \sim 0.15 - 0.2$ as well as around $Y_e \sim 0.45 - 0.5$. In zones with initial $Y_e < 0.35$ we find the fraction of nuclei with $A \geq 63$ to be $> 90\%$. At higher Y_e the fraction quickly drops to less than

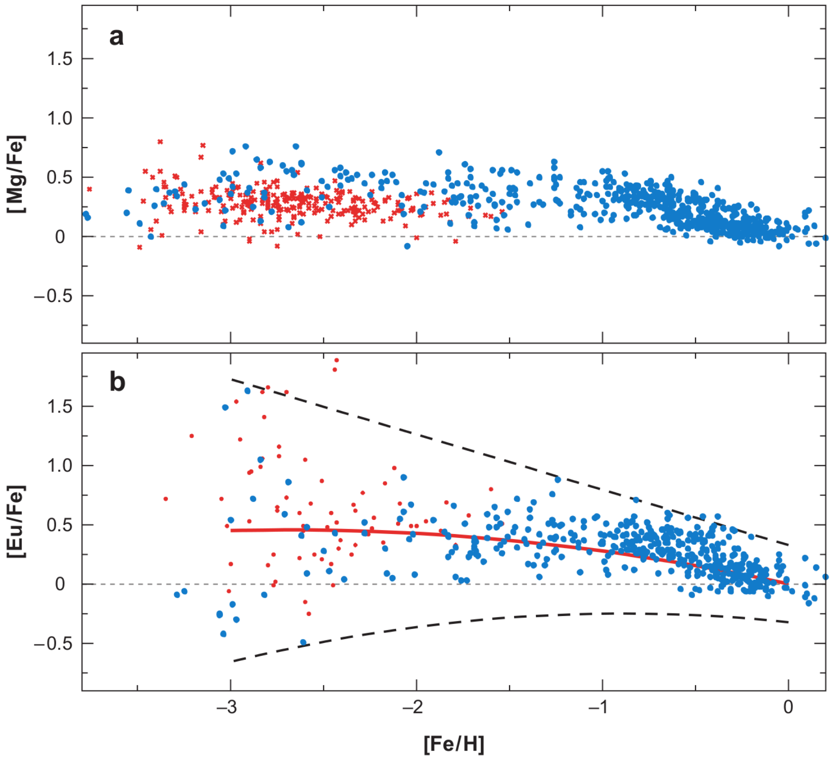

Figure 5.21: [Mg/Fe] and [Eu/Fe] abundances as function of metallicity [Fe/H] for halo and disk stars the red and blue dots are data from different large-sample surveys (see [119] for references). The thin dashed line represents the solar abundance ratios. In panel *b*, the solid red line is a least-square fit to the Eu data, and the two dashed black lines indicate the approximate extent of the Eu/Fe data (figure adopted from [119]).

1%. Therefore, we can simply estimate the ratio of ejected r-process elements to the total ejected mass by simply looking at the mass distribution with respect to Y_e and then take the ratio of the mass of zones with $Y_e < 0.35$ to zones with $Y_e \geq 0.35$. From Figure 5.17, an estimate of the r-process element fraction yields $\sim 50\%$ for model 1 and $\sim 80\%$ for model 2. In [45] the mass distribution with respect to electron fraction shows a strong peak at $Y_e = 0.45 - 0.5$ but lacks the large contribution from very low Y_e (their figs 9. and 16.), consistently resulting in a r-process element contribution of $\sim 10\%$ of the total mass. In [89] the mass distribution for the model whose results look similar to our model 1 is almost flat (their Figure 4, bottom right), and we would predict a r-process element mass $\sim 50\% - 60\%$ of the total mass. Which does not agree with the author's statement of $\sim 10\%$.

5.3.6 Implications for Galactic Chemical Evolution

In this section we will make a preliminary exploration of the influence of our results on galactic chemical evolution. If we assume, that the process by which all r-process elements in our galaxy are produced, is somehow related to CCSN, then each CCSN would need to eject $10^{-5} M_\odot$ to $10^{-4} M_\odot$ of r-material (see Section 4.2.1). If we assume, that in MHD Jets $10^{-2} M_\odot$ to $10^{-1} M_\odot$ of r-process elements are fed into the interstellar medium, then it would be sufficient if only every hundredth or thousandth CCSN actually produces a jet. This low event rate could also explain a particularity of observed r-process element abundances at low metallicity. While the abundance pattern of r-process elements in very old stars is almost identical to the one observed in the solar system, the relative abundances of typical r-process elements as Eu compared to the Fe abundance shows a huge scatter which is not observed in elements that are produced in stellar nucleosynthesis like Mg. In Figure 5.21 this effect is illustrated for both Eu and Mg relative to Fe as function of metallicity. One can clearly see that in panel *b* the data points are widely spread at low metalicites. With increasing [Fe/H] this spread is reduced (indicated by the black dashed lines). This observation is consistent with an early chemically unmixed galaxy, with individual nucleosynthetic events (e.g. CCSN) being widely spread. At later times this abundance scatter diminishes as the galaxy becomes more chemically homogeneous. It further suggests that r-process element production was rare in the early galaxy, i.e. only a few stars synthesized elements such as Eu, and that Mg and Fe production was not strongly coupled to r-process production. Therefore, Eu abundances observed in very metal-poor stars are most likely the result of only a single or very few r-process element producing events. Occurring only once in hundred or thousand supernovae, MHD Jets would naturally meet this requirement for a rare r-process event in the early galaxy.

Chapter 6

Summary and Outlook

Nuclear network evolution codes are an essential tool to explore nucleosynthesis in astrophysical processes. In course of this Ph.D. we developed a modernized version of the widespread network code of F.-K. Thielemann. The main novelties are the implementation of a powerful sparse matrix solver and a memory and computationally efficient representation of sparse matrices. The new program allows to perform nucleosynthesis calculations even for large network sizes. We also implement the treatment of β-delayed neutron emission and fission, including two different empirical fission fragment distributions. Therefore, all kinds of reactions can be included in calculations, with the exception of neutrino induced reactions (see outlook).

In the first part of this dissertation we present self-consistent standard big bang nucleosynthesis (SBBN) calculations. Using a recent reaction rate compilation [30] and a parametrized n ↔ p interconversion rate [117], our light element predictions for the latest WMAP [67] value for the baryon-to-photon ratio $\eta = 6.16 \pm 0.15 \times 10^{-10}$ yield:

$$\begin{aligned} \mathrm{D/H} &= (2.84 \pm 0.23) \times 10^{-5} \\ {}^{3}\mathrm{He/H} &= (1.07 \pm 0.09) \times 10^{-5} \\ \mathrm{Y_p} &= 0.2490 \pm 0.0005 \\ {}^{7}\mathrm{Li/H} &= (4.57 \pm 0.55) \times 10^{-10}. \end{aligned}$$

We find these values to be in good agreement with observations (except for ^{7}Li) and theoretical predictions. The SBBN predicted overabundance of primordial ^{7}Li compared to observations is a well known problem and appears consistently in all SBBN calculations. The results for ^{3}He, ^{4}He and ^{7}Li are also found to be consistent with the calculated deuterium abundance. Another shortcoming of current SBBN calculations is that the predicted isotopic ratio ${}^{6}\mathrm{Li}/{}^{7}\mathrm{Li}$ is three to four orders of magnitude lower than what is observed. We investigate the influence of recent evaluations [52, 82] of the main production reaction ${}^{2}\mathrm{H}\,(\alpha,\gamma)\,{}^{6}\mathrm{Li}$ on the predicted ^{6}Li abundance. The results show no significant increase of the ^{6}Li abundance, on the contrary, in one case (using the rate of [82]) the final abundance is actually reduced. Calculations based on an inhomogeneous big bang scenario yield a slight increase on the abundances of C, N, O and F, but no significant production of heavy elements.

In the second part of the thesis we explore magnetically driven jets from core collapse supernovae as possible site for the production of heavy elements via the r-process. We first study the influence of different initial parameters and of fission on the final abundance distribution in a parameter study, based on an adiabatic expansion. We find that the electron fraction, Y_e, is the key quantity to determine whether an r-process occurs. A superposition of five calculations for $Ye = 0.1, 0.15, 0.2, 0.25, 0.3$ yields an almost perfect reproduction of solar system abundances in the mass range $120 \leq A \leq 210$. Fission reactions are found to be important only in calculations with $Y_e \leq 0.17$. The choice of fission fragment distribution has a strong influence on abundances in the mass range $100 \leq A \leq 160$.

The main results of this thesis are the first postprocessing calculations based on data from 3D magneto-hydrodynamic simulations of core collapse supernova simulations. The calculations are based on two simulations with different resolution, initial magnetic field and simulation duration [68]. We present results for two different methods to extract data from the simulation. The first is based on built-in Lagrangian tracer particles that record the time evolution of relevant quantities. The second is based on the full 3D data at the last timestep of the simulation, from where we extract data via a 2-dimensional, mass-weighted histogram. For both methods the same extrapolation as in the parametric study has to be employed to simulate the long term evolution. Results of both methods are found to be nearly identical within each model.

The results for both models show a good qualitative agreement with the global solar system abundances pattern and results obtained from 2D simulations [89]. However, the detailed distributions obtained from the two models show some differences. Whether these are due to our method of data extraction, or different initial conditions, spatial resolution or simulation time of the simulations can not be resolved at the moment. We also calculate the ejected mass in both models, which is found to be consistent with galactic chemical evolution, assuming that only $0.1\% - 1\%$ of all core collapse supernovae form a jet. This in turn naturally meets the requirement for a rare r-process event in the early galaxy, explaining the large star-to-star scatter of r-process element abundances in very old halo stars.

Our results indicate, that MHD jets from core collapse supernovae are a promising r-process site candidate. However, it would be premature to claim that it is *the* r-process site. Nevertheless, we claim it worthwhile to further investigate this scenario.

As projects for the near future we plan to investigate the effect of neutrino heating by including neutrino capture reactions into the postprocessing calculations. Also the influence of the theoretical mass model should be studied. A quantitative analysis of the ejecta will provide further insight on the detailed composition.

The new reaction network is already being used in different projects, and the demand is steadily increasing. Still, there are a few rough edges to be removed before it can be made available for the broad scientific community.

Appendix A

Self-Consistent Big Bang Evolution

As we have seen in section 3.1 the expansion only depends on one single parameter, η. Thus, the time evolution of temperature and density has to be calculated self-consistently without introducing more free parameters. Our prescription for the self-consistent calculation closely follows the explanations in Appendix D of [65] using the same terminology. The implementation of this scheme was already done as part of a masterthesis, but we will repeat the theoretical details for completeness.
There are three interdependent quantities to be evolved in order to get the desired time evolution of the temperature and the baryon density. These quantities are the temperature T_9 (in units of 10^9K), the electron chemical potential ϕ_e, and the quantity h defined by

$$h \equiv \frac{M_u n_b}{T_9^3} = M_u \frac{n_\gamma}{T_9^3}\eta \tag{A.1}$$

where M_b is the unit of atomic mass ([135] Eq.4) and η the cosmological parameter. In addition we need the nuclide abundances Y_i along with their time derivatives $\dot{Y}_i$. The baryon density and the electron chemical potential are calculated using h and T_9

$$\rho_b \sim hT_9^3 \tag{A.2}$$

$$\phi_e \sim \frac{ChY_p}{z^3}\left[\frac{1}{\sum_n (-)^{n+1} nL(nz)}\right], \tag{A.3}$$

with $C = (\pi^2/2)N_A(\hbar c/k_B)^3$, $z = m_e c^2/k_B T_9$ and $L(z)$ is given by Eq.(A.10). Initially we will determine some other quantities and derivatives which will be needed to calculate the sought-after derivatives. The photon energy density depends only on the temperature

$$\rho_\gamma = \frac{\pi}{15}\frac{k_B^4}{(c\hbar)^3}T^4, \tag{A.4}$$

and it's derivative $d\rho_\gamma/dT_9$ can be calculated easily. The photon pressure is that of an ultrarelativistic particle, Eq.(3.5)

$$\frac{p_\gamma}{c^2} = \frac{1}{3}\rho_\gamma. \tag{A.5}$$

Furthermore, we need the sum of electron and positron densities (see [41] Eq.B44) and it's partial derivatives with respect to T_9 and ϕ_e

$$\rho_{e^-} + \rho_{e^+} = \frac{2}{\pi^2} \frac{(m_e c^2)^4}{(\hbar c)^3} \sum_{n=1}^{\infty} (-)^{n+1} \cosh(n\phi_e) M(nz) \tag{A.6}$$

$$\frac{\partial(\rho_{e^-} + \rho_{e^+})}{\partial \phi_e} = \frac{2}{\pi^2} \frac{(m_e c^2)^4}{(\hbar c)^3} \sum_{n=1}^{\infty} (-)^{n+1} n \sinh(n\phi_e) M(nz) \tag{A.7}$$

$$\frac{\partial(\rho_{e^-} + \rho_{e^+})}{\partial T_9} = \frac{2}{\pi^2} \frac{(m_e c^2)^4}{(\hbar c)^3} \sum_{n=1}^{\infty} (-)^{n+1} n \cosh(n\phi_e) N(nz), \tag{A.8}$$

as well as the sum of electron and positron pressures (see [41] Eq.B27)

$$\frac{p_{e^-} + p_{e^+}}{c^2} = \frac{2}{\pi^2} \frac{(m_e c^2)^4}{(\hbar c)^3} \sum_{n=1}^{\infty} \frac{(-)^{n+1}}{nz} \cosh(n\phi_e) L(nz). \tag{A.9}$$

The functions $L(z)$, $M(z)$ and $N(z)$ are defined as

$$L(z) = \frac{K_2(z)}{z} \tag{A.10}$$

$$M(z) = \frac{1}{z} \left[\frac{3}{4} K_3(z) + \frac{1}{4} K_1(z) \right] \tag{A.11}$$

$$N(z) = \frac{1}{z} \left[\frac{1}{2} K_4(z) + \frac{1}{2} K_2(z) \right] \tag{A.12}$$

where $K_n(z)$ are modified Bessel functions. Information about Bessel functions, their derivatives and addition theorems can be found in [6].

Finally, we also need the difference of the electron and positron number densities (see [41] Eq.B6) and again the partial derivatives $\partial/\partial T_9$ and $\partial/\partial \phi_e$

$$\frac{\pi^2}{2} \left[\frac{\hbar c}{m_e c^2} \right]^3 z^3 \left(n_{e^-} - n_{e^+} \right) = z^3 \sum_{n=1}^{\infty} (-)^{n+1} \sinh\left(n\phi_e \right) L\left(nz \right) \tag{A.13}$$

$$\frac{\partial}{\partial \phi_e} (...) = z^3 \sum_{n=1}^{\infty} (-)^{n+1} n \cosh\left(n\phi_e \right) L\left(nz \right) \tag{A.14}$$

$$\frac{\partial}{\partial T_9} (...) = -\frac{z^3}{T_9} \sum_{n=1}^{\infty} (-)^{n+1} \sinh\left(n\phi_e \right) \left[3L(nz) - nzM(nz) \right]. \tag{A.15}$$

The form of the equations may look strange at first sight but will eventually make sense in the context where they will be applied.

Ultimately, we are now able to calculate the derivatives of T_9, h, and ϕ_e from

$$\frac{dT_9}{dt} = \frac{dr}{dt} / \frac{dr}{dT_9} \tag{A.16}$$

$$\frac{dh}{dt} = -3h \left[\frac{1}{R}\frac{dR}{dt} + \frac{1}{T_9}\frac{dT_9}{dt} \right] \tag{A.17}$$

$$\frac{d\phi_e}{dt} = \frac{\partial \phi_e}{\partial T_9}\frac{dT_9}{dt} + \frac{\partial \phi_e}{\partial r}\frac{dr}{dt} + \frac{\partial \phi_e}{\partial S}\frac{dS}{dt}, \tag{A.18}$$

where R is the scale factor, $r = \ln\left(R^3\right)$, and $S = \sum_i Z_i Y_i$. We will discuss these three expressions separately in detail.

dT_9/dt :

The numerator of Eq.(A.16) can be calculated straightforward, using the second Friedman equation Eq.(3.2)

$$H^2 \equiv \left(\frac{\dot{R}}{R}\right)^2 = \frac{8\pi G\rho + \Lambda}{3c^2} - \frac{kc^2}{R^2}. \tag{A.19}$$

Assuming a flat universe ($k = 0$) and a vanishing cosmological constant $\Lambda = 0$ yields

$$\frac{dr}{dt} = \frac{d}{dt}\ln(R^3) = 3 \cdot \frac{1}{R}\frac{dR}{dt} = 3 \cdot H. \tag{A.20}$$

For the denominator of Eq.(A.16), dr/dT_9, we have to start from the conservation of Energy (Eq.10 in [135])

$$\frac{d}{dt}\left(\rho R^3\right) + \frac{p}{c^2}\frac{d}{dt}\left(R^3\right) + R^3 \left.\frac{d\rho}{dt}\right|_{T_9=const} = 0 \tag{A.21}$$

where the third term is taking into account the energy changes introduced by nucleosynthesis. Expanding the first term, substituting $R^3 = \exp(r)$ and $dR^3 = \exp(r)dr$ and regrouping yields

$$\left(\rho + \frac{p}{c^2}\right)\frac{dr}{dt} + \frac{d\rho}{dt} + \left.\frac{d\rho}{dt}\right|_{T_9=const} = 0. \tag{A.22}$$

We can now convert this into an equation for dr/dT_9

$$\frac{dr}{dT_9} = -\frac{\frac{d\rho}{dT_9}}{\rho + \frac{p}{c^2} + \left(\frac{1}{dr/dt}\right)\left.\frac{d\rho}{dt}\right|_{T_9=const}} \tag{A.23}$$

and using ρ_e to express $(\rho_{e^-} + \rho_{e^+})$, p_e for $(p_{e^-} + p_{e^+})$ and expanding $\rho = \rho_\gamma + \rho_e + \rho_b$ and $p = p_\gamma + p_e + p_b$, this can be written in more detail

$$\frac{dr}{dT_9} = -\frac{\frac{d\rho_\gamma}{dT_9} + \frac{d\rho_e}{dT_9} + \frac{d\rho_b}{dT_9}}{\rho_\gamma + \frac{p_\gamma}{c^2} + \rho_e + \frac{p_e}{c^2} + \frac{p_b}{c^2} + \frac{1}{dr/dt}\left(\left.\frac{d\rho_b}{dt}\right|_{T_9} + \left.\frac{d\rho_e}{dt}\right|_{T_9}\right)}. \tag{A.24}$$

Since the photon density depends only on the temperature, the derivative $d\rho_\gamma/dt|_{T_9}$vanishes. The remaining photon terms are straightforward and given by Eqs.(A.4) and (A.5). For the electrons and positrons, the term $d\rho_e/dT_9$ is given as

$$\frac{d\rho_e}{dT_9} = \frac{\partial\rho_e}{\partial T_9} + \frac{\partial\rho_e}{\partial\phi_e}\frac{\partial\phi_e}{\partial T_9}, \tag{A.25}$$

where the derivatives of the density are given in Eqs.(A.7) and (A.25), and the derivative $\partial\phi_e/\partial T_9$ will be calculated further down in Eq.(A.33). The terms for the electron and positron density and pressure come from Eqs.(A.6) and (A.9). The baryon density, as given by Eq.(A.2), would go strictly as $1/R^3$ and thus drop out of equation (A.24). However, if we use a more detailed equation for the baryon density ([135] Eq.2)

$$\begin{aligned}\rho_b &= n_b[M_u + \sum_i \left(\Delta M_i + \frac{3k_BT}{2c^2}\right) Y_i] \\ &= hT_9^3\left[1 + \sum_i\left(\frac{\Delta M_i}{M_u} + \zeta T_9\right)Y_i\right],\end{aligned} \tag{A.26}$$

where ζ is just a constant, there is one derivative term remaining which would not drop out

$$\frac{d\rho_b}{dT_9} = hT_9^3\zeta\sum_i Y_i. \tag{A.27}$$

The baryon pressure is given by

$$\begin{aligned}p_b &= n_bk_BT\sum_i Y_i \\ &= hT_9^3\left(\frac{2}{3}\zeta T_9\sum_i Y_i\right).\end{aligned} \tag{A.28}$$

The last remaining terms in the denominator of Eq.(A.24) are the time derivative of the baryon density, given as

$$\left.\frac{d\rho_b}{dt}\right|_{T_9=const} = hT_9^3\sum_i\left(\frac{\Delta M_i}{M_u} + \zeta T_9\right)\frac{dY_i}{dt}, \tag{A.29}$$

and the time derivative of the electron-positron density,

$$\frac{1}{(dr/dt)}\left.\frac{d\rho_e}{dt}\right|_{T_9=const} = \frac{\partial\rho_e}{\partial\phi_e}\left(\frac{\partial\phi_e}{\partial r} + \frac{\partial\phi_e}{\partial S}\frac{\partial S}{\partial t}\frac{1}{(dr/dt)}\right). \tag{A.30}$$

The derivatives of ϕ_e are calculated below in Eqs.(A.34) and (A.35), and the derivative of S follows straightforward from its definition.

dh/dt :

Equation (A.17) follows directly from Eq.(A.2): $h \sim \rho_b/T_9^3 \sim 1/R^3T_9^3$. The first term represents the Friedman equation (A.19), and the second term has been evaluated in the previous paragraph.

$d\phi_e/dt$:

In order to calculate the partial derivatives for Eq.(A.18) we will start with the equation for charge conservation

$$n_{e^-} - n_{e^+} = N_A h T_9^3 S. \tag{A.31}$$

This equation can be rewritten so that the left-hand side is identical to the left-hand side of Eq.(A.13)

$$\frac{\pi^2}{2}\left[\frac{\hbar c}{m_e c^2}\right]^3 z^3 \left(n_{e^-} - n_{e^+}\right) = \frac{\pi^2}{2}\left[N_A \left(\frac{\hbar c}{k_B}\right)^3 hS\right]. \tag{A.32}$$

We can now call the left-hand side function $N = N(T_9, \phi_e)$ and the right-hand side function $M = M(T_9, r, S)$. Taking derivatives of both sides with respect to T_9, r and S, we get the needed partial derivatives:

$$\left.\frac{\partial M}{\partial T_9}\right|_{r,S} = \frac{\partial N}{\partial T_9} + \frac{\partial N}{\partial \phi_e}\frac{\partial \phi_e}{\partial T_9} \Longrightarrow \frac{\partial \phi_e}{\partial T_9} = \left(\frac{\partial N}{\partial \phi_e}\right)^{-1}\left[\frac{\partial M}{\partial T_9} - \frac{\partial N}{\partial T_9}\right] \tag{A.33}$$

$$\left.\frac{\partial M}{\partial r}\right|_{T_9,S} = \frac{\partial N}{\partial \phi_e}\frac{\partial \phi_e}{\partial r} \Longrightarrow \frac{\partial \phi_e}{\partial r} = \left(\frac{\partial N}{\partial \phi_e}\right)^{-1}\frac{\partial M}{\partial r} \tag{A.34}$$

$$\left.\frac{\partial M}{\partial S}\right|_{T_9,r} = \frac{\partial N}{\partial \phi_e}\frac{\partial \phi_e}{\partial S} \Longrightarrow \frac{\partial \phi_e}{\partial S} = \left(\frac{\partial N}{\partial \phi_e}\right)^{-1}\frac{\partial M}{\partial S} \tag{A.35}$$

The partial derivatives for N are given in Eqs.(A.14) and (A.15) and the partial derivatives of M are straightforward.

With the time derivatives from Eqs.(A.16), (A.17) and (A.18), the corresponding quantities are evolved using a second order Runge-Kutta method. The easiest way to time-evolve a quantitiy $x(t)$ from time t_1 to a time $t_2 = t_1 + \Delta t$ would be to use Euler's method

$$x(t_2) = x(t_1) + \Delta t \frac{dx(t_1)}{dt}. \tag{A.36}$$

Unfortunately, as we have already demonstrated in Section 2.3.2, this method is neither very accurate nor stable. To achieve higher accuracy and stability, we symmetrize the method by evaluating the derivatives at both times, t_1 and t_2, and averaging to get a final solution. We begin by using Euler's method Eq.(A.36) to get an initial trial value $\tilde{x}(t_2)$. With this trial value the time derivative $d\tilde{x}(t_2)/dt$ and averaging over the two derivatives yields

$$\frac{d\tilde{x}(t_1)}{dt} = \frac{1}{2}\left(\frac{dx(t_1)}{dt} + \frac{d\tilde{x}(t_2)}{dt}\right). \tag{A.37}$$

From there the final value can be extrapolated as

$$x(t_2) = x(t_1) + \Delta t \frac{d\tilde{x}(t_1)}{dt}. \tag{A.38}$$

For a more detailed description of this and other integration methods we refer the reader to [104].

Appendix B

Reaction Rate Fit Coefficients

B.1 $n \leftrightarrow p$

$a_0 = 1$ $a_1 = 0.15735$ $a_2 = 4.6172$
$a_3 = -0.40520 \times 10^2$ $a_4 = 0.13875 \times 10^3$ $a_5 = -0.59898 \times 10^2$
$a_6 = 0.66752 \times 10^2$ $a_7 = -0.16705 \times 10^2$ $a_8 = 3.8071$
$a_9 = -0.39140$ $a_{10} = 0.023590$ $a_{11} = -0.83696 \times 10^{-4}$
$a_{12} = -0.42095 \times 10^{-4}$ $a_{13} = 0.17675 \times 10^{-5}$ $q_{np} = 0.33979$

and

$b_0 = -0.62173$ $b_1 = 0.22211 \times 10^2$ $b_2 = -0.72798 \times 10^2$
$b_3 = 0.11571 \times 10^3$ $b_4 = -0.11763 \times 10^2$ $b_5 = 0.45521 \times 10^2$
$b_6 = -3.7973$ $b_7 = 0.41266$ $b_8 = -0.026210$
$b_9 = 0.87934 \times 10^{-3}$ $b_{10} = -0.12016 \times 10^{-4}$ $q_{pn} = 2.8602.$

B.2 $^{2}\mathrm{H}\,(\alpha,\gamma)\,^{6}\mathrm{Li}$

$^{2}\mathrm{H}\,(\alpha,\gamma)\,^{6}\mathrm{Li}$	a_0	a_1	a_2	a_3
	a_4	a_5	a_6	
[52]	3.934273×10^{1}	-1.673753×10^{1}	5.196860×10^{2}	-5.682702×10^{2}
	2.485785×10^{1}	-1.137492×10^{0}	3.265960×10^{2}	
	8.306788×10^{3}	-7.541123×10^{0}	1.542034×10^{3}	-1.298640×10^{4}
	5.289529×10^{3}	-2.587906×10^{3}	2.610200×10^{3}	
	1.012455×10^{3}	-5.707879×10^{-2}	5.009761×10^{1}	-1.810205×10^{3}
	1.959306×10^{3}	-2.085059×10^{3}	1.945842×10^{2}	
[82]	-2.398840×10^{0}	2.164957×10^{-3}	-8.117467×10^{0}	8.242741×10^{0}
	-5.530047×10^{-1}	1.514094×10^{-2}	-2.003651×10^{0}	
	-2.760158×10^{2}	-1.819156×10^{2}	3.929411×10^{3}	-3.629167×10^{3}
	1.626086×10^{2}	-8.808753×10^{0}	2.196422×10^{3}	

Table B.1: Reaclib fit parameters for the $^{2}\mathrm{H}\,(\alpha,\gamma)\,^{6}\mathrm{Li}$ reaction. The tabulated data in [52] and [82] is reproduced with a relative error $< 5\%$ [44].

B.3 $^{6}\mathrm{Li}\,(\gamma,\alpha)\,^{2}\mathrm{H}$

$^{6}\mathrm{Li}\,(\gamma,\alpha)\,^{2}\mathrm{H}$	a_0	a_1	a_2	a_3
	a_4	a_5	a_6	
[52]	0.627868×10^{2}	-0.338433×10^{2}	0.519686×10^{3}	-0.568270×10^{3}
	0.248578×10^{2}	-0.113749×10^{1}	0.328096×10^{3}	
	0.833023×10^{4}	-0.246469×10^{2}	0.154203×10^{4}	-0.129864×10^{5}
	0.528953×10^{4}	-0.258791×10^{4}	0.261170×10^{4}	
	0.103590×10^{4}	-0.171628×10^{2}	0.500976×10^{2}	-0.181020×10^{4}
	0.195931×10^{4}	-0.208506×10^{4}	0.196084×10^{3}	
[82]	0.210452×10^{2}	-0.171036×10^{2}	-0.811747×10^{1}	0.824274×10^{1}
	-0.553005×10^{0}	0.151409×10^{-1}	-0.503651×10^{0}	
	-0.252572×10^{3}	-0.199021×10^{3}	0.392941×10^{4}	-0.362917×10^{4}
	0.162609×10^{3}	-0.880875×10^{1}	0.219792×10^{4}	

Table B.2: Reaclib fit parameters for the $^{6}\mathrm{Li}\,(\gamma,\alpha)\,^{2}\mathrm{H}$ reaction. The photodisintegration reaction rate is obtained via detailed balance [44].

Bibliography

[1] http://pardiso-project.org/.

[2] http://cococubed.asu.edu/code_pages/chemical_potential.shtml.

[3] http://www.nag.co.uk/.

[4] http://download.nucastro.org/astro/reaclib/.

[5] http://www.nndc.bnl.gov/nudat2/.

[6] ABRAMOWITZ, M., AND STEGUN, I. A. *Handbook of Mathematical Functions: with Formulas, Graphs, and Mathematical Tables.* Dover Publications, 1965.

[7] ALPHER, R. A., BETHE, H., AND GAMOW, G. The Origin of Chemical Elements. *PhRv 73* (1948), 803–804.

[8] ANDERS, E., AND GREVESSE, N. Abundances of the elements: Meteoritic and solar. *GeCoA 53*, 1 (1989), 197–214.

[9] ARCONES, A., JANKA, H.-T., AND SCHECK, L. Nucleosynthesis-relevant conditions in neutrino-driven supernova outflows. I. Spherically symmetric hydrodynamic simulations. *A&A 467* (2007), 1227–1248.

[10] ARCONES, A., AND MARTÍNEZ-PINEDO, G. Dynamical r-process studies within the neutrino-driven wind scenario and its sensitivity to the nuclear physics input. *PhRvC 83*, 4 (2011), 045809.

[11] ARGAST, D., SAMLAND, M., THIELEMANN, F.-K., AND QIAN, Y.-Z. Neutron star mergers versus core-collapse supernovae as dominant r-process sites in the early Galaxy. *A&A 416* (2004), 997–1011.

[12] ARNETT, W. D., AND TRURAN, J. W. Carbon-Burning Nucleosynthesis at Constant Temperature. *ApJ 157* (1969), 339–365.

[13] ASPLUND, M., GREVESSE, N., AND SAUVAL, A. J. The Solar Chemical Composition. In *Cosmic Abundances as Records of Stellar Evolution and Nucleosynthesis* (2005), T. G. B. I. . F. N. Bash, Ed., vol. 336 of *Astronomical Society of the Pacific Conference Series*, pp. 25–+.

[14] Asplund, M., Lambert, D. L., Nissen, P. E., Primas, F., and Smith, V. V. Lithium Isotopic Abundances in Metal-poor Halo Stars. *ApJ 644*, 1 (2006), 229–259.

[15] Audi, G., Bersillon, O., Blachot, J., and Wapstra, A. H. The evaluation of nuclear and decay properties. *NuPhA 729*, 1 (2003), 3–128. The 2003 NUBASE and Atomic Mass Evaluations.

[16] Aver, E., Olive, K. A., and Skillman, E. D. A new approach to systematic uncertainties and self-consistency in helium abundance determinations. *JCAP 2010*, 05 (2010), 003.

[17] Bania, T. M., Rood, R. T., and Balser, D. S. The cosmological density of baryons from observations of ^{3}He$^+$ in the Milky Way. *Nature 415* (2002), 54–57.

[18] Bethe, H. A., and Wilson, J. R. Revival of a stalled supernova shock by neutrino heating. *ApJ 295* (1985), 14–23.

[19] Blatt, J. M., and Weisskopf, V. F. *Theoretical Nuclear Physics.* John Wiley & Sons Inc, 1952.

[20] Burbidge, E. M., Burbidge, G. R., Fowler, W. A., and Hoyle, F. Synthesis of the Elements in Stars. *Rev. Mod. Phys. 29*, 4 (1957), 547–650.

[21] Burrows, A., Dessart, L., Livne, E., Ott, C. D., and Murphy, J. Simulations of Magnetically Driven Supernova and Hypernova Explosions in the Context of Rapid Rotation. *ApJ 664* (2007), 416–434.

[22] Cameron, A. G. W. Nuclear Reactions in Stars and Nucleogenesis. *PASP 69* (1957), 201–222.

[23] Clayton, D. D. *Principles of stellar evolution and nucleosynthesis.*, 2nd ed. University Of Chicago Press, 1984.

[24] Coc, A., Goriely, S., Xu, Y., Saimpert, M., and Vangioni, E. Standard Big-Bang Nucleosynthesis up to CNO with an improved extended nuclear network. *arXiv:1107.1117v1* (2011).

[25] Coc, A., Olive, K. A., Uzan, J.-P., and Vangioni, E. Nonuniversal scalar-tensor theories and big bang nucleosynthesis. *PhRvD 79* (2009), 103512.

[26] Coc, A., and Vangioni, E. Big-Bang nucleosynthesis with updated nuclear data. *JPCS 202*, 1 (2010), 012001.

[27] Committee on the Physics of the Universe, and National Research Council. *Connecting Quarks with the Cosmos: Eleven Science Questions for the New Century.* National Academies Press, 2003.

[28] Cowan, J. J., and Sneden, C. Heavy element synthesis in the oldest stars and the early Universe. *Nature 440*, 7088 (2006), 1151–1156.

[29] Cowan, J. J., Thielemann, F.-K., and Truran, J. W. Nuclear Evolution of the Universe. in preparation.

[30] Cyburt, R. H., Amthor, A. M., Ferguson, R., Meisel, Z., Smith, K., Warren, S., Heger, A., Hoffman, R. D., Rauscher, T., Sakharuk, A., Schatz, H., Thielemann, F. K., and Wiescher, M. The JINA REACLIB Database: Its Recent Updates and Impact on Type-I X-ray Bursts. *ApJS 189*, 1 (2010), 240–252.

[31] Cyburt, R. H., Ellis, J., Fields, B. D., Luo, F., Olive, K. A., and Spanos, V. C. Nuclear reaction uncertainties, massive gravitino decays and the cosmological lithium problem. *JCAP 2010*, 10 (2010), 032.

[32] Cyburt, R. H., Fields, B. D., and Olive, K. A. An update on the big bang nucleosynthesis prediction for ^{7}Li: the problem worsens. *JCAP 2008*, 11 (2008), 012.

[33] Duncan, R. C., Shapiro, S. L., and Wasserman, I. Neutrino-driven winds from young, hot neutron stars. *ApJ 309* (1986), 141–160.

[34] Ellis, J., Olive, K. A., and Vangioni, E. The effects of unstable particles on light-element abundances: Lithium versus deuterium and ^{3}He. *PhLB 619*, 1-2 (2005), 30–42.

[35] Epstein, R. I., Lattimer, J. M., and Schramm, D. N. The origin of deuterium. *Nature 263* (1976), 198–202.

[36] Farouqi, K., Kratz, K.-L., Pfeiffer, B., Rauscher, T., Thielemann, F.-K., and Truran, J. W. Charged-particle and Neutron-capture Processes in the High-entropy Wind of Core-collapse Supernovae. *ApJ 712* (2010), 1359–1377.

[37] Fields, B. Big bang nucleosynthesis in the new cosmology. *EPJA 27* (2006), 3–14.

[38] Fields, B. D., and Olive, K. A. The Revival of Galactic Cosmic-Ray Nucleosynthesis? *ApJ 516*, 2 (1999), 797–810.

[39] Fischer, T., Sagert, I., Pagliara, G., Hempel, M., Schaffner-Bielich, J., Rauscher, T., Thielemann, F.-K., Käppeli, R., Martínez-Pinedo, G., and Liebendörfer, M. Core-collapse Supernova Explosions Triggered by a Quark-Hadron Phase Transition During the Early Post-bounce Phase. *ApJS 194*, 2 (2011), 39.

[40] Fowler, W. A., Caughlan, G. R., and Zimmerman, B. A. Thermonuclear Reaction Rates. *ARA&A 5* (1967), 525–570.

[41] Fowler, W. A., and Hoyle, F. Neutrino Processes and Pair Formation in Massive Stars and Supernovae. *ApJS 9* (1964), 201–319.

[42] Freiburghaus, C., Rembges, J.-F., Rauscher, T., Kolbe, E., Thielemann, F.-K., Kratz, K.-L., Pfeiffer, B., and Cowan, J. J. The Astrophysical r-Process: A Comparison of Calculations following Adiabatic Expansion with Classical Calculations Based on Neutron Densities and Temperatures. *ApJ 516*, 1 (1999), 381–398.

[43] Freiburghaus, C., Rosswog, S., and Thielemann, F.-K. r-Process in Neutron Star Mergers. *ApJL 525*, 2 (1999), L121–L124.

[44] Frischknecht, U. private communication.

[45] Fujimoto, S.-i., Hashimoto, M.-a., Kotake, K., and Yamada, S. Heavy-Element Nucleosynthesis in a Collapsar. *ApJ 656*, 1 (2007), 382–392.

[46] Fujimoto, S.-i., Nishimura, N., and Hashimoto, M.-a. Nucleosynthesis in Magnetically Driven Jets from Collapsars. *ApJ 680*, 2 (2008), 1350–1358.

[47] Fuller, G. M., Fowler, W. A., and Newman, M. J. Stellar weak-interaction rates for sd-shell nuclei. I - Nuclear matrix element systematics with application to Al-26 and selected nuclei of importance to the supernova problem. *ApJS 42* (1980), 447–473.

[48] Fuller, G. M., Fowler, W. A., and Newman, M. J. Stellar weak interaction rates for intermediate mass nuclei. III - Rate tables for the free nucleons and nuclei with A = 21 to A = 60. *ApJS 48* (1982), 279–319.

[49] Fuller, G. M., Fowler, W. A., and Newman, M. J. Stellar weak interaction rates for intermediate-mass nuclei. IV - Interpolation procedures for rapidly varying lepton capture rates using effective log (ft)-values. *ApJ 293* (1985), 1–16.

[50] Fuller, G. M., Mathews, G. J., and Alcock, C. R. Quark-hadron phase transition in the early Universe: Isothermal baryon-number fluctuations and primordial nucleosynthesis. *PhRvD 37* (1988), 1380–1400.

[51] Gadioli, E., and Hodgson, P. E. *Pre-Equilibrium Nuclear Reactions (Oxford Studies in Nuclear Physics).* Oxford University Press, USA, 1992.

[52] Hammache, F., Heil, M., Typel, S., Galaviz, D., Sümmerer, K., Coc, A., Uhlig, F., Attallah, F., Caamano, M., Cortina, D., Geissel, H., Hellström, M., Iwasa, N., Kiener, J., Koczon, P., Kohlmeyer, B., Mohr, P., Schwab, E., Schwarz, K., Schümann, F., Senger, P., Sorlin, O., Tatischeff, V., Thibaud, J. P., Vangioni, E., Wagner, A., and Walus, W. High-energy breakup of ^6Li as a tool to study the Big Bang nucleosynthesis reaction $^2H(\alpha,\gamma)^6Li$. *PhRvC 82*, 6 (2010), 065803.

[53] Heger, A., Langer, N., and Woosley, S. E. Presupernova Evolution of Rotating Massive Stars. I. Numerical Method and Evolution of the Internal Stellar Structure. *ApJ 528*, 1 (2000), 368–396.

[54] Heger, A., Woosley, S. E., and Spruit, H. C. Presupernova Evolution of Differentially Rotating Massive Stars Including Magnetic Fields. *ApJ 626*, 1 (2005), 350–363.

[55] Hix, W. R., and Meyer, B. S. Thermonuclear kinetics in astrophysics. *NuPhA 777* (2006), 188–207. Special Issue on Nuclear Astrophysics.

[56] Hix, W. R., and Thielemann, F.-K. Computational methods for nucleosynthesis and nuclear energy generation. *JCoAM 109*, 1-2 (1999), 321–351.

[57] Itkis, M. G., Kondratiev, N. A., Kozulin, E. M., Oganessian, Y. T., Pokrovsky, I. V., Prokhorova, E. V., and Rusanov, A. Y. Bimodal fission of ^{270}Sg ($Z = 106$) in the sub-barrier fusion of ^{22}Ne and ^{248}Cm. *PhRvC 59*, 6 (1999), 3172–3176.

[58] Itkis, M. G., Okolovich, V. N., and Smirenkin, G. N. Symmetric and asymmetric fission of nuclei lighter than radium. *NuPhA 502* (1989), 243–260.

[59] Izotov, Y. I., and Thuan, T. X. The Primordial Abundance of ^{4}He Revisited. *ApJ 500*, 1 (1998), 188–216.

[60] Izotov, Y. I., Thuan, T. X., and Lipovetsky, V. A. The Primordial Helium Abundance: Systematic Effects and a New Determination. *ApJS 108*, 1 (1997), 1–39.

[61] Izotov, Y. I., Thuan, T. X., and Stasińska, G. The Primordial Abundance of ^{4}He: A Self-consistent Empirical Analysis of Systematic Effects in a Large Sample of Low-Metallicity H_{II} Regions. *ApJ 662*, 1 (2007), 15–38.

[62] Jedamzik, K. Neutralinos, big bang nucleosynthesis, and ^{6}Liin low-metallicity stars. *PhRvD 70* (2004), 083510.

[63] Jedamzik, K., Fuller, G. M., Mathews, G. J., and Kajino, T. Enhanced heavy-element formation in baryon-inhomogeneous big bang models. *ApJ 422* (1994), 423–429.

[64] Jedamzik, K., and Pospelov, M. Big Bang nucleosynthesis and particle dark matter. *NJPh 11*, 10 (2009), 105028.

[65] Kawano, L. Let's go: Early universe 2. Primordial nucleosynthesis the computer way. *FERMILAB-PUB-92-004-A* (1992), 1–58.

[66] Kodama, T., and Takahashi, K. R-process nucleosynthesis and nuclei far from the region of β-stability. *NuPhA 239*, 3 (1975), 489–510.

[67] Komatsu, E., Smith, K. M., Dunkley, J., Bennett, C. L., Gold, B., Hinshaw, G., Jarosik, N., Larson, D., Nolta, M. R., Page, L., Spergel, D. N., Halpern, M., Hill, R. S., Kogut, A., Limon, M., Meyer, S. S., Odegard, N., Tucker, G. S., Weiland, J. L., Wollack, E., and Wright, E. L. Seven-year Wilkinson Microwave Anisotropy Probe (WMAP) Observations: Cosmological Interpretation. *ApJS 192*, 2 (2011), 18.

[68] Käppeli, R. *Numerical Methods for 3D Magneto-Rotational Core-Collapse Supernova Simulation with Jet Formation.* PhD thesis, University of Basel, 2011.

[69] Käppeli, R., Whitehouse, S. C., Scheidegger, S., Pen, U.-L., and Liebendörfer, M. FISH: A Three-dimensional Parallel Magnetohydrodynamics Code for Astrophysical Applications. *ApJS 195*, 2 (2011), 20.

[70] Langanke, K., and Martínez-Pinedo, G. Rate tables for the weak processes of pf-shell nuclei in stellar environments. *ADNDT 79*, 1 (2001), 1–46.

[71] Lattimer, J. M., and Schramm, D. N. Black-hole-neutron-star collisions. *ApJL 192* (1974), L145–L147.

[72] Lattimer, J. M., and Swesty, F. D. A generalized equation of state for hot, dense matter. *NuPhA 535*, 2 (1991), 331–376.

[73] LeBlanc, J. M., and Wilson, J. R. A Numerical Example of the Collapse of a Rotating Magnetized Star. *ApJ 161* (1970), 541–551.

[74] Liebendörfer, M., Rosswog, S., and Thielemann, F.-K. An Adaptive Grid, Implicit Code for Spherically Symmetric, General Relativistic Hydrodynamics in Comoving Coordinates. *ApJS 141*, 1 (2002), 229–246.

[75] Matsuura, S., Fujimoto, S.-i., Hashimoto, M.-a., and Sato, K. Reply to "Comment on 'Heavy element production in inhomogeneous big bang nucleosynthesis"'. *PhRvD 75* (2007), 068302.

[76] Matsuura, S., Fujimoto, S.-i., Nishimura, S., Hashimoto, M.-a., and Sato, K. Heavy element production in inhomogeneous big bang nucleosynthesis. *PhRvD 72* (2005), 123505.

[77] Merrill, S. P. W. Spectroscopic Observations of Stars of Class. *ApJ 116* (1952), 21–26.

[78] Meyer, B. S. The r-, s-, and p-Processes in Nucleosynthesis. *ARA&A 32* (1994), 153–190.

[79] Meyer, B. S., Krishnan, T. D., and Clayton, D. D. Theory of Quasi-Equilibrium Nucleosynthesis and Applications to Matter Expanding from High Temperature and Density. *ApJ 498*, 2 (1998), 808–830.

[80] Mocelj, D. *Neutron- and neutrino induced reactions: their physical description and influence on r-process calculations.* PhD thesis, University of Basel, 2006.

[81] Montes, F., Beers, T. C., Cowan, J., Elliot, T., Farouqi, K., Gallino, R., Heil, M., Kratz, K.-L., Pfeiffer, B., Pignatari, M., and Schatz, H. Nucleosynthesis in the Early Galaxy. *ApJ 671*, 2 (2007), 1685–1695.

[82] Mukhamedzhanov, A. M., Blokhintsev, L. D., and Irgaziev, B. F. Reexamination of the astrophysical S factor for the α+d $\rightarrow$ 6Li+γ reaction. *PhRvC 83*, 5 (2011), 055805.

[83] Myers, W. D., and Swiatecki, W. J. Thomas-Fermi fission barriers. *PhRvC 60* (1999), 014606.

[84] Möller, P., Nix, J. R., and Kratz, K.-L. Nuclear Properties for Astrophysical and Radioactive-Ion-Beam-Applications. *ADNDT 66*, 2 (1997), 131–343.

[85] Möller, P., Nix, J. R., Myers, W. D., and Swiatecki, W. J. Nuclear Ground-State Masses and Deformations. *ADNDT 59*, 2 (1995), 185–381.

[86] Möller, P., Pfeiffer, B., and Kratz, K.-L. New calculations of gross β-decay properties for astrophysical applications: Speeding-up the classical r process. *PhRvC 67*, 5 (2003), 055802.

[87] Nakamura, K., and Particle Data Group. Review of Particle Physics. *J. Phys. G: Nucl. Part. Phys. 37*, 7A (2010), 075021.

[88] Nakamura, R., Hashimoto, M.-a., Fujimoto, S.-i., Nishimura, N., and Sato, K. Observational Constraint on Heavy Element Production in Inhomogeneous Big Bang Nucleosynthesis. *arXiv:1007.0466v1* (2010).

[89] Nishimura, S., Kotake, K., aki Hashimoto, M., Yamada, S., Nishimura, N., Fujimoto, S., and Sato, K. r-Process Nucleosynthesis in Magnetohydrodynamic Jet Explosions of Core-Collapse Supernovae. *ApJ 642*, 1 (2006), 410–419.

[90] Obergaulinger, M., Aloy, M. A., and Müller, E. Axisymmetric simulations of magneto-rotational core collapse: dynamics and gravitational wave signal. *A&A 450* (2006), 1107–1134.

[91] Oechslin, R., Janka, H.-T., and Marek, A. Relativistic neutron star merger simulations with non-zero temperature equations of state. I. Variation of binary parameters and equation of state. *A&A 467* (2007), 395–409.

[92] Oechslin, R., Rosswog, S., and Thielemann, F.-K. Conformally flat smoothed particle hydrodynamics application to neutron star mergers. *PhRvD 65* (2002), 103005.

[93] Olive, K. A., and Steigman, G. On the abundance of primordial helium. *ApJS 97* (1995), 49–58.

[94] Olive, K. A., Steigman, G., and Skillman, E. D. The Primordial Abundance of ^{4}He: An Update. *ApJ 483*, 2 (1997), 788–797.

[95] O'Meara, J. M., Burles, S., Prochaska, J. X., Prochter, G. E., Bernstein, R. A., and Burgess, K. M. The Deuterium-to-Hydrogen Abundance Ratio toward the QSO SDSS J155810.16-003120.0. *ApJL 649*, 2 (2006), L61–L65.

[96] Ott, C. D., Burrows, A., Thompson, T. A., Livne, E., and Walder, R. The Spin Periods and Rotational Profiles of Neutron Stars at Birth. *ApJS 164*, 1 (2006), 130–155.

[97] Panov, I., Kolbe, E., Pfeiffer, B., Rauscher, T., Kratz, K.-L., and Thielemann, F.-K. Calculations of fission rates for r-process nucleosynthesis. *NuPhA 747*, 2-4 (2005), 633–654.

[98] Panov, I. V., Freiburghaus, C., and Thielemann, F. K. Could fission provide the formation of chemical elements with A $\leq$ 120 in metal-poor stars? *NuPhA 688*, 1-2 (2001), 587–589.

[99] Panov, I. V., Korneev, I. Y., Rauscher, T., Martínez-Pinedo, G., Kelić-Heil, A., Zinner, N. T., and Thielemann, F.-K. Neutron-induced astrophysical reaction rates for translead nuclei. *A&A 513* (2010), A61.

[100] Peimbert, M., Luridiana, V., and Peimbert, A. Revised Primordial Helium Abundance Based on New Atomic Data. *ApJ 666*, 2 (2007), 636–646.

[101] Peimbert, M., Peimbert, A., Carigi, L., and Luridiana, V. Measurements of ^{4}He in metal-poor extragalactic H_{II} regions: the primordial Helium abundance and the $\Delta Y/\Delta O$ ratio. *Proceedings of the International Astronomical Union 5*, Symposium S268 (2009), 91–100.

[102] Pettini, M., Zych, B. J., Murphy, M. T., Lewis, A., and Steidel, C. C. Deuterium abundance in the most metal-poor damped Lyman alpha system: converging on $\Omega_{b,0}h^2$. *MNRAS 391* (2008), 1499–1510.

[103] Pinsonneault, M. H., Steigman, G., Walker, T. P., and Narayanan, V. K. Stellar Mixing and the Primordial Lithium Abundance. *ApJ 574*, 1 (2002), 398–411.

[104] Press, W. H., Teukolsky, S. A., Vetterling, W. T., and Flannery, B. P. *Numerical recipes in FORTRAN. The art of scientific computing*, 2nd ed. Cambridge: University Press, 1992.

[105] Prieto, C. A., Lambert, D. L., and Asplund, M. The Forbidden Abundance of Oxygen in the Sun. *ApJL 556*, 1 (2001), L63–L66.

[106] Rauscher, T. Nuclear Partition Functions at Temperatures Exceeding 10^{10} K. *ApJS 147*, 2 (2003), 403–408.

[107] Rauscher, T. Comment on "Heavy element production in inhomogeneous big bang nucleosynthesis". *PhRvD 75* (2007), 068301.

[108] Rauscher, T. The Path to Improved Reaction Rates for Astrophysics. *IJMPE 20* (2011), 1071–1169.

[109] Rauscher, T., Applegate, J. H., Cowan, J. J., Thielemann, F.-K., and Wiescher, M. Production of heavy elements in inhomogeneous cosmologies. *ApJ 429* (1994), 499–530.

[110] Rauscher, T., and Thielemann, F.-K. Astrophysical Reaction Rates From Statistical Model Calculations. *ADNDT 75*, 1-2 (2000), 1–351.

[111] Ryan, S., and Elliott, L. The Halo Lithium Plateau: Outstanding Issues. In *Chemical Abundances and Mixing in Stars in the Milky Way and its Satellites*, S. Randich and L. Pasquini, Eds., vol. 36 of *ESO Astrophysics Symposia*. Springer Berlin / Heidelberg, 2006, pp. 185–190.

[112] Ryan, S. G., Beers, T. C., Olive, K. A., Fields, B. D., and Norris, J. E. Primordial Lithium and Big Bang Nucleosynthesis. *ApJL 530*, 2 (2000), L57–L60.

[113] Saad, Y. *Iterative methods for sparse linear systems*, 2nd ed. SIAM, Philadelphia, 2003.

[114] Sbordone, L., Bonifacio, P., Caffau, E., Ludwig, H.-G., Behara, N. T., González Hernández, J. I., Steffen, M., Cayrel, R., Freytag, B., Van´t Veer, C., Molaro, P., Plez, B., Sivarani, T., Spite, M., Spite, F., Beers, T. C., Christlieb, N., François, P., and Hill, V. The metal-poor end of the spite plateau. *A&A 522* (2010), A26.

[115] Schenk, O., and Gärtner, K. Solving unsymmetric sparse systems of linear equations with PARDISO. *FGCS 20*, 3 (2004), 475–487. Selected numerical algorithms.

[116] Schenk, O., and Gärtner, K. On fast factorization pivoting methods for symmetric indefinite systems. *ETNA 23* (2006), 158–179.

[117] Serpico, P. D., Esposito, S., Iocco, F., Mangano, G., Miele, G., and Pisanti, O. Nuclear reaction network for primordial nucleosynthesis: a detailed analysis of rates, uncertainties and light nuclei yields. *JCAP 12* (2004), 010.

[118] Simmerer, J., Sneden, C., Cowan, J. J., Collier, J., Woolf, V. M., and Lawler, J. E. The Rise of the s-Process in the Galaxy. *ApJ 617*, 2 (2004), 1091–1114.

[119] Sneden, C., Cowan, J. J., and Gallino, R. Neutron-capture elements in the early Galaxy. *ARA&A 46* (2008), 241–288.

[120] Sneden, C., Cowan, J. J., Lawler, J. E., Ivans, I. I., Burles, S., Beers, T. C., Primas, F., Hill, V., Truran, J. W., Fuller, G. M., Pfeiffer, B., and Kratz, K.-L. The Extremely Metal-poor, Neutron Capture-rich Star CS 22892-052: A Comprehensive Abundance Analysis. *ApJ 591*, 2 (2003), 936–953.

[121] Sneden, C., McWilliam, A., Preston, G. W., Cowan, J. J., Burris, D. L., and Armosky, B. J. The Ultra–Metal-poor, Neutron-Capture–rich Giant Star CS 22892-052. *ApJ 467* (1996), 819–840.

[122] Spite, F., and Spite, M. Abundance of lithium in unevolved halo stars and old disk stars - Interpretation and consequences. *A&A 115* (1982), 357–366.

[123] Spite, M., and Spite, F. Li isotopes in metal-poor halo dwarfs: a more and more complicated story. In *IAU Symposium* (2010), C. Charbonnel, M. Tosi, F. Primas, & C. Chiappini, Ed., vol. 268 of *IAU Symposium*, pp. 201–210.

[124] Steigman, G. Primordial Alchemy: From The Big Bang To The Present Universe. *arXiv:astro-ph/0208186v1* (2002).

[125] Steigman, G. BBN and the Primordial Abundances. In *Chemical Abundances and Mixing in Stars in the Milky Way and its Satellites*, S. Randich and L. Pasquini, Eds., vol. 36 of *ESO Astrophysics Symposia*. Springer Berlin / Heidelberg, 2006, pp. 331–342.

[126] Steigman, G. The cosmological evolution of the average mass per baryon. *JCAP 2006*, 10 (2006), 016.

[127] Tammann, G. A. Supernova statistics and related problems. In *Supernovae: A Survey of Current Research* (1982), M. J. Rees & R. J. Stoneham, Ed., pp. 371–403.

[128] Thielemann, F.-K., Arcones, A., Käppeli, R., Liebendörfer, M., Rauscher, T., Winteler, C., Fröhlich, C., Dillmann, I., Fischer, T., Martinez-Pinedo, G., Langanke, K., Farouqi, K., Kratz, K.-L., Panov, I., and Korneev, I. What are the astrophysical sites for the r-process and the production of heavy elements? *PrPNP 66*, 2 (2011), 346–353. Particle and Nuclear Astrophysics, International Workshop on Nuclear Physics, 32nd Course.

[129] Thielemann, F.-K., Truran, J. W., and Arnould, M. Thermonuclear reaction rates from statistical model calculations. In *Advances in Nuclear Astrophysics* (1986), E. Vangioni-Flam, J. Audouze, M. Casse, J.-P. Chieze, & J. Tran Thanh Van , Ed., pp. 525–540.

[130] Timmes, F. X. Integration of Nuclear Reaction Networks for Stellar Hydrodynamics. *ApJS 124*, 1 (1999), 241–263.

[131] Timmes, F. X., and Swesty, F. D. The Accuracy, Consistency, and Speed of an Electron-Positron Equation of State Based on Table Interpolation of the Helmholtz Free Energy. *ApJS 126*, 2 (2000), 501–516.

[132] Travaglio, C., Gallino, R., Arnone, E., Cowan, J., Jordan, F., and Sneden, C. Galactic Evolution of Sr, Y, and Zr: A Multiplicity of Nucleosynthetic Processes. *ApJ 601*, 2 (2004), 864–884.

[133] van den Bergh, S., and Tammann, G. A. Galactic and extragalactic supernova rates. *ARA&A 29* (1991), 363–407.

[134] Vonlanthen, P., Rauscher, T., Winteler, C., Puy, D., Signore, M., and Dubrovich, V. Chemistry of heavy elements in the Dark Ages. *A&A 503* (2009), 47–59.

[135] Wagoner, R. V. Synthesis of the Elements Within Objects Exploding from Very High Temperatures. *ApJS 18* (1969), 247–295.

[136] Woosley, S. E., Wilson, J. R., Mathews, G. J., Hoffman, R. D., and Meyer, B. S. The r-process and neutrino-heated supernova ejecta. *ApJ 433* (1994), 229–246.

Curriculum Vitae

Personal Details

Name	Christian Winteler
Date of birth	16.02.1981
Citizenship	Swiss
Place of origin	Glarus Nord/GL (CH)

Education

2007 - 2011	**PhD in Theoretical Physics** University of Basel, Switzerland Thesis: *Light Element Production in the Big Bang and the Synthesis of Heavy Elements in 3D MHD Jets from Core-Collapse Supernovae*
2001 - 2007	**Master of Science in Physics** University of Basel, Switzerland Thesis: *Primordial Abundances in Light of a Self-Consistent Calculation and Updated Reaction Rates*
1997 - 2000	**Matura** (Swiss Highschool Diploma) Gymnasium Muttenz, Switzerland

During my studies I heard lectures by the following people:

C. Bandle, B. Binggeli, C. Bruder, H. Burkhart, R. Buser, S. Goedecker, M. Grote, A. Hujeirat, H.-C. Im Hof, E. Kolbe, H. Kraft, B. Krusche, D. Loss, C. Luchsinger, H. Mühry, T. Rauscher, C. Rehmann-Sutter, C. Schönenberger, I. Sick, L. Tauscher, F.-K. Thielemann, D. Trautmann, M. Wänke

Acknowledgements

I would like to thank everybody who contributed to this thesis.

- First of all I would like to thank my advisors, Prof. Dr. F.-K. Thielemann and PD Dr. T. Rauscher, for giving me the opportunity to carry out an interesting research project.
- I would also like to thank Prof. Dr. K.-L. Kratz, who agreed to be on my dissertation committee.
- Further thank goes to Roger Käppeli. His data is the rock on which the last part of this thesis is built upon.
- I am grateful to Tommy Rauscher and Urs Frischknecht for providing me with reaction rate fits whenever I needed them.
- I am indebted to Almudena Arcones. Her interest in my work and her profound knowledge were a constant motivation in the last half-year.
- I would like to thank Marc Sommer for correcting my English, and for the countless Mensa lunches we had together.
- It was a pleasure to work with all the nice people in the whole astrophysics group.
- Special thank goes to the people I shared the office with: Albino Perego, Roger ”Dr. Fortran” Käppeli and Urs ”Dr. Python” Frischknecht for the productive yet funny atmosphere.
- I acknowledge the financial support of the Swiss National Science Foundation (SNF), and the efforts of Friedel Thielemann to extend my contract as long as possible.
- I would also like to thank my family for supporting me during my studies, and for being there whenever I needed them.
- Last, but not least I wish to thank my girlfriend for her continuous love and support, and especially for raising my spirits more than once during the final (hectic) phase of writing this thesis.